NASA Contract NAS1-00122
Final Report

Integrated Orbit, Attitude, and Structural Control Systems Design for Space Solar Power Satellites

Bong Wie[1]
Dept. of Mechanical & Aerospace Engineering
Arizona State University
Tempe, Arizona 85287-6106

Carlos Roithmayr[2]
NASA Langley Research Center
Hampton, Virginia 23681-2199

Prepared for
Jessica Woods-Vedeler and Chris Moore
NASA Langley Research Center
Hampton, Virginia 23681-2199

January 2, 2001

[1]Principal Investigator, (480) 965-8674, bong.wie@asu.edu
[2]Co-Investigator, (757) 864-6778, c.m.roithmayr@larc.nasa.gov

Acknowledgment

The authors would like to thank the SSP Exploratory Research and Technology (SERT) program of NASA for supporting this project. In particular, the authors are indebted to Connie Carrington, Harvey Feingold, Chris Moore, and John Mankins without whose previous SSP systems engineering work this dynamics & control research would not have been possible. Special thanks also go to Jessica Woods-Vedeler and Tim Collins for their technical support and guidance throughout the course of this study.

Abstract

The major objective of this study is to develop preliminary concepts for controlling orbit, attitude, and structural motions of very large Space Solar Power Satellites (SSPS) in geosynchronous orbit. This study focuses on the 1.2-GW "Abacus" SSPS configuration characterized by a square (3.2 × 3.2 km) solar array platform, a 500-m diameter microwave beam transmitting antenna, and an earth-tracking reflector (500 × 700 m). For this baseline Abacus SSPS configuration, we derive and analyze a complete set of mathematical models, including external disturbances such as solar radiation pressure, microwave radiation, gravity-gradient torque, and other orbit perturbation effects. An integrated orbit, attitude, and structural control systems architecture, employing electric thrusters, is developed.

A key parameter that characterizes the sensitivity of a satellite to solar radiation pressure is the area-to-mass ratio, A/m; the value of A/m for the Abacus satellite is 0.4 m^2/kg, which is relatively large when compared to 0.02 m^2/kg for typical geosynchronous communications satellites. Solar radiation pressure causes a cyclic drift in the longitude of the Abacus satellite of 2 deg, east and west. Consequently, in addition to standard north-south and east-west stationkeeping maneuvers for ±0.1 deg orbit position control, active control of the orbit eccentricity using ion thrusters becomes nearly mandatory. Furthermore, continuous sun tracking of the Abacus platform requires large control torques to counter various disturbance torques.

The proposed control systems architecture utilizes properly distributed ion thrusters to counter, simultaneously, the cyclic pitch gravity-gradient torque, the secular roll torque caused by an offset of the center-of-mass and center-of-pressure, the cyclic roll/yaw microwave radiation torque, and the solar pressure force whose average value is about 60 N. A minimum of 500 ion engines of 1-N thrust level are required for simultaneous attitude and stationkeeping control. When reliability, lifetime, duty cycle, lower thrust level, and redundancy of ion engines are considered, this number will increase significantly. A significant control-structure interaction problem, possible for such very large Abacus platform with the lowest structural mode frequency of 0.002 Hz, is avoided simply by designing an attitude control system with very low bandwidth (< orbit frequency). However, the proposed low-bandwidth attitude control system utilizes a concept of cyclic-disturbance accommodating control to provide ±5 arcmin pointing of the Abacus platform in the presence of large external disturbances and dynamic modeling uncertainties. Approximately 85,000 kg of propellant per year is required for simultaneous orbit, attitude, and structural control using 500 1-N electric propulsion thrusters with a specific impulse of 5,000 sec. Only 21,000 kg of propellant per year is required if electric propulsion thrusters with a specific impulse of 20,000 sec can be developed. As I_{sp} is increased, the propellant mass decreases but the electric power requirement increases; consequently, the mass of solar arrays and power processing units increases.

Contents

1 Introduction and Summary **1**
- 1.1 Report Outline . . . 1
- 1.2 Evolution of Space Solar Power Satellites . . . 2
- 1.3 Research Objectives and Tasks . . . 7
- 1.4 Abacus SSPS Configuration . . . 8
  - 1.4.1 Geometric Properties . . . 8
  - 1.4.2 External Disturbances . . . 8
  - 1.4.3 Orbit Parameters and Control Requirements . . . 11
- 1.5 Major Findings and Results . . . 13
  - 1.5.1 Technical Issues . . . 13
  - 1.5.2 Control Systems Architecture . . . 19
  - 1.5.3 Attitude and Orbit Control Simulation Results . . . 21
- 1.6 Summary and Recommendations for Future Research . . . 29
  - 1.6.1 Summary of Study Results . . . 29
  - 1.6.2 Recommendations for Future Research . . . 29

2 Mathematical Models of Large Sun-Pointing Spacecraft **32**
- 2.1 Introduction to Orbit Dynamics . . . 32
  - 2.1.1 Two-Body System . . . 32
  - 2.1.2 Orbital Elements . . . 38
  - 2.1.3 Orbital Position and Velocity . . . 40
  - 2.1.4 Geosynchronous Orbits . . . 42
- 2.2 Orbital Perturbations . . . 42
  - 2.2.1 Non-Keplerian Orbit Dynamics . . . 43
  - 2.2.2 Asphericity . . . 48
  - 2.2.3 Earth's Anisotropic Gravitational Potential . . . 49
  - 2.2.4 Earth's Oblateness . . . 51
  - 2.2.5 Earth's Triaxiality . . . 53
  - 2.2.6 Luni-Solar Gravitational Perturbations . . . 56
  - 2.2.7 Solar Radiation Pressure . . . 58
  - 2.2.8 Orbit Simulation Results . . . 60
- 2.3 Rigid-Body Attitude Equations of Motion . . . 66

2.4 Abacus Satellite Structural Models 71

3 Development of Abacus Control Systems Architecture 77
3.1 Introduction to Control Systems Design 77
3.1.1 Feedback Control Systems 77
3.1.2 Classical Frequency-Domain Methods 80
3.1.3 Classical PID Control Design 82
3.1.4 Digital PID Controller 86
3.1.5 Classical Gain-Phase Stabilization 88
3.1.6 Persistent Disturbance Rejection 90
3.1.7 Classical versus Modern Control Issues 95
3.2 Control Systems Architecture 97
3.3 Control System Simulation Results 99

4 Conclusions and Recommendations 113
4.1 Summary of Study Results 113
4.2 Recommendations for Future Research 114

A Simulation of Orbital Motion 119
A.1 Introduction 119
A.2 Two-Body Motion 119
A.3 Encke's Method 120
A.4 Contributions to the Perturbing Force 121
A.4.1 Solar and Lunar Gravitational Attraction 121
A.4.2 Tesseral Harmonics 122
A.4.3 Solar Radiation Pressure 123

List of Figures

1.1 Morphology of various SSPS concepts (Moore [4], [5]). 3
1.2 A cylindrical SSPS concept with zero pitch gravity-gradient torque (Carrington and Feingold [6]). 4
1.3 Integrated Symmetrical Concentrator concept (Carrington and Feingold [6]). 5
1.4 1.2-GW Abacus/Reflector concept (Carrington and Feingold [6]). 6
1.5 Baseline 1.2-GW Abacus satellite. 9
1.6 Mass breakdown of Abacus components (Carrington and Feingold [6]). . 10
1.7 Orbit orientation with respect to the geocentric-equatorial reference frame, also called the Earth-Centered Inertial (ECI) reference system. A near circular orbit is shown in this figure. 12
1.8 Orbit simulation results with the effects of the earth's oblateness and triaxiality, luni-solar perturbations, and 60-N solar radiation pressure force. 17
1.9 Orbit simulation results with the effects of the earth's oblateness and triaxiality, luni-solar perturbations, and 60-N solar radiation pressure force (continued). 18
1.10 A schematic illustration of the NSTAR 2.3-kW, 30-cm diameter ion thruster on Deep Space 1 Spacecraft (92-mN maximum thrust, specific impulse ranging from 1,900 to 3,200 sec, 25 kW/N, overall efficiency of 45–65%). 20
1.11 An integrated orbit, attitude, and structural control system architecture employing electric propulsion thrusters. 22
1.12 Placement of a minimum of 500 1-N electric propulsion thrusters at 12 different locations, with 100 thrusters each at locations #2 and #4. (Note: In contrast to a typical placement of thrusters at the four corners, e.g., employed for the 1979 SSPS reference system, the proposed placement of roll/pitch thrusters at locations #1 through #4 minimizes roll/pitch thruster couplings as well as the excitation of platform out-of-plane bending modes.) 23
1.13 Control simulation results with cyclic-disturbance rejection control in the presence of various dynamic modeling uncertainties. 24
1.14 Roll/pitch thruster firings for simultaneous eccentricity and roll/pitch control. 25
1.15 Yaw thruster firings for simultaneous inclination and yaw attitude control. 26

1.16 Orbit control simulation results with simultaneous orbit and attitude control. . . . 27
1.17 Orbit control simulation results with simultaneous orbit and attitude control (continued). . . . 28

2.1 Two-body problem. . . . 32
2.2 The eccentric anomaly E of an elliptic orbit. . . . 36
2.3 Orbit orientation with respect to the geocentric-equatorial reference frame, also called the Earth-Centered Inertial (ECI) reference system. A near circular orbit is shown in this figure. . . . 38
2.4 Perifocal reference frame. . . . 40
2.5 A two-dimensional view of the oblate earth. . . . 51
2.6 Solar radiation pressure force acting on an ideal flat surface (a case with 45-deg pitch angle ϕ is shown here). . . . 59
2.7 Orbit simulation results with the effects of the earth's oblateness and triaxiality, luni-solar perturbations, and 60-N solar pressure force. . . . 62
2.8 Orbit simulation results with the effects of the earth's oblateness and triaxiality, luni-solar perturbations, and 60-N solar pressure force (continued). 63
2.9 Orbit control simulation results with continuous (non-impulsive) eccentricity and inclination control. . . . 64
2.10 Orbit control simulation results with continuous (non-impulsive) eccentricity and inclination control (continued). . . . 65
2.11 A large space solar power satellite in geosynchronous orbit. . . . 66
2.12 Abacus structural platform concepts (Courtesy of Tim Collins at NASA LaRC). . . . 72
2.13 Baseline Abacus finite element model (Courtesy of Tim Collins at NASA LaRC). . . . 73
2.14 Baseline Abacus vibration modes (Courtesy of Tim Collins at NASA LaRC). 74
2.15 Selected FEM node locations for control analysis and design (Courtesy of Tim Collins at NASA LaRC). . . . 75
2.16 Bode magnitude plots of reduced-order transfer functions from an input force at node #1 to various output locations. . . . 76

3.1 Block diagram representations of a feedback control system. . . . 78
3.2 Control of a double integrator plant by direct velocity and position feedback. 83
3.3 Control of a double integrator plant using a phase-lead compensator. . . . 85
3.4 Simplified block diagram of the pitch-axis pointing control system of the Hubble Space Telescope [17], [28]. . . . 87
3.5 Persistent disturbance rejection control system (transfer function description). . . . 91
3.6 Persistent disturbance rejection control system (state-space description). 93
3.7 Persistent-disturbance rejection control system for the ISS. . . . 96

3.8 A schematic illustration of the NSTAR 2.3-kW, 30-cm diameter ion thruster on Deep Space 1 Spacecraft (92-mN maximum thrust, specific impulse ranging from 1,900 to 3,200 sec, 25 kW/N, overall efficiency of 45–65%). 98
3.9 An integrated orbit, attitude, and structural control system architecture employing electric propulsion thrusters. 101
3.10 Placement of a minimum of 500 1-N electric propulsion thrusters at 12 different locations, with 100 thrusters each at locations #2 and #4. (Note: In contrast to a typical placement of thrusters at the four corners, e.g., employed for the 1979 SSPS reference system, the proposed placement of roll/pitch thrusters at locations #1 through #4 minimizes roll/pitch thruster couplings as well as the excitation of platform out-of-plane bending modes.) 102
3.11 Simulation results without cyclic-disturbance rejection control. 103
3.12 Simulation results without cyclic-disturbance rejection control (continued).104
3.13 Simulation results without cyclic-disturbance rejection control (continued).105
3.14 Simulation results without cyclic-disturbance rejection control (continued).106
3.15 Simulation results without cyclic-disturbance rejection control (continued).107
3.16 Simulation results with cyclic-disturbance rejection control. 108
3.17 Simulation results with cyclic-disturbance rejection control (continued). . 109
3.18 Simulation results with cyclic-disturbance rejection control (continued). . 110
3.19 Simulation results with cyclic-disturbance rejection control (continued). . 111
3.20 Simulation results with cyclic- disturbance rejection control (continued). 112

List of Tables

1.1 Geometric and mass properties of the 1.2-GW Abacus satellite 9
1.2 Solar pressure and microwave radiation disturbances 11
1.3 Orbit parameters and control requirements 13
1.4 A large single-gimbal CMG 14
1.5 A space-constructed, large-diameter momentum wheel [7] 14
1.6 Electric propulsion systems for the 1.2-GW Abacus satellite 19
1.7 Technology advancement needs for the Abacus SSPS 30

3.1 Electric propulsion systems for the 1.2-GW Abacus satellite 97

4.1 Technology advancement needs for the Abacus SSPS 115

Chapter 1

Introduction and Summary

This chapter provides an executive summary of this report. Detailed technical descriptions are provided in Chapters 2 and 3.

1.1 Report Outline

This report is intended to provide a coherent and unified framework for mathematical modeling, analysis, and control of very large Space Solar Power Satellites (SSPS) in geosynchronous orbit.

Chapter 1 presents a summary of major findings and results, and it can be read as an executive summary. Chapter 2 provides mathematical models for orbit, attitude, and structural dynamics analysis and control design. Chapter 3 presents an integrated orbit, attitude, and structural control system architecture, preliminary control analysis and design, and computer simulation results.

Chapters 2 and 3 also contain introductory sections on the basic definitions and fundamental concepts essential to mathematical modeling and control of space vehicles. These sections summarize many of the useful results in spacecraft dynamics and control, and they are primarily based on the material in *Space Vehicle Dynamics and Control*, Wie, B., AIAA Education Series, AIAA, Washington, DC, 1998.

Chapter 4 provides a summary of the study results and recommendations for future research.

Appendix A begins with a brief description of the general relationship for two-body motion, then provides an overview of Encke's method and how it is carried out in the computer program, and ends with a presentation of the expressions used in computing the various contributions to the perturbing forces exerted on the two bodies.

1.2 Evolution of Space Solar Power Satellites

A renewed interest in space solar power is spurring a reexamination of the prospects for generating large amounts of electricity from large-scale, space-based solar power systems. Peter Glaser [1], [2] first proposed the Satellite Solar Power Station (SSPS) concept in 1968 and received a U.S. patent on a conceptual design for such a satellite in 1973. As a result of a series of technical and economic feasibility studies by NASA and DOE in the 1970s, an SSPS reference system was developed in the late 1970s.

The 1979 SSPS reference system, as it is called, featured a very large solar array platform (5.3 $\times$ 10.7 km) and a gimballed, microwave beam transmitting antenna (1 km diameter). The total mass was estimated to be 50 $\times 10^6$ kg. A ground or ocean-based rectenna measuring 10 $\times$ 13 km would receive the microwave beam on the earth and deliver up to 5 GW of electricity.

In 1995, NASA revisited the Space Solar Power (SSP) concept to assess whether SSP-related technologies had advanced enough to alter significantly the outlook on the economic and technical feasibility of space solar power. The "Fresh Look" study, [3], conducted by NASA during 1995-1997 found that in fact a great deal had changed and that multi-megawatt SSP satellites appear viable, with strong space applications. The study also found that ambitious research, technology development and validation over a period of perhaps 15-20 years are required to enable SSP concepts to be considered "ready" for commercial development.

Recent studies by NASA as part of the SSP Exploratory Research and Technology (SERT) program have produced a variety of new configurations of Space Solar Power Satellites (SSPS) as reported in Refs. [4] and [5], and shown in Figure 1.1. Some of these configurations are based on the passive gravity-gradient stabilization concept. However, most other configurations require active three-axis attitude control to maintain continuous sun tracking of the solar arrays in the presence of external disturbances including the gravity-gradient torque. As illustrated in Figure 1.2, a cylindrical configuration, which is not affected by the troublesome pitch gravity-gradient torque, has also been considered by NASA [6].

Two other advanced concepts now under consideration by NASA [6] are shown in Figures 1.3 and 1.4. The Integrated Symmetrical Concentrator (ISC) concept, as illustrated in Figure 1.3, features ultralight-weight materials and structures which may greatly reduce the projected cost of SSPS. In this concept, mirrors would reflect and focus sunlight onto multi-bandgap, thin film photovoltaic arrays located next to a phased-array microwave transmitter. On the other hand, the Abacus/Reflector concept, as illustrated in Figure 1.4, is characterized by its simple configuration consisting of an inertially oriented, 3.2 $\times$ 3.2 km solar-array platform, a 500-m diameter microwave beam transmitting antenna fixed to the platform, and a 500 $\times$ 700 m rotating reflector that tracks the earth. This study focuses on the 1.2-GW Abacus SSPS configuration.

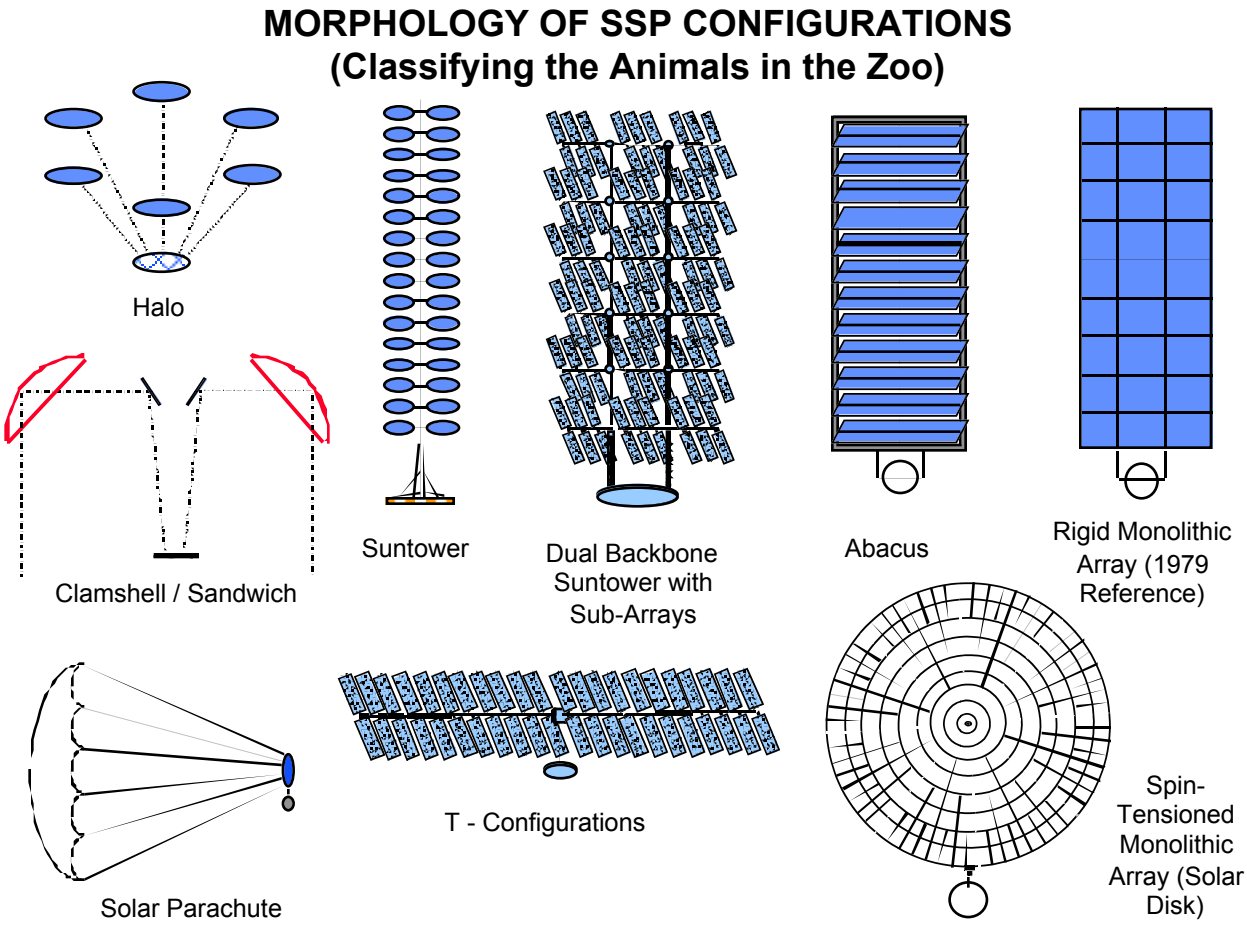

Figure 1.1: Morphology of various SSPS concepts (Moore [4], [5]).

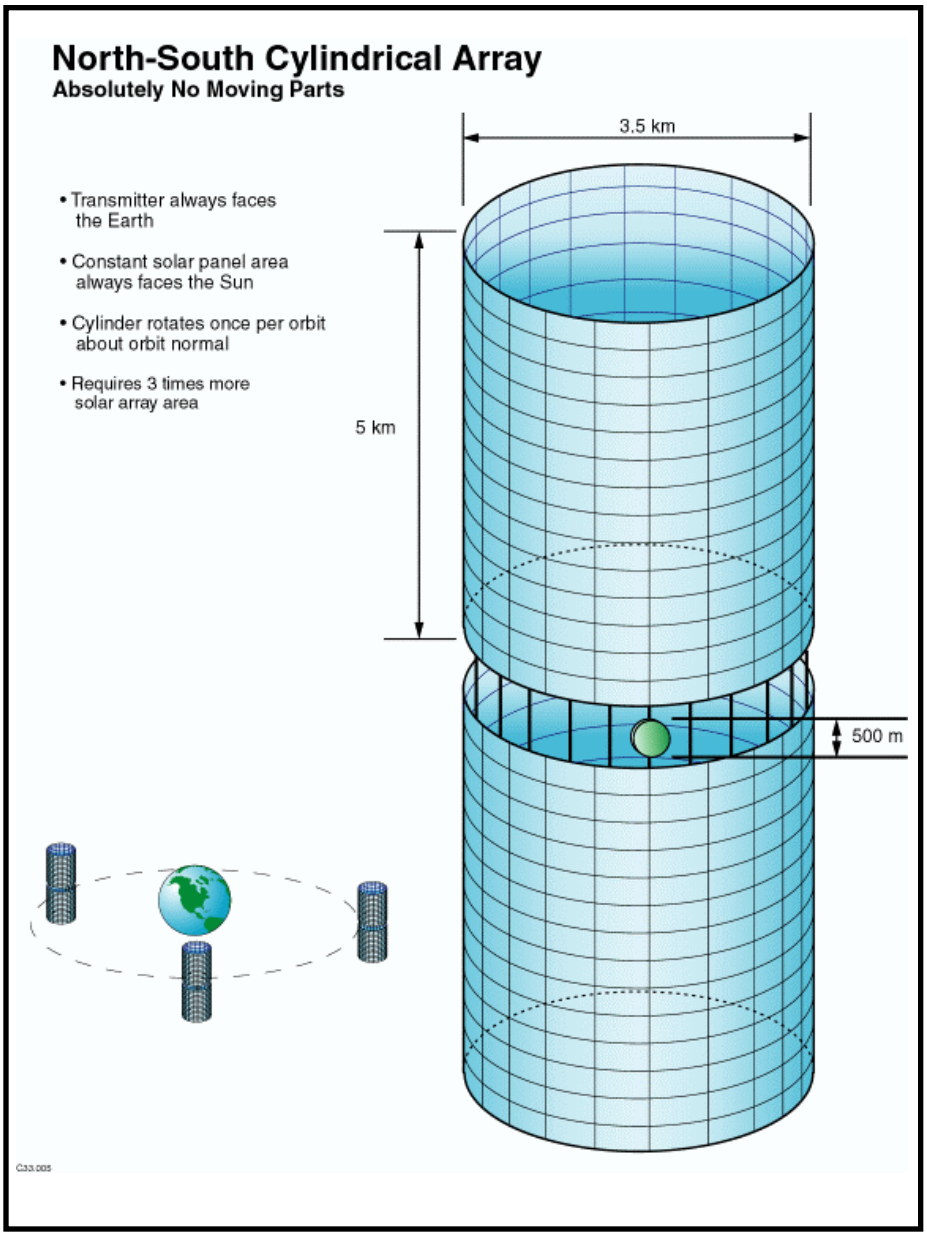

Figure 1.2: A cylindrical SSPS concept with zero pitch gravity-gradient torque (Carrington and Feingold [6]).

SERT Systems Integration, Analysis and Modeling

Integrated Symmetrical Concentrator

- Massive PMAD estimates motivated minimum PMAD configuration
- Geosynchronous equatorial orbit, mast POP
- Two primary mirror clamshells consisting of inflatable flat mirrors (focal length > 10 km) reflect sunlight onto two centrally-located PV arrays, <6X concentration ratio
- Energy converted to electrical @ PV arrays, distributed by cables to transmitter, converted to RF and transmitted to Earth
- Clamshells track sun (one rotation per day about boom metering structure, seasonal beta tilting), transmitter faces rectenna on ground

Concept sized for 1.2 GW delivered to Grid on Earth

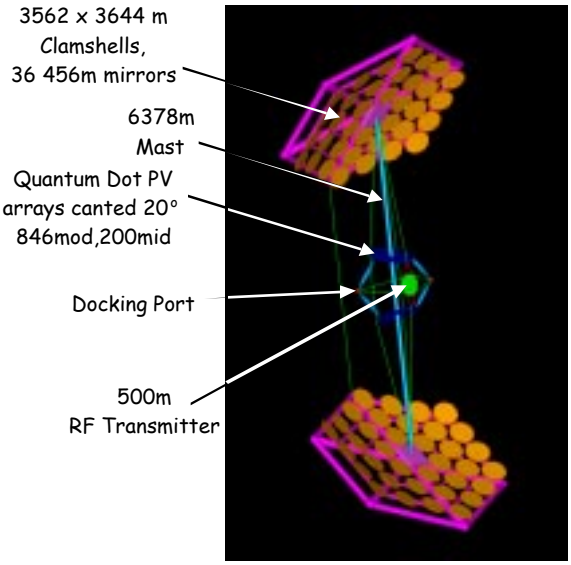

Figure 1.3: Integrated Symmetrical Concentrator concept (Carrington and Feingold [6]).

Abacus/Reflector Concept

Issues

- In-space construction, assembly, and or deployment of large (500m aperture) reflector
- Surface precision (λ/20-λ/40) required by reflector
- Management of reflector temperature and thermal stresses
- Azimuth roll-ring and activated links must provide stable platform for reflectors

Benefits

- Solar collectors always face Sun with very little, if any, shadowing.
- Solar concentrator uses shifting lens to accommodate seasonal beta-tracking, eliminates rotational joints between cells and abacus frame.
- Reflector design eliminates massive rotary joint and slip rings of 1979 Reference concept.
- Fixed orbital orientation allows continuous anti-Sun viewing for radiators.
- Abacus structural frame provides runs for PMAD cabling and permits "plug and play" solar array approach for assembly and maintenance.
- Triangular truss structure provides reasonable aspect ratio for abacus.
- Activated links provide reflector tilt for target latitude accessability
- Reduced rotational mass since rotating reflector structure can be made much lighter than large planar transmitter array

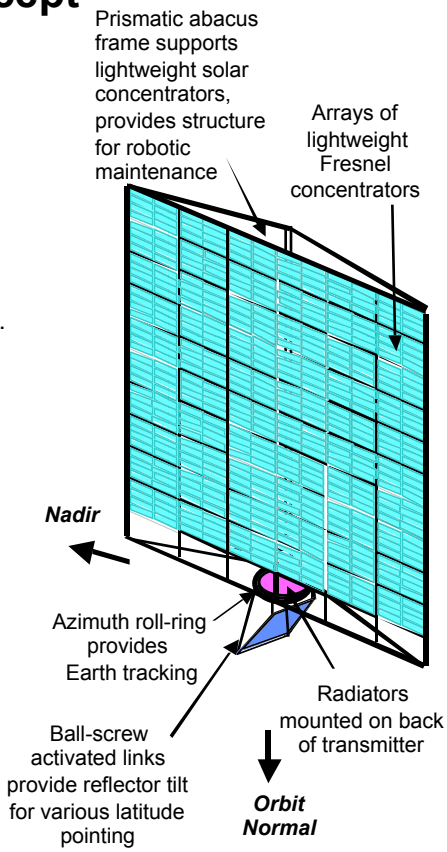

Figure 1.4: 1.2-GW Abacus/Reflector concept (Carrington and Feingold [6]).

1.3 Research Objectives and Tasks

The major objective of this study is to develop preliminary concepts for controlling orbit, attitude, and structural motions of very large Space Solar Power Satellites (SSPS) in geosynchronous orbit. This study focuses on the 1.2-GW Abacus SSPS configuration shown in Figure 1.4.

The research objectives and tasks of this study, in support of the SSP Exploratory Research and Technology (SERT) program of NASA, are as follows:

- Develop concepts for orbit, attitude, and structural control of very large Space Solar Power Satellites (SSPS) using a variety of actuators such as control moment gyros, momentum wheels, and electric propulsion thrusters
- Develop mathematical models, define a top-level control system architecture, and perform control systems design and analysis for a baseline Abacus SSPS configuration in geosynchronous orbit
- Determine the required number, size, placement, mass, and power for the actuators to control the orbit, attitude and structural motions of the baseline Abacus satellite. Also determine top-level estimates of attitude control system mass and propellant consumption per year
- Further explore advanced control technology toward achieving the mission requirements of future large space vehicles, and provide the space systems designer with options and approaches to meet the mission requirements of very large SSPS-type platforms

Because of the limited scope of this study, the following important topics are not studied in detail:

- Thermal distortion and structural vibrations due to solar heating
- Structural distortion due to gravity-gradient loading
- Autonomous stationkeeping maneuvers
- Simultaneous eccentricity and longitude control
- Attitude control during the solar eclipses
- Orbit and attitude control during assembly
- Attitude and orbit determination problem
- Reflector tracking and pointing control problem
- Electric propulsion systems
- Backup chemical propulsion systems

However, some of these important issues are discussed briefly at appropriate places throughout this report.

1.4 Abacus SSPS Configuration

This study focuses on the 1.2-GW Abacus SSPS concept, characterized by a huge (3.2 × 3.2 km) solar-array platform, a 500-m diameter microwave beam transmitting antenna, and a 500 × 700 m rotating reflector that tracks the earth. As illustrated in Figure 1.4, some unique features of the Abacus satellite relative to the 1979 SSPS reference system, can be described as follows:

- The transmitting antenna is not gimballed; instead, an azimuth roll-ring mounted, rotating reflector provides earth pointing of the microwave beam.
- The rotating reflector design thus eliminates massive rotary joint and slip rings of the 1979 SSPS reference concept.
- Ball-screw activated links provide reflector tilt for various latitude pointing.

1.4.1 Geometric Properties

The three major parts of the Abacus satellite and their dimensions are shown in Figure 1.5; the mass of each part is given in Table 1.1, together with the total mass and area of the spacecraft. The mass of the reflector is approximately 3% of the total mass; therefore, the reflector's mass can be neglected in the analysis of attitude motion, simplifying the task in two important respects. First, the Abacus satellite can be treated as a single body rather than a multibody spacecraft. When the Abacus satellite is regarded as rigid, as is the case in Sec. 2.3, the spacecraft's moments and products of inertia for a set of axes fixed in the solar array do not vary with time. Second, when the unsymmetrical mass distribution of the reflector is left out of account, the principal axes of inertia of the spacecraft with respect to the spacecraft's mass center are parallel to the roll, pitch, and yaw axes illustrated in Figure 1.5. The moments of inertia for these axes, henceforth considered to be principal moments of inertia, are given in Table 1.1.

The center of pressure is located 100 m below the geometric center of the square platform, and the center of mass is located 300 m below the geometric center along the pitch axis. The mass of individual components, in units of metric tons, can be found in Figure 1.6.

1.4.2 External Disturbances

External disturbances acting on the Abacus satellite include: solar radiation pressure force, microwave radiation force, gravity-gradient torque, and other orbit perturbation forces. Some of these disturbances are summarized in Table 1.2. Disturbance torques in units of N-m due to solar pressure, microwave radiation, cm-cp offset, and cm/cp location uncertainty can be expressed along the principal axes as:

Table 1.1: Geometric and mass properties of the 1.2-GW Abacus satellite

Solar array mass	21 $\times 10^6$ kg
Transmitting antenna mass	3×10^6 kg
Reflector mass	0.8×10^6 kg
Total mass	m = 25×10^6 kg
Platform area	A = 3200 m $\times$ 3200 m
Area-to-mass ratio	A/m = 0.4 m^2/kg
Roll inertia	$J_1 = 2.8 \times 10^{13}$ kg-m^2
Pitch inertia	$J_2 = 1.8 \times 10^{13}$ kg-m^2
Yaw inertia	$J_3 = 4.6 \times 10^{13}$ kg-m^2
cm-cp offset	200 m (along pitch axis)
cm-cp offset (uncertainty)	$\pm$20 m (along roll axis)

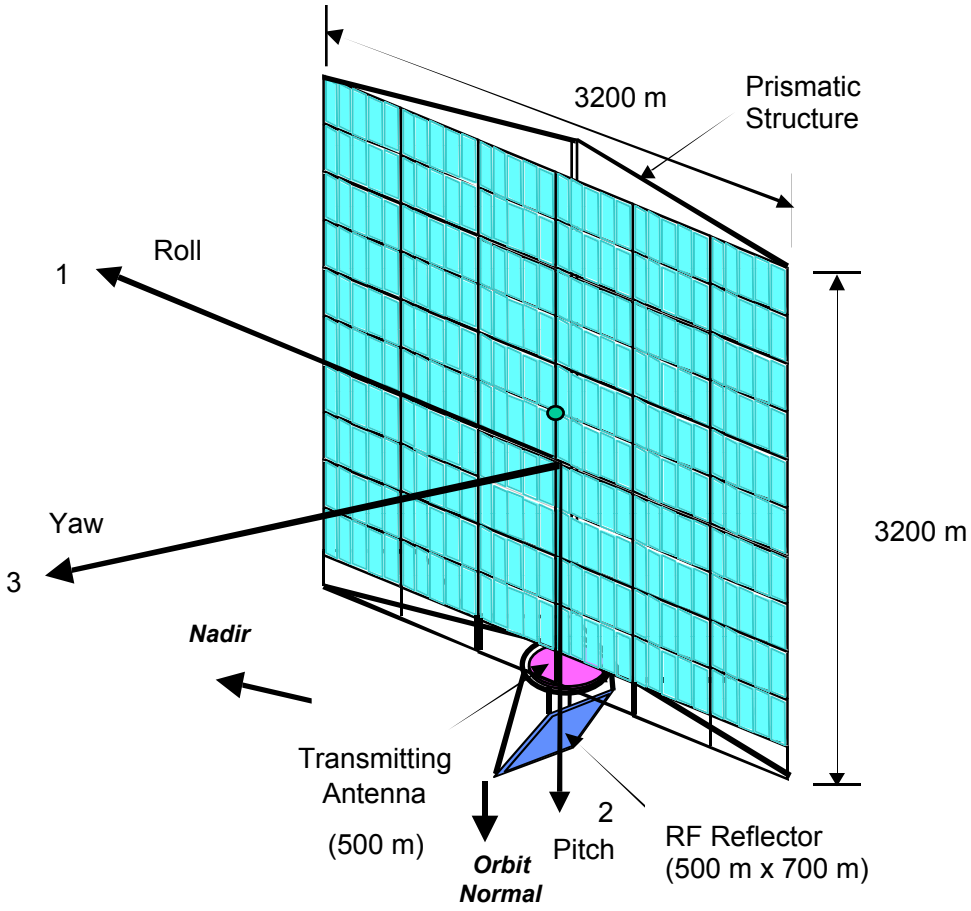

Figure 1.5: Baseline 1.2-GW Abacus satellite.

Abacus/Reflector Concept

ENTECH Concentrators, Solid State, 1200 MW Delivered from GEO

System Element	*Mass (MT)*	*Comments*
RF Transmitter Array		Devices, Structure; Input Power = 3614 MWe
Transmitter Elements	1156	Diameter = 500 meters; 83903 Thousand Solid State Devices
Transmitter Planar Array	1612	Mass = 8.21 kg/m2
Transmitter Array Structure	281	Composite Truss Structure @ 1.43 kg/m2
Reflector and Bearing Struct	844	Only Applicable to Reflector Concepts
Transmitter Thermal Control	0	Integrated, Some TC Included in Transmitter Element Mass
Add'l Structure Allowance	117	Allowance = 3%
Solar Conversion		SLA, 1 wing(s) with array dimensions = 1772 m x 6200 m
Solar Concentrators/Arrays	4317	Unit Height = 40 m, Width = 200 m, Mass = 3.664 MT, Power = 3.346 MW
Add'l Structure Allowance	129	Allowance = 3%
Telecomm & Command	3	One set per solar array node (38 sets)
Add'l Structure Allowance	0	Allowance = 3%
Integrating Structure	3563	Abacus, Total Length = 1772 meters
PMAD		Cabling & Power Conversion, SPG Power = 3941 MWe; Advanced PMAD
Cabling	173	Total Length = 3162 km @ 0.055 kg/m, Voltage = 100 kV
Array Converter Mass	3544	Mass based on 1178 Converters (1000 V to 100 kV), 3.346 MW Power Out
Transmitter PMAD Mass	4362	Mass Includes Voltage Convertors, Switches, Harness & PMAD Thermal , 3.61 GW
Rotary Joints, Switches, Etc.	1	Thruster Switches Only
Attitude Control/Pointing		Sensors, Computers, Control Effectors
Dry Mass	452	Thrusters, CMG's, Sensors etc. at each solar collector
Propellant	665	Delta V = 50 m/s per year for 10 years
Add'l Structure Allowance	14	Allowance = 3%
SEP Propulsion	831	LEO-GEO Transfer Stages
Dry Mass	3815	Thruster Power = 50 kWe (8 Hall Thrusters, Isp = 2000 sec)
Propellant	7361	Krypton
Add'l Structure Allowance	114	Allowance = 3%
Expendable Solar Arrays	664	Thin Film Arrays, 500 W/kg
Payload Mass	0	
Satellite Launched Mass (MT)	33187	ETO Payloads = 40 MT per launch (830 Launches)
Satellite Orbited Mass (MT)	25162	At 35786 km

Rectenna Diameter (m) 7450

Harvey Feingold 5/26/00

Figure 1.6: Mass breakdown of Abacus components (Carrington and Feingold [6]).

Table 1.2: Solar pressure and microwave radiation disturbances

Solar pressure force	(4.5E-6)(1.3)(A) = 60 N
Solar-pressure-induced acceleration	(4.5E-6)(1.3)(A/m) = 2.4 $\times 10^{-6}$ m/s^2
Solar pressure torque (roll)	60 N $\times$ 200 m = 12,000 N-m
Solar pressure torque (pitch)	60 N $\times$ 20 m = 1,200 N-m
Transmitter/reflector radiation force	7 N (rotating force)
Transmitter/reflector radiation torque	7 N $\times$1700 m = 11,900 N-m

$$\begin{aligned} \text{Roll: } & d_1 \approx 12,000 - 11,900 \cos nt \\ \text{Pitch: } & d_2 \approx 1,200 \\ \text{Yaw: } & d_3 \approx -11,900 \sin nt \end{aligned}$$

where n is the orbital rate of the Abacus satellite, and t is time. The constant pitch disturbance torque of 1,200 N-m is due to the assumed cm-cp offset uncertainty of 20 m along the roll axis. In addition to these disturbances, gravity-gradient disturbance torques are also acting on the Abacus satellite. It is assumed that the electric currents circulate in the solar array structure in such a way that magnetic fields cancel out and the Abacus satellite is not affected by the magnetic field of the earth.

1.4.3 Orbit Parameters and Control Requirements

To describe a satellite orbit about the earth, we often employ six scalars, called the six orbital elements. Three of these scalars specify the orientation of the orbit plane with respect to the geocentric-equatorial reference frame, also called the Earth-Centered Inertial (ECI) reference system, which has its origin at the center of the earth, as shown in Figure 1.7. Note that this reference frame is not fixed to the earth and is not rotating with it; rather the earth rotates about it. The (X, Y) plane of the geocentric-equatorial reference frame is the earth's equatorial plane, simply called the equator. The Z-axis is along the earth's polar axis of rotation. The X-axis is pointing toward the *vernal equinox*, the point in the sky where the sun crosses the equator from south to north on the first day of spring. The vernal equinox direction is often denoted by the symbol Υ.

The six classical orbital elements consist of five independent quantities which are sufficient to completely describe the size, shape, and orientation of an orbit, and one quantity required to pinpoint the position of a satellite along the orbit at any particular time, as also illustrated in Figure 1.7.

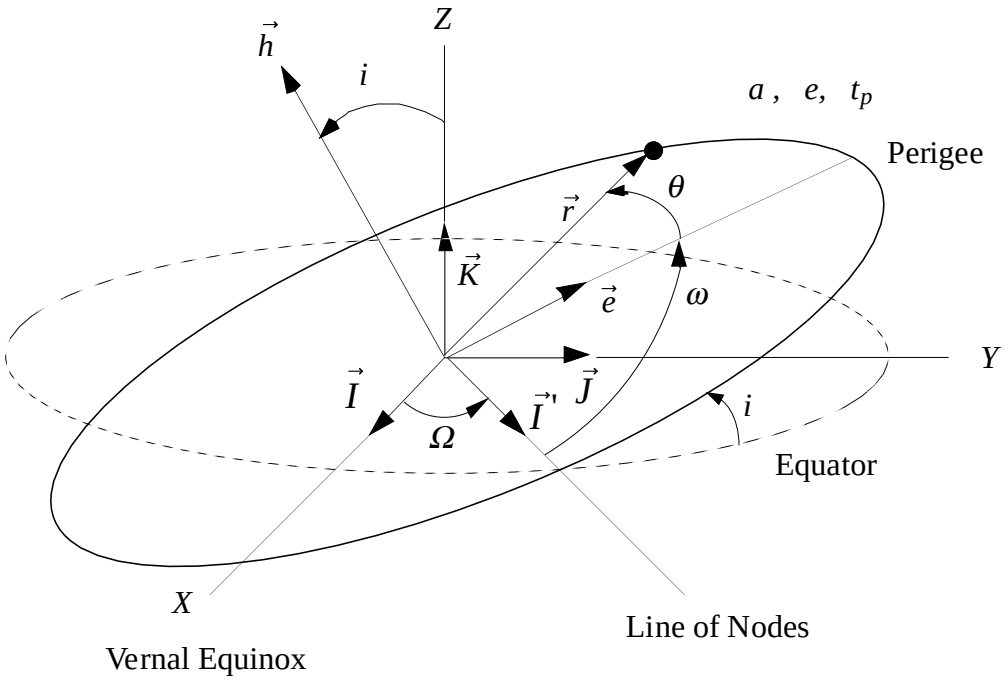

Figure 1.7: Orbit orientation with respect to the geocentric-equatorial reference frame, also called the Earth-Centered Inertial (ECI) reference system. A near circular orbit is shown in this figure.

Six such classical orbital elements are:

$a =$ the semimajor axis
$e =$ the eccentricity
$i =$ the inclination of the orbit plane
$\Omega =$ the right ascension or longitude of the ascending node
$\omega =$ the argument of the perigee
$M =$ the mean anomaly

A traditional set of the six classical orbital elements includes the perigee passage time instead of the mean anomaly. The elements a and e determine the size and shape of the elliptic orbit, respectively, and t_p or M relates position in orbit to time. The angles Ω and i specify the orientation of the orbit plane with respect to the geocentric-equatorial reference frame. The angle ω specifies the orientation of the orbit in its plane.

Basic orbital characteristics and control requirements for the Abacus satellite in geosynchronous orbit are summarized in Table 1.3.

Table 1.3: Orbit parameters and control requirements

Earth's gravitational parameter	μ = 398,601 km^3/s^2
Geosynchronous orbit ($e, i \approx 0$)	a = 42,164 km
Orbit period	23 hr 56 min 4 sec = 86,164 sec
Orbit rate	n = 7.292 $\times 10^{-5}$ rad/sec
Longitude location	TBD
Stationkeeping accuracy	$\pm$0.1 deg (longitude/latitude)
Solar array pointing accuracy	$\pm$0.5 deg for roll/pitch axes
Microwave beam pointing accuracy	$\pm$5 arcmin

1.5 Major Findings and Results

In this section, a summary of major findings and results from this study is presented. Detailed technical discussions of the development of mathematical models and a control system architecture will be presented in Chapters 2 and 3.

1.5.1 Technical Issues

Momentum Storage Requirement

Assuming that the gravity-gradient torque is the only external disturbance torque acting along the pitch axis, we consider the pitch equation of motion of the Abacus satellite in geosynchronous orbit given by

$$J_2\ddot{\theta}_2 = \frac{3n^2}{2}(J_3 - J_1)\sin 2\theta_2 + u_2 \tag{1}$$

where J_1, J_2, and J_3 are, respectively, the roll, pitch, and yaw principal moments of inertia; θ_2 is the pitch angle measured from the LVLH (local vertical and local horizontal) reference frame; n is the orbit rate; and u_2 is the pitch control torque.

For continuous sun pointing of the Abacus satellite with $\theta_2 = nt$, the pitch control torque required to counter the cyclic gravity-gradient torque simply becomes

$$u_2 = -\frac{3n^2}{2}(J_3 - J_1)\sin 2nt \tag{2}$$

with peak values of $\pm$143,000 N-m. If angular momentum exchange devices, such as momentum wheels (MWs) or control moment gyros (CMGs), are to be employed for pitch control, the peak angular momentum to be stored can then be estimated as

$$H_{\max} = \frac{3n}{2}(J_3 - J_1) = 2 \times 10^9 \ \text{ N-m-s} \tag{3}$$

Table 1.4: A large single-gimbal CMG

Cost	$1M
Momentum	7,000 N-m-s
Max torque	4,000 N-m
Peak power	500 W
Mass	250 kg
Momentum/mass	28 N-m-s/kg

Table 1.5: A space-constructed, large-diameter momentum wheel [7]

Momentum = 4×10^8 N-m-s	Rim radius = 350 m
Max torque = 30,000 N-m	Mass = 6000 kg
Material = aluminum	Max power = 19 kW
Natural frequency = 0.22 Hz	Max speed = 6 rpm
Momentum/mass = 66,000 N-m-s/kg	cost = TBD

This is is about 100,000 times the angular momentum storage requirement of the International Space Station (ISS). The ISS is to be controlled by four double-gimballed CMGs with a total momentum storage capability of about 20,000 N-m-s. The double-gimballed CMGs to be employed for the ISS have a momentum density of 17.5 N-m-s/kg, and future advanced flywheels may have a larger momentum density of 150 N-m-s/kg. Basic characteristics of a large single-gimbal CMG are also summarized in Table 1.4.

Based on the preceding discussion, it can be concluded that a traditional momentum management approach using conventional CMGs (or even employing future advanced flywheels) is not a viable option for controlling very large Space Solar Power Satellites.

To meet the momentum storage requirement of very large SSPS, a concept of constructing large-diameter momentum wheels in space has been studied in the late 1970s [7]. An example of such space-assembled, large-diameter wheels is summarized in Table 1.5. About 5 to 7 such large-diameter momentum wheels are required for the Abacus satellite. The concept of lightweight, space-assembled (or deployable, inflatable) large-diameter momentum wheels merits further study, but is beyond the scope of the present report.

In an attempt to resolve the angular momentum storage problem of large sun-pointing spacecraft, a quasi-inertial sun-pointing, pitch control concept was developed by Elrod [8] in 1972, and further investigated by Juang and Wang [9] in 1982. However, such a "free-drift" concept is not a viable option for the Abacus satellite because of the large pitch attitude peak error of 18.8 deg and its inherent sensitivity with respect to initial phasing and other orbit perturbations.

Because the pitch gravity-gradient torque becomes naturally zero for cylindrical, spherical or beam-like satellites with $J_1 = J_3$, a cylindrical SSPS configuration was also studied by NASA (see Figure 1.2) to simply avoid such a troublesome pitch gravity-gradient torque problem.

Solar Radiation Pressure and Large Area-to-Mass Ratio

Despite the importance of the cyclic pitch gravity-gradient torque, this study shows that the solar radiation pressure force is considerably more detrimental to control of the Abacus satellite (and other large SSPS) because of an area-to-mass ratio that is very large compared to contemporary, higher-density spacecraft.

The significant orbit perturbation effect of the solar pressure force on large spacecraft with large area-to-mass ratios has been investigated by many researchers in the past [10]-[15]. A detailed physical description of the solar radiation pressure can be found in a recent book on solar sailing by McInnes [14]. The solar pressure effects on formation flying of satellites with different area-to-mass ratios were also recently investigated by Burns et al. [15].

For typical geosynchronous communications satellites, we have

Area-to-mass ratio $A/m \approx 0.02$ m^2/kg
Solar pressure perturbation acceleration $\approx 0.12 \times 10^{-6}$ m/s^2
$\Delta e = \dfrac{3\pi(4.5 \times 10^{-6})(1.3)A/m}{n^2 a} \approx 4.9 \times 10^{-6}$ per day
Earth's gravitational acceleration $= 0.224$ m/s^2
Earth's oblateness J_2 perturbation $= 2.78 \times 10^{-6}$ m/s^2
Solar gravitational perturbation $< 4 \times 10^{-6}$ m/s^2
Lunar gravitational perturbation $< 9 \times 10^{-6}$ m/s^2
$\Rightarrow$ Stationkeeping $\Delta V \approx 50$ m/sec per year
$\Rightarrow \Delta m = m\left(1 - \exp\left(-\dfrac{\Delta V}{g I_{sp}}\right)\right) \approx 17$ kg/year
where m is assumed as 1000 kg, $g = 9.8$ m/s^2, $I_{sp} = 300$ sec

For the Abacus satellite, however, we have

Area-to-mass ratio $A/m \approx 0.4$ m^2/kg
Solar pressure force ≈ 60 N
Solar pressure perturbation acceleration $\approx 2.4 \times 10^{-6}$ m/s^2
Earth's gravitational acceleration $= 0.224$ m/s^2
Earth's oblateness J_2 perturbation $= 2.78 \times 10^{-6}$ m/s^2
Solar gravitational perturbation $< 4 \times 10^{-6}$ m/s^2

Lunar gravitational perturbation $< 9 \times 10^{-6}$ m/s^2

$$\Delta e = \frac{3\pi(4.5 \times 10^{-6})(1.3)A/m}{n^2 a} \approx 1 \times 10^{-4} \text{ per day}$$

$\Rightarrow$ Longitude drift $\Delta\lambda = 2\Delta e \approx 0.0115$ deg/day

$\Rightarrow$ maximum $\Delta e \approx 0.018$ at the mid year

$\Rightarrow$ maximum $\Delta\lambda = 2\Delta e \approx 2$ deg; maximum $\Delta a \approx 1.8$ km

$\Rightarrow$ Orbit eccentricity control is necessary

$$\Rightarrow \Delta m = \frac{(60)(24 \times 3600 \times 365)}{5000 \times 9.8} \approx 40,000 \text{ kg/year with } I_{sp} = 5000 \text{ sec}$$

Typical north-south and east-west stationkeeping maneuvers for the Abacus satellite will also require

$$\Delta m = m\left(1 - \exp\left(-\frac{\Delta V}{g I_{sp}}\right)\right) \approx 30,000 \text{ kg/year}$$

where $m = 25 \times 10^6$ kg, $\Delta V = 50$ m/s per year, $g = 9.8$ m/s^2, and $I_{sp} = 5000$ sec.

The results of 30-day simulations of orbital motion of the Abacus satellite, with the effects of the earth's oblateness and triaxiality, luni-solar perturbations, and 60-N solar pressure force included, are shown in Figures 1.8 and 1.9. It is worth noting the extent to which eccentricity and inclination are perturbed.

The initial values used in the simulations correspond to a circular, equatorial orbit of radius 42164.169 km; therefore, the initial orbital elements are

$$\begin{aligned} a &= 42164.169 \text{ km} \\ e &= 0 \\ i &= 0 \text{ deg} \\ \Omega &= 0 \text{ deg} \\ \omega &= 0 \text{ deg} \end{aligned}$$

The epoch used to calculate the solar and lunar positions, as well as the Earth's orientation in inertial space, is March 21, 2000. In order to place the spacecraft at an initial terrestrial longitude of 75.07 deg (one of the stable longitudes), a true anomaly θ of 253.89 deg is used.

These elements correspond to an initial position and velocity of

$$\begin{aligned} \vec{r} &= -11698.237\,\vec{I} - 40508.869\,\vec{J} + 0\vec{K} \text{ km} \\ \vec{v} &= \quad 2.954\,\vec{I} - \quad 0.853\,\vec{J} + 0\vec{K} \text{ km/s} \end{aligned}$$

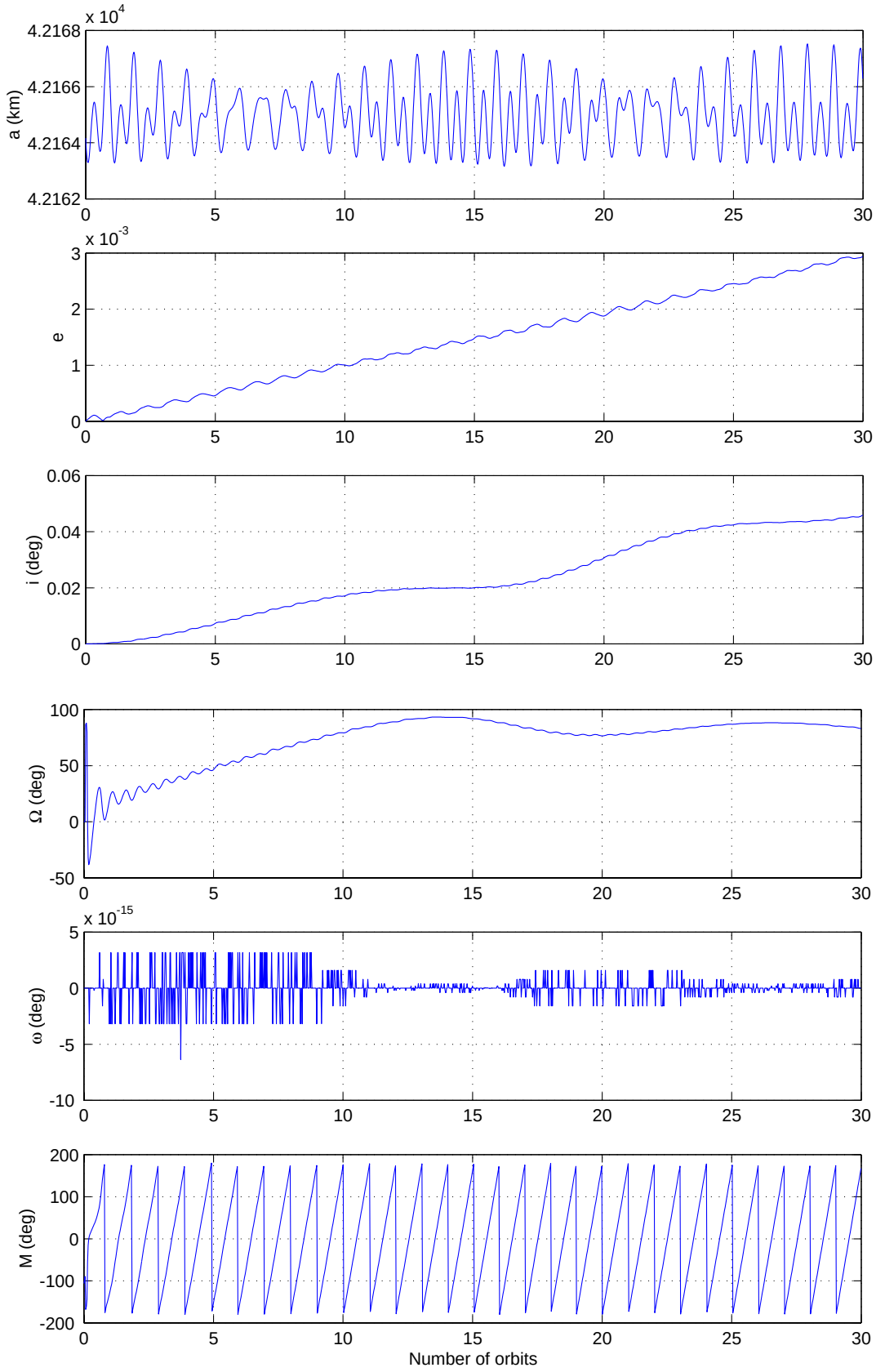

Figure 1.8: Orbit simulation results with the effects of the earth's oblateness and triaxiality, luni-solar perturbations, and 60-N solar radiation pressure force.

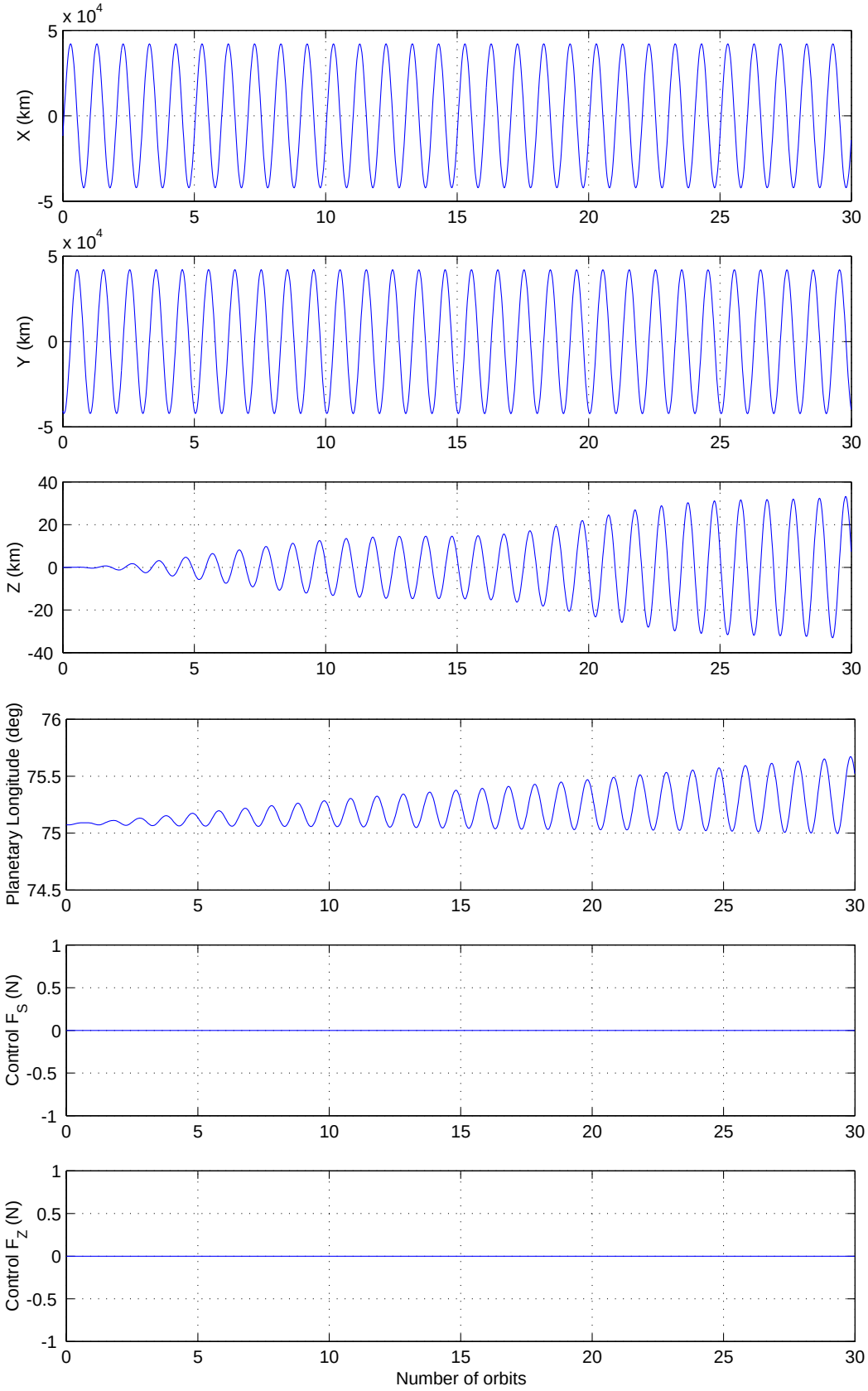

Figure 1.9: Orbit simulation results with the effects of the earth's oblateness and triaxiality, luni-solar perturbations, and 60-N solar radiation pressure force (continued).

Table 1.6: Electric propulsion systems for the 1.2-GW Abacus satellite

Thrust, T	$\geq$ 1 N
Specific impulse, $I_{sp} = T/(\dot{m}g)$	$\geq$ 5,000 sec
Exhaust velocity, $V_e = I_{sp}g$	$\geq$ 49 km/s
Total efficiency, $\eta = P_o/P_i$	$\geq$ 80%
Power/thrust ratio, P_i/T	$\leq$ 30 kW/N
Mass/power ratio	$\leq$ 5 kg/kW
Total peak thrust	200 N
Total peak power	6 MW
Total average thrust	80 N
Total average power	2.5 MW
Number of 1-N thrusters	$\geq$ 500
Total dry mass	$\geq$ 75,000 kg
Propellant consumption	85,000 kg/year

Note: $T = \dot{m}V_e$, $P_o = \frac{1}{2}\dot{m}V_e^2 = \frac{1}{2}TV_e$, $P_o/T = \frac{1}{2}V_e$ = ideal power/thrust ratio, $P_i/T = \frac{1}{2\eta}V_e$, $I_{sp} = T/(\dot{m}g) = V_e/g$, $V_e = I_{sp}g$ where $g = 9.8$ m/s^2, $\dot{m}$ is the exhaust mass flow rate, P_i is the input power, and P_o is the output power.

1.5.2 Control Systems Architecture

The preceding section illustrates the consequences of solar pressure acting on a spacecraft with a large area-to-mass ratio. If left uncontrolled, this can cause a cyclic drift in the longitude of the Abacus satellite of 2 deg, east and west. Thus, in addition to standard north-south and east-west stationkeeping maneuvers for $\pm$0.1 deg orbit position control, active control of the orbit eccentricity using electric thrusters with high specific impulse, I_{sp}, becomes mandatory. Furthermore, continuous sun tracking of the Abacus satellite requires large control torques to counter various disturbance torques. A control systems architecture developed in this study utilizes properly distributed ion thrusters to counter, simultaneously, the cyclic pitch gravity-gradient torque and solar radiation pressure.

Electric Propulsion Systems

Basic characteristics of electric propulsion systems proposed for the Abacus satellite are summarized in Table 1.6. Approximately 85,000 kg of propellant per year is required for simultaneous orbit, attitude, and structural control using 500 1-N electric propulsion thrusters with $I_{sp} = 5{,}000$ sec. The yearly propellant requirement is reduced to 21,000 kg if an I_{sp} of 20,000 sec can be achieved. As I_{sp} is increased, the propellant mass decreases but the electric power requirement increases; consequently, the mass of solar arrays and power processing units increases. Based on 500 1-N thrusters, a mass/power ratio of 5 kg/kW, and a power/thrust ratio of 30 kW/N, the total dry mass (power processing

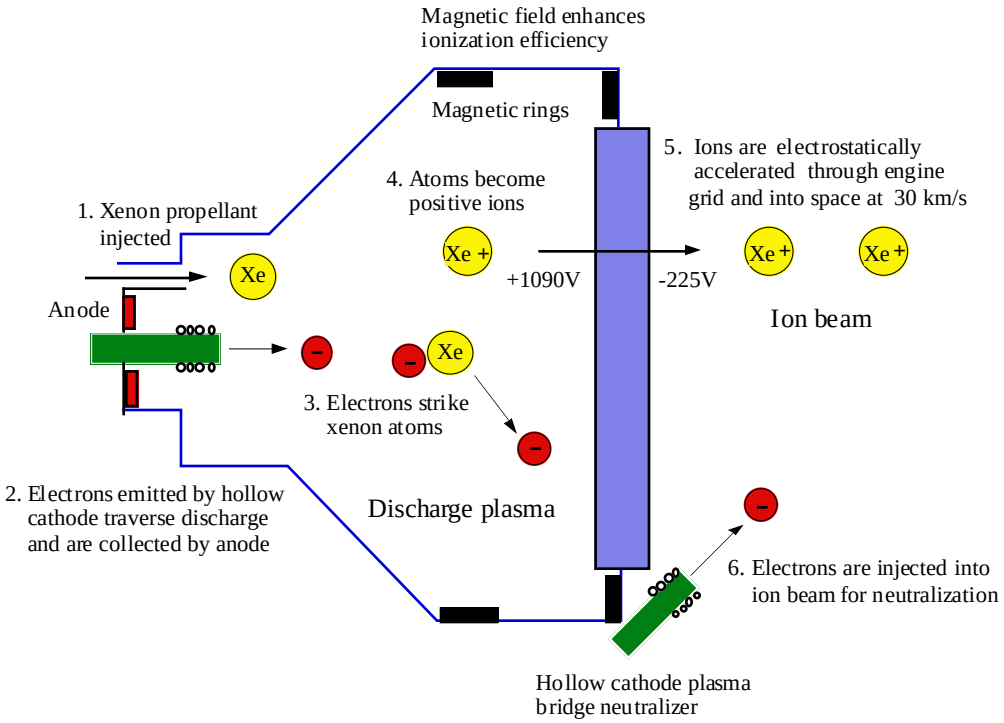

Figure 1.10: A schematic illustration of the NSTAR 2.3-kW, 30-cm diameter ion thruster on Deep Space 1 Spacecraft (92-mN maximum thrust, specific impulse ranging from 1,900 to 3,200 sec, 25 kW/N, overall efficiency of 45–65%).

units, thrusters, tanks, feed systems, etc.) of electric propulsion systems proposed for the Abacus satellite is estimated as 75,000 kg.

A schematic illustration of the 2.3-kW, 30-cm diameter ion engine on the Deep Space 1 spacecraft is given in Figure 1.10, which is formally known as NSTAR, for NASA Solar electric propulsion Technology Application Readiness system. The maximum thrust level available from the NSTAR ion engine is about 92 mN and throttling down is achieved by feeding less electricity and xenon propellant into the propulsion system. Specific impulse ranges from 1,900 sec at the minimum throttle level to 3,200 sec.

In principle, an electric propulsion system employs electrical energy to accelerate ionized particles to extremely high velocities, giving a large total impulse for a small consumption of propellant. In contrast to standard propulsion, in which the products of chemical combustion are expelled from a rocket engine, ion propulsion is accomplished by giving a gas, such as xenon (which is like neon or helium, but heavier), an electrical charge and electrically accelerating the ionized gas to a speed of about 30 km/s. When xenon ions are emitted at such high speed as exhaust from a spacecraft, they push the spacecraft in the opposite direction. However, the exhaust gas from an ion thruster consists of large numbers of positive and negative ions that form an essentially neutral plasma beam extending for large distances in space. It seems that little is known yet about the long-term effect of such an extensive plasma on geosynchronous satellites.

Orbit, Attitude, and Structural Control Systems

A control systems architecture developed in this study is shown in Figure 1.11. The proposed control systems utilize properly distributed ion thrusters to counter, simultaneously, the cyclic pitch gravity-gradient torque, the secular roll torque caused by cm-cp offset and solar pressure, the cyclic roll/yaw microwave radiation torque, and the solar pressure force whose average value is 60 N. A control-structure interaction problem of the Abacus platform with the lowest structural mode frequency of 0.002 Hz is avoided simply by designing an attitude control system with very low bandwidth ($<$ orbit frequency). However, the proposed low-bandwidth attitude control system utilizes a concept of cyclic-disturbance accommodating control to provide ± 5 arcmin pointing of the Abacus platform in the presence of large external disturbances and dynamic modeling uncertainties. High-bandwidth, colocated direct velocity feedback, active dampers may need to be properly distributed over the platform.

Placement of a minimum of 500 1-N electric propulsion thrusters at 12 different locations is illustrated in Figure 1.12. In contrast to a typical placement of thrusters at the four corners, e.g., employed for the 1979 SSPS reference system, the proposed placement shown in Figure 1.12 minimizes roll/pitch thruster couplings as well as the excitation of platform out-of-plane bending modes. A minimum of 500 ion engines of 1-N thrust level are required for simultaneous attitude and stationkeeping control. When reliability, lifetime, duty cycle, lower thrust level, and redundancy of ion engines are considered, this number will increase significantly.

1.5.3 Attitude and Orbit Control Simulation Results

Computer simulation results of a case with initial attitude errors of 10 deg in the presence of various dynamic modeling uncertainties (e.g., $\pm 20\%$ uncertainties in moments and products of inertia, cm location, principal axes, etc.) are shown in Figure 1.13. The proposed low-bandwidth attitude control system utilizing the concept of cyclic-disturbance accommodating control meets the ± 5 arcmin pointing requirement of the Abacus platform in the presence of large external disturbances and dynamic modeling uncertainties. Proper roll/pitch thruster firings needed for simultaneous eccentricity and roll/pitch attitude control can be seen in Figure 1.14. Nearly linear control forces are generated by on-off modulation of individual 1-N thrusters, as can be seen in Figure 1.14. The total thrusting force from the roll/pitch thrusters #1 through #4 nearly counters the 60-N solar pressure force.

Orbit control simulation results with the effects of the earth's oblateness and triaxiality, luni-solar perturbations, 60-N solar pressure force, and simultaneous orbit and attitude control thruster firings are shown in Figures 1.16 and 1.17. In Figure 1.17, F_Z is the orbit inclination control force and F_X is the solar pressure countering control force. It can be seen that the inclination, eccentricity, satellite longitude location, and the Z-axis orbit position are all properly maintained.

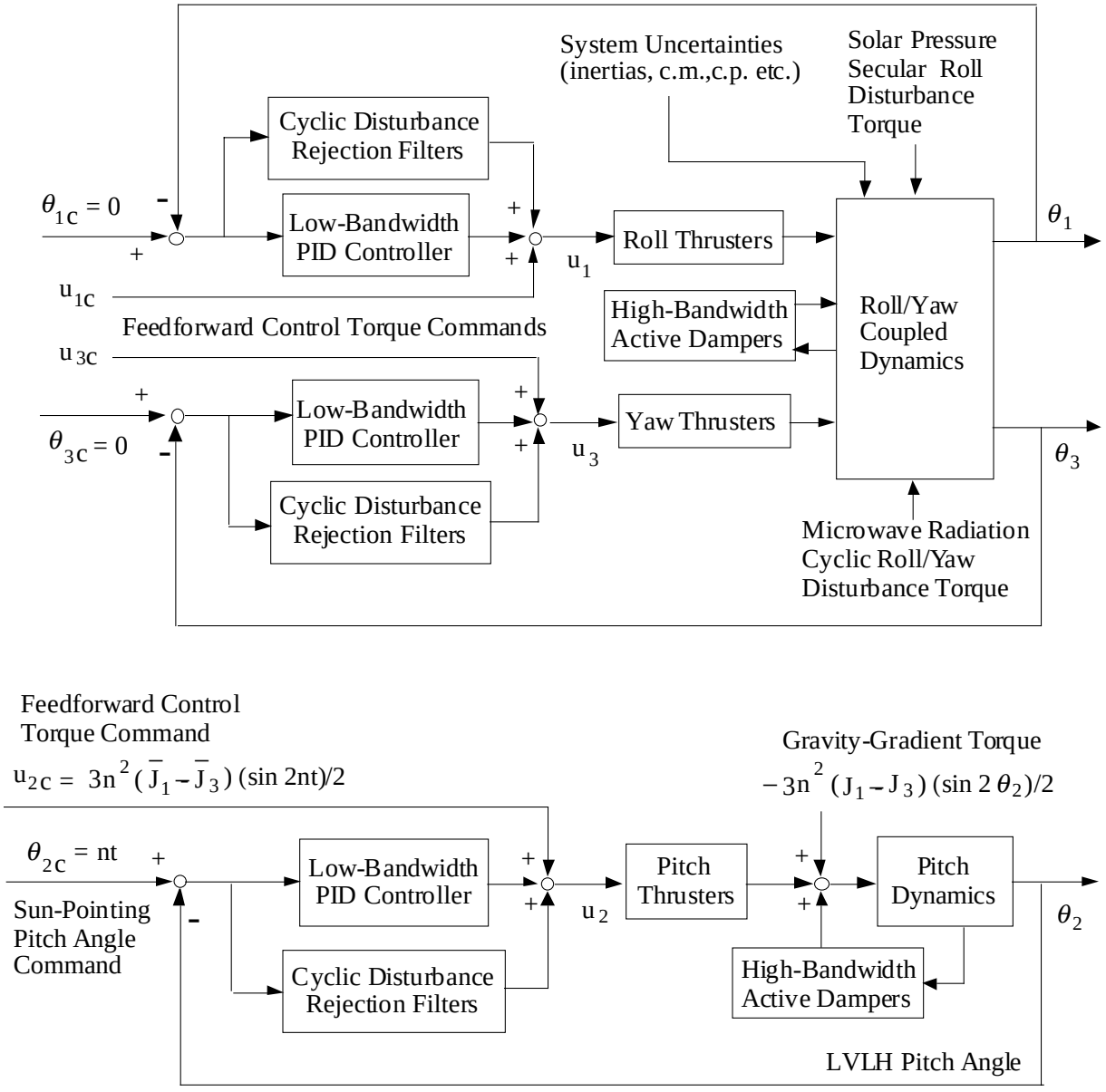

Figure 1.11: An integrated orbit, attitude, and structural control system architecture employing electric propulsion thrusters.

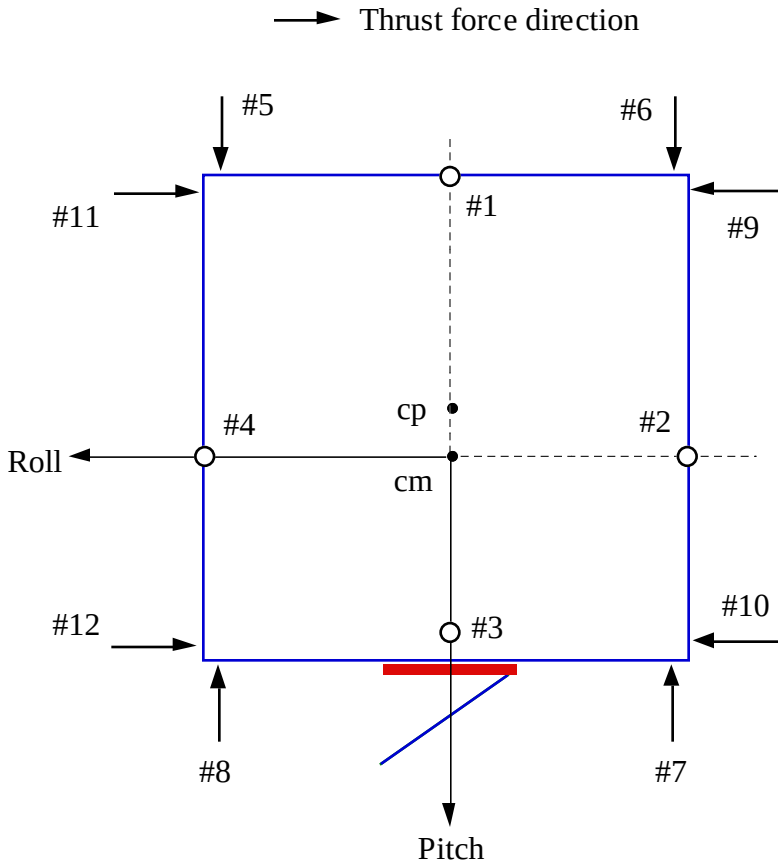

Roll: 1/3 Pitch: 2/4 Yaw: 5/6/7/8

Orbit Eccentricity, Roll/Pitch Control: 1/3, 2/4

E/W and Yaw Control: 9/10/11/12

N/S and Yaw Control: 5/6/7/8

Figure 1.12: Placement of a minimum of 500 1-N electric propulsion thrusters at 12 different locations, with 100 thrusters each at locations #2 and #4. (Note: In contrast to a typical placement of thrusters at the four corners, e.g., employed for the 1979 SSPS reference system, the proposed placement of roll/pitch thrusters at locations #1 through #4 minimizes roll/pitch thruster couplings as well as the excitation of platform out-of-plane bending modes.)

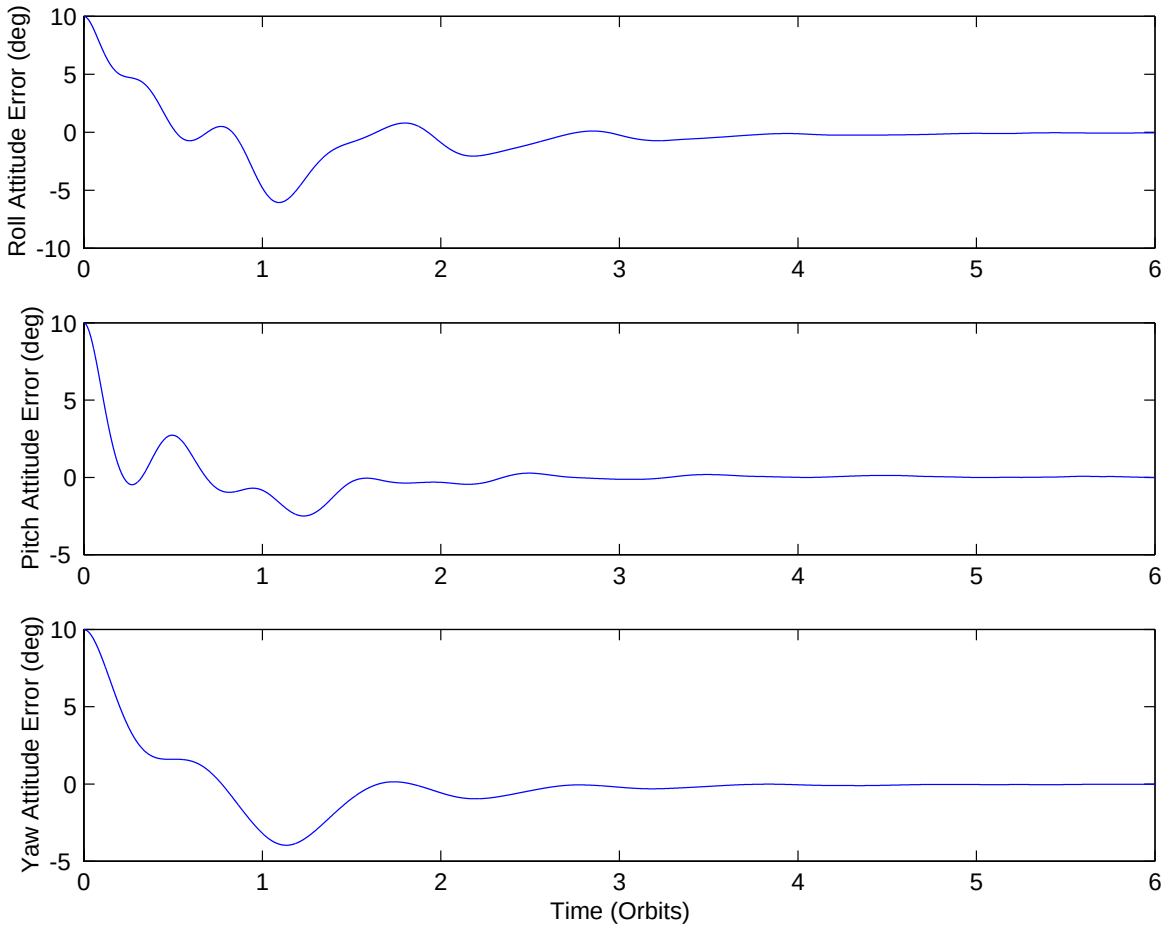

Figure 1.13: Control simulation results with cyclic-disturbance rejection control in the presence of various dynamic modeling uncertainties.

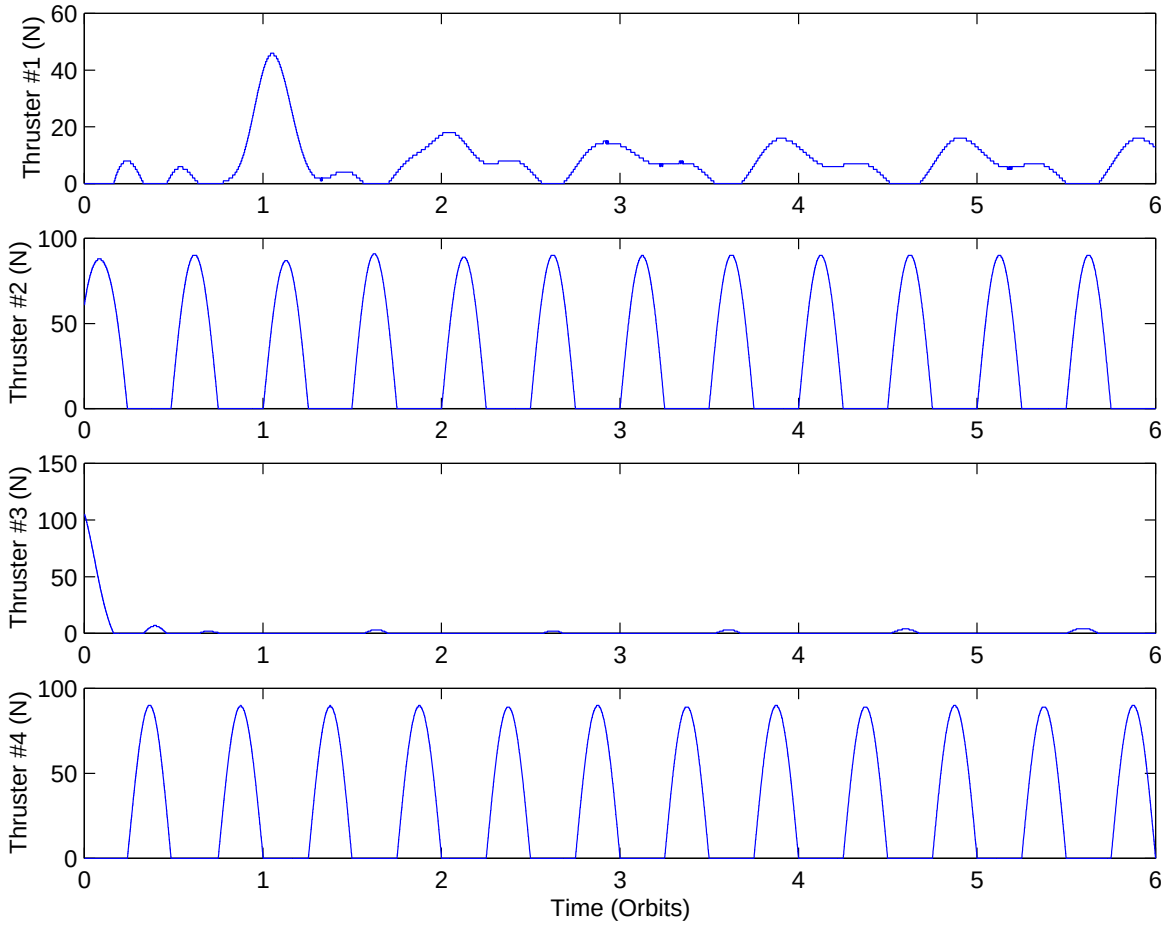

Figure 1.14: Roll/pitch thruster firings for simultaneous eccentricity and roll/pitch control.

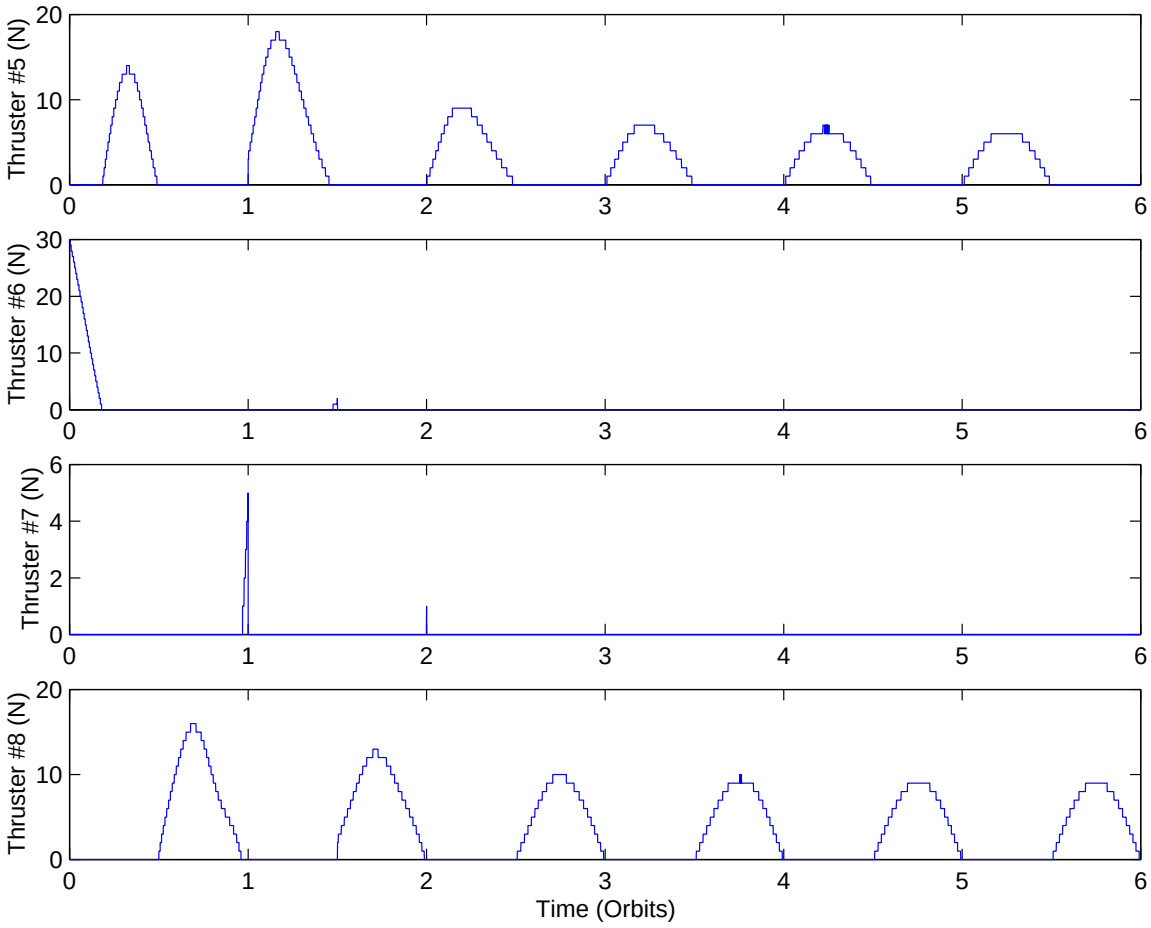

Figure 1.15: Yaw thruster firings for simultaneous inclination and yaw attitude control.

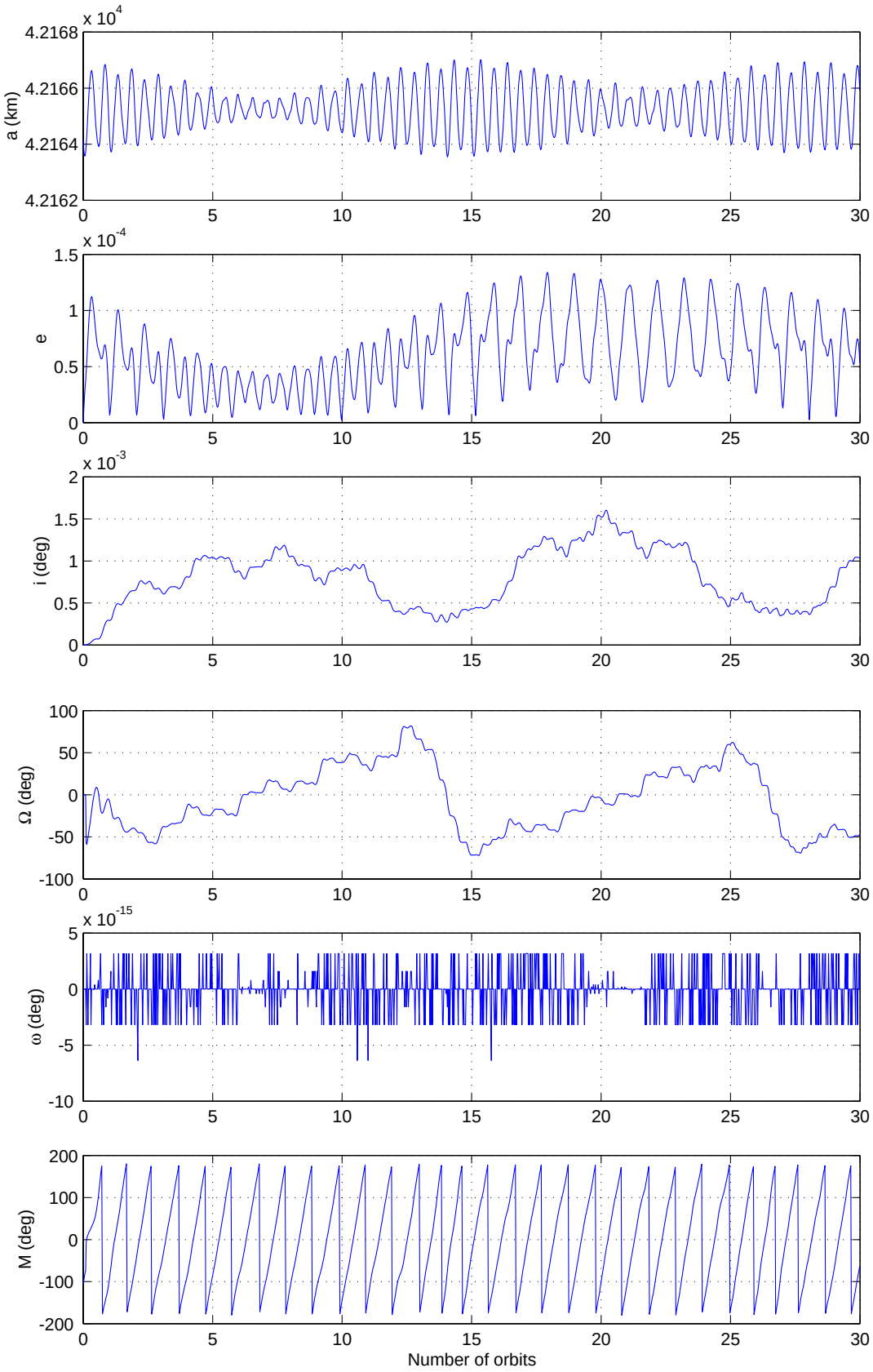

Figure 1.16: Orbit control simulation results with simultaneous orbit and attitude control.

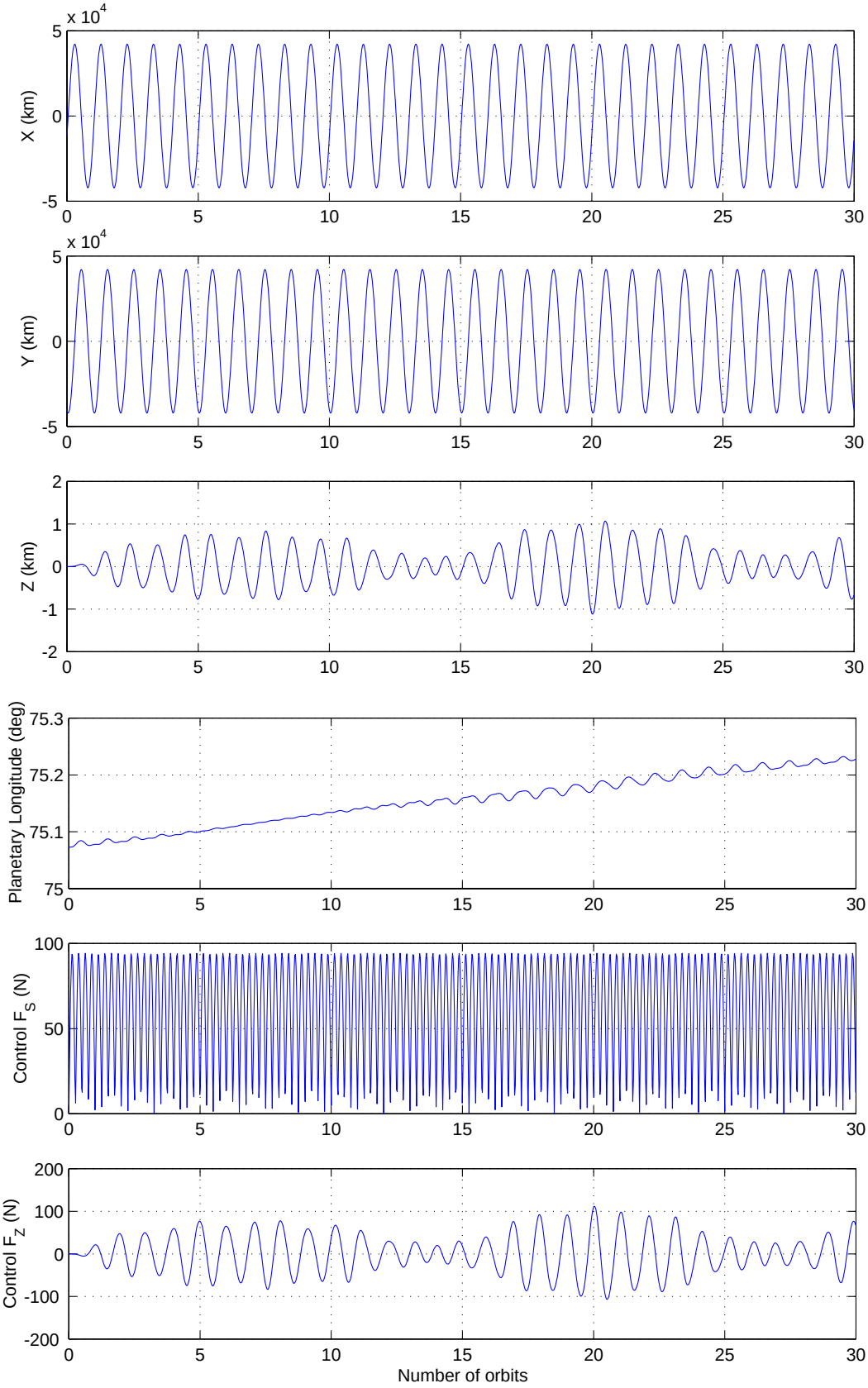

Figure 1.17: Orbit control simulation results with simultaneous orbit and attitude control (continued).

1.6 Summary and Recommendations for Future Research

1.6.1 Summary of Study Results

The area-to-mass ratio, 0.4 m^2/kg, is a key indication of the sensitivity of the Abacus satellite to solar radiation pressure. Left unopposed, solar radiation pressure can cause a cyclic drift in the longitude of the Abacus satellite of 2 deg, east and west. Consequently, in addition to standard north-south and east-west stationkeeping maneuvers, active control of the orbit eccentricity using high-I_{sp} electric thrusters becomes mandatory.

The proposed control system architecture utilizes properly distributed 500 1-N ion thrusters to counter, simultaneously, the cyclic pitch gravity-gradient torque, the secular roll torque caused by cm-cp offset and solar pressure, the cyclic roll/yaw microwave radiation torque, and the solar pressure force of an average value of about 60 N. In contrast to a typical placement of thrusters at the four corners, e.g., employed for the 1979 SSPS reference system, the proposed placement shown in Figure 1.12 minimizes roll/pitch thruster couplings as well as the excitation of platform out-of-plane bending modes. A control-structure interaction problem of the Abacus platform with the lowest structural mode frequency of 0.002 Hz is avoided simply by designing an attitude control system with very low bandwidth (< orbit frequency). However, the proposed low-bandwidth control system utilizes a concept of cyclic-disturbance accommodating control to provide ±5 arcmin pointing of the Abacus platform in the presence of large external disturbances and dynamic modeling uncertainties.

Approximately 85,000 kg of propellant per year is required for simultaneous orbit, attitude, and structural control using 500 1-N electric propulsion thrusters with I_{sp} = 5,000 sec; yearly propellant consumption is reduced to 21,000 kg if the thrusters have an I_{sp} of 20,000 sec. As I_{sp} is increased, the propellant mass decreases but the electric power requirement increases; consequently, the mass of solar arrays and power processing units increases. The total dry mass (power processing units, thrusters, tanks, feed systems, etc.) of electric propulsion systems of the Abacus satellite is estimated as 75,000 kg, based on 500 1-N thrusters and a mass/power ratio of 5 kg/kW. The peak power requirement is estimated as 6 MW based on the peak thrust requirement of 200 N and a power/thrust ratio of 30 kW/N.

1.6.2 Recommendations for Future Research

The baseline control system architecture developed for the Abacus satellite requires a minimum of 500 ion engines of 1-N thrust level. The capability of present electric thrusters are orders of magnitude below that required for the Abacus satellite. If the xenon fueled, 1-kW level, off-the-shelf ion engines available today, are to be employed, the number of thrusters would be increased to 15,000. The actual total number of ion engines will further increase significantly when we consider the ion engine's lifetime, relia-

Table 1.7: Technology advancement needs for the Abacus SSPS

	Current	Enabling
Electric Thrusters	3 kW, 100 mN	30 kW, 1 N
	$I_{sp} = 3000$ sec	$I_{sp} > 5000$ sec
	(5,000–10,000 thrusters)	(500–1,000 thrusters)
CMGs	20 N-m-s/kg	2,000 N-m-s/kg
	5,000 N-m-s/unit	500,000 N-m-s/unit
	(500,000 CMGs)	(5,000 CMGs)
Space-Assembled		66,000 N-m-s/kg
Momentum Wheels		4×10^8 N-m-s/unit
(300-m diameter)		(5–10 MWs)

bility, duty cycle, redundancy, etc. Consequently, a 30-kW, 1-N level electric propulsion thruster with a specific impulse greater than 5,000 sec needs to be developed for the Abacus satellite if excessively large number of thrusters are to be avoided.

Several high-power electric propulsion systems are currently under development. For example, the NASA T-220 10-kW Hall thruster recently completed a 1,000-hr life test. This high-power (over 5 kW) Hall thruster provides 500 mN of thrust at a specific impulse of 2,450 sec and 59% total efficiency. Dual-mode Hall thrusters, which can operate in either high-thrust mode or high-I_{sp} mode for efficient propellant usage, are also being developed.

The exhaust gas from an electric propulsion system forms an essentially neutral plasma beam extending for large distances in space. Because little is known yet about the long-term effect of an extensive plasma on geosynchronous satellites with regard to communications, solar cell degradation, contamination, etc, the use of lightweight, space-assembled large-diameter momentum wheels may also be considered as an option for the Abacus satellite; therefore, these devices warrant further study. The electric thrusters, CMGs, and momentum wheels are compared in Table 1.7 in terms of their technology advancement needs. It is emphasized that both electrical propulsion and momentum wheel technologies require significant advancement to support the development of large SSPS.

Despite the huge size and low structural frequencies of the Abacus satellite, the control-structure interaction problem appears to be a tractable one because the tight pointing control requirement can be met even with a control bandwidth that is much lower than the lowest structural frequency. However, further detailed study needs to be performed for achieving the required 5-arcmin microwave beam pointing accuracy in the presence of transmitter/reflector-coupled structural dynamics, Abacus platform thermal distortion and vibrations, hardware constraints, and other short-term impulsive disturbances.

Although the rotating reflector concept of the Abacus satellite eliminates massive rotary joint and slip rings of the 1979 SSPS reference concept, the transmitter fixed to the Abacus platform results in unnecessarily tight pointing requirements imposed on the platform. Further system-level tradeoffs will be required for the microwave-transmitting antenna design, such as whether or not to gimbal it with respect to the platform, use mechanical or electronic beam steering, and so forth.

The following research topics of practical importance in the areas of dynamics and control of large flexible space platforms also need further detailed investigation to support the development of large SSPS.

- Thermal distortion and vibration due to solar heating
- Structural distortion due to gravity-gradient loading
- Autonomous stationkeeping maneuvers
- Simultaneous eccentricity and longitude control
- Attitude control during the solar eclipses
- Orbit and attitude control during assembly
- Attitude and orbit determination problem
- Reflector tracking and pointing control problem
- Microwave beam pointing analysis and simulation
- Space-assembled, large-diameter momentum wheels
- Electric propulsion systems for both orbit transfer and on-orbit control
- Backup chemical propulsion systems for attitude and orbit control

Chapter 2

Mathematical Models of Large Sun-Pointing Spacecraft

2.1 Introduction to Orbit Dynamics

This section provides a summary of the basic definitions and fundamentals in orbital mechanics. It also provides the necessary background material for a non-Keplerian orbit model with various orbit perturbation effects to be discussed later in this chapter. Further detailed discussions of orbital mechanics can be found in Ref. [16].

2.1.1 Two-Body System

Consider two particles P_1 and P_2, of masses m_1 and m_2, whose position vectors from a point fixed in an inertial reference frame are given by $\vec{R}_1$ and $\vec{R}_2$, respectively, as shown in Figure 2.1. Applying Newton's second law and his law of gravity to each particle, we write the equations of motion as

$$m_1 \ddot{\vec{R}}_1 = +\frac{G m_1 m_2}{r^3} \vec{r} \tag{1}$$

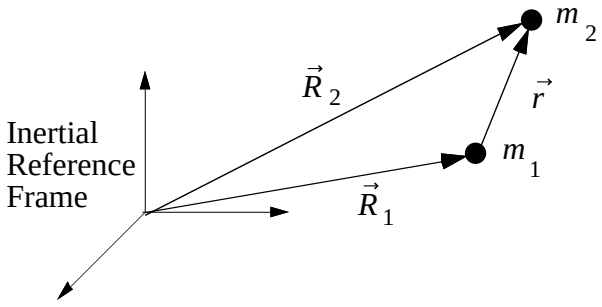

Figure 2.1: Two-body problem.

$$m_2\ddot{\vec{R}}_2 = -\frac{Gm_1m_2}{r^3}\vec{r} \tag{2}$$

where $\vec{r} = \vec{R}_2 - \vec{R}_1$ is the position vector from P_1 to P_2, $r = |\vec{r}|$, $\ddot{\vec{R}}_i = d^2\vec{R}_i/dt^2$ is the inertial acceleration of P_i, and $G = 6.6695\times10^{-11}\text{N}\cdot\text{m}^2/\text{kg}^2$ is the universal gravitational constant.

Eliminating m_1 from Eq. (1), and m_2 from Eq. (2), and subtracting the first result from the second, we obtain

$$\ddot{\vec{r}} + \frac{\mu}{r^3}\vec{r} = 0 \tag{3}$$

where $\ddot{\vec{r}} = d^2\vec{r}/dt^2$ is the inertial acceleration of P_2 with respect to P_1, $r = |\vec{r}|$, and $\mu = G(m_1 + m_2)$ is called the *gravitational parameter* of the two-body system under consideration. Equation (3) describes the motion of P_2 relative to P_1 in an inertial reference frame and it is the fundamental equation in the two-body problem.

In most practical cases of interest in orbital mechanics, the mass of the primary body is much greater than that of the secondary body (i.e., $m_1 \gg m_2$), which results in $\mu \approx Gm_1$. For example, for a sun-planet system, we have $\mu \approx \mu_\odot \equiv GM_\odot$, where $\mu_\odot$ denotes the gravitational parameter of the sun and $M_\odot$ denotes the mass of the sun. Likewise, for an earth-satellite system, we have $\mu \approx \mu_\oplus \equiv GM_\oplus$, where $\mu_\oplus$ denotes the gravitational parameter of the earth and $M_\oplus$ denotes the mass of the earth. It is worth emphasizing that, in the two-body problem, the primary body is *not* inertially fixed. The two-body problem must be distinguished from a so-called *restricted* two-body problem in which the primary body of mass m_1 is assumed to be inertially fixed. Such a restricted two-body problem is often described by *central force motion* of a particle of mass m_2 around the inertially-fixed primary body of mass m_1.

Energy Equation

The energy equation of the two-body system is given by

$$\frac{v^2}{2} - \frac{\mu}{r} = \mathcal{E} \tag{4}$$

where $v \equiv |\vec{v}| = |\dot{\vec{r}}|$, the constant $\mathcal{E}$ is called the *total mechanical energy per unit mass* or the *specific mechanical energy*, $v^2/2$ is the *kinetic energy per unit mass*, and $-\mu/r$ is a *potential energy per unit mass*. This equation represents the law of conservation of energy for the two-body system.

Angular Momentum Equation

Defining the *angular momentum per unit mass* or the *specific angular momentum* as

$$\vec{h} = \vec{r}\times\dot{\vec{r}} \equiv \vec{r}\times\vec{v} \tag{5}$$

we obtain

$$\frac{d\vec{h}}{dt} = 0 \quad \text{or} \quad \vec{h} = \text{constant vector} \tag{6}$$

Thus we have the law of conservation of angular momentum for the two-body system. Since $\vec{h}$ is the vector cross product of $\vec{r}$ and $\vec{v}$, it is always perpendicular to the plane containing $\vec{r}$ and $\vec{v}$. Furthermore, since $\vec{h}$ is a constant vector, $\vec{r}$ and $\vec{v}$ always remain in the same plane, called an *orbital plane*. Therefore, we conclude that the orbital plane is fixed in an inertial reference frame, and the angular momentum vector $\vec{h}$ is perpendicular to the orbital plane.

Eccentricity Vector

Taking the post-cross product of Eq. (3) with $\vec{h}$, finding an expression for a vector whose inertial derivative is equal to the preceding cross product, and then integrating, we obtain

$$\dot{\vec{r}} \times \vec{h} - \frac{\mu}{r}\vec{r} = \text{constant vector} = \mu\vec{e} \tag{7}$$

where a constant vector $\vec{e}$ is called the *eccentricity vector*. Note that the constant vector $\mu\vec{e}$ can also be written as

$$\begin{aligned} \mu\vec{e} = \vec{v} \times \vec{h} - \frac{\mu}{r}\vec{r} &= \vec{v} \times (\vec{r} \times \vec{v}) - \frac{\mu}{r}\vec{r} \\ &= (v^2 - \frac{\mu}{r})\vec{r} - (\vec{r} \cdot \vec{v})\vec{v} \end{aligned}$$

Taking the dot product of Eq. (7) with $\vec{r}$, we find

$$h^2 - \mu r = \mu r e \cos\theta \tag{8}$$

where $h \equiv |\vec{h}|$, $e \equiv |\vec{e}|$, and θ is the angle between $\vec{r}$ and $\vec{e}$. The angle θ is called the *true anomaly* and e is called the *eccentricity* of the orbit.

Kepler's First Law

Equation (8) can be further transformed into the *orbit equation* of the form:

$$r = \frac{h^2/\mu}{1 + e\cos\theta} \tag{9}$$

which can be rewritten as

$$r = \frac{p}{1 + e\cos\theta} \tag{10}$$

where p, called the *parameter*, is defined as

$$p = \frac{h^2}{\mu} \tag{11}$$

Equation (10) is the equation of a *conic section*, written in terms of polar coordinates r and θ with the origin located at a focus, with θ measured from the point on the conic nearest the focus. Kepler's first law states that the orbit of each planet around the sun is an ellipse, with the sun at one focus. Since an ellipse is one type of conic section, Kepler's first law follows from this equation. The size and shape of the orbit depends on the parameter p and the eccentricity e, respectively.

Kepler's Second and Third Laws

The orbital area, ΔA, swept out by the radius vector $\vec{r}$ as it moves through a small angle $\Delta\theta$ in a time interval Δt, is given as

$$\Delta A = \frac{1}{2} r(r\Delta\theta)$$

Then the *areal velocity* of the orbit, denoted by dA/dt, can be shown to be constant, as follows:

$$\frac{dA}{dt} = \lim_{\Delta t \to 0} \frac{\Delta A}{\Delta t} = \lim_{\Delta t \to 0} \frac{1}{2} r^2 \frac{\Delta\theta}{\Delta t} = \frac{1}{2} r^2 \dot{\theta} = \frac{1}{2} h = \text{constant} \tag{12}$$

which is a statement of Kepler's second law: the radius vector from the sun to a planet sweeps out equal areas in equal time intervals.

The period of an elliptical can be found by dividing the total orbital area by the areal velocity, as follows:

$$P = \frac{A}{dA/dt} = \frac{\pi ab}{h/2} = \frac{\pi a^2 \sqrt{1-e^2}}{\sqrt{\mu a(1-e^2)}/2} = 2\pi \sqrt{\frac{a^3}{\mu}} \tag{13}$$

where a is the semimajor axis and b is the semiminor axis of an ellipse. This can be rewritten as

$$P^2 = \frac{4\pi^2}{\mu} a^3$$

which is, in fact, a statement of Kepler's third law: the square of the orbital period of a planet is proportional to the cube of the semimajor axis of the ellipse. Note that the ratio P^2/a^3 is not constant for all planets because $\mu = G(M_\odot + m_2)$, where $M_\odot$ is the mass of the sun and m_2 is the mass of the planet. Therefore, the ratio differs slightly for each planet.

Kepler's Time Equation

Now we introduce a geometrical parameter known as the *eccentric anomaly* to find the position in an orbit as a function of time or vice versa.

Consider an auxiliary circle, which was first introduced by Kepler, as shown in Figure 2.2. From this figure, we have

$$a\cos E + r\cos(\pi - \theta) = ae \tag{14}$$

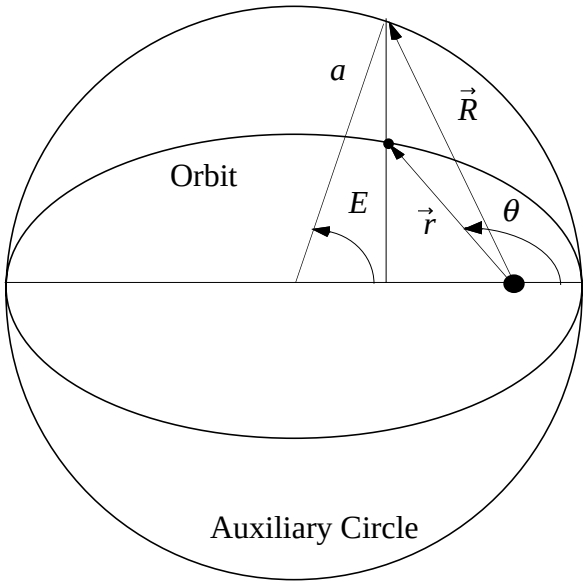

Figure 2.2: The eccentric anomaly E of an elliptic orbit.

where E is the *eccentric anomaly* and θ is the *true anomaly*. Using the orbit equation

$$r = \frac{p}{1 + e\cos\theta} = \frac{a(1-e^2)}{1 + e\cos\theta} \tag{15}$$

we rewrite Eq. (14) as

$$\cos E = \frac{e + \cos\theta}{1 + e\cos\theta} \tag{16}$$

Using the fact that all lines parallel to the minor axis of an ellipse have a foreshortening factor of b/a with respect to a circle with a radius of a, we obtain

$$r\sin\theta = \frac{b}{a}(a\sin E) = a\sqrt{1-e^2}\sin E \tag{17}$$

Combining this with the orbit equation, we obtain

$$\sin E = \frac{\sqrt{1-e^2}\sin\theta}{1 + e\cos\theta} \tag{18}$$

Furthermore, we have

$$\tan\frac{E}{2} = \frac{\sin E}{1 + \cos E} = \sqrt{\frac{1-e}{1+e}}\tan\frac{\theta}{2} \tag{19}$$

from which E or θ can be determined without quadrant ambiguity.

Equation (14) can be rewritten as

$$r\cos\theta = a(\cos E - e) \tag{20}$$

Thus, squaring Eqs. (17) and (20) and adding them, we obtain

$$r = a(1 - e\cos E) \tag{21}$$

which is the orbit equation in terms of the eccentric anomaly E and its geometrical constants a and e.

The area swept out by the position vector $\vec{r}$ is

$$(t - t_p)\dot{A} = (t - t_p)\frac{ab}{2}\sqrt{\frac{\mu}{a^3}} \tag{22}$$

where t_p is the perigee passage time, $(t - t_p)$ is the elapsed time since perigee passage, and $\dot{A}$ is the constant areal velocity given by Kepler's third law:

$$\dot{A} = \frac{\pi ab}{P} = \frac{\pi ab}{2\pi\sqrt{a^3/\mu}} = \frac{ab}{2}\sqrt{\frac{\mu}{a^3}} \tag{23}$$

This area of the ellipse is the same as the area of the auxiliary circle swept out by the vector $\vec{R}$, multiplied by the factor b/a. Thus we have

$$\begin{aligned}\frac{ab}{2}\sqrt{\frac{\mu}{a^3}}(t - t_p) &= \frac{b}{a}(\frac{1}{2}a^2E - \frac{ae}{2}a\sin E) \\ &= \frac{ab}{2}(E - e\sin E)\end{aligned} \tag{24}$$

which becomes

$$\sqrt{\frac{\mu}{a^3}}\,(t - t_p) = E - e\sin E \tag{25}$$

where E is in units of radians.

Defining the *mean anomaly* M and the orbital *mean motion* n, as follows:

$$M = n(t - t_p) \tag{26}$$

$$n = \sqrt{\frac{\mu}{a^3}} \tag{27}$$

we obtain

$$M = E - e\sin E \tag{28}$$

which is known as *Kepler's time equation* for relating time to position in orbit.

The time required to travel between any two points in an elliptical orbit can be simply computed by first determining the eccentric anomaly E corresponding to a given true anomaly θ and then by using Kepler's time equation.

Kepler's time equation (28) does not provide time values, $(t - t_p)$, greater than one-half of the orbit period, but it gives the elapsed time since perigee passage in the shortest direction. Thus, for $\theta > \pi$, the result obtained from Eq. (28) must be subtracted from the orbit period to obtain the correct time since perigee passage.

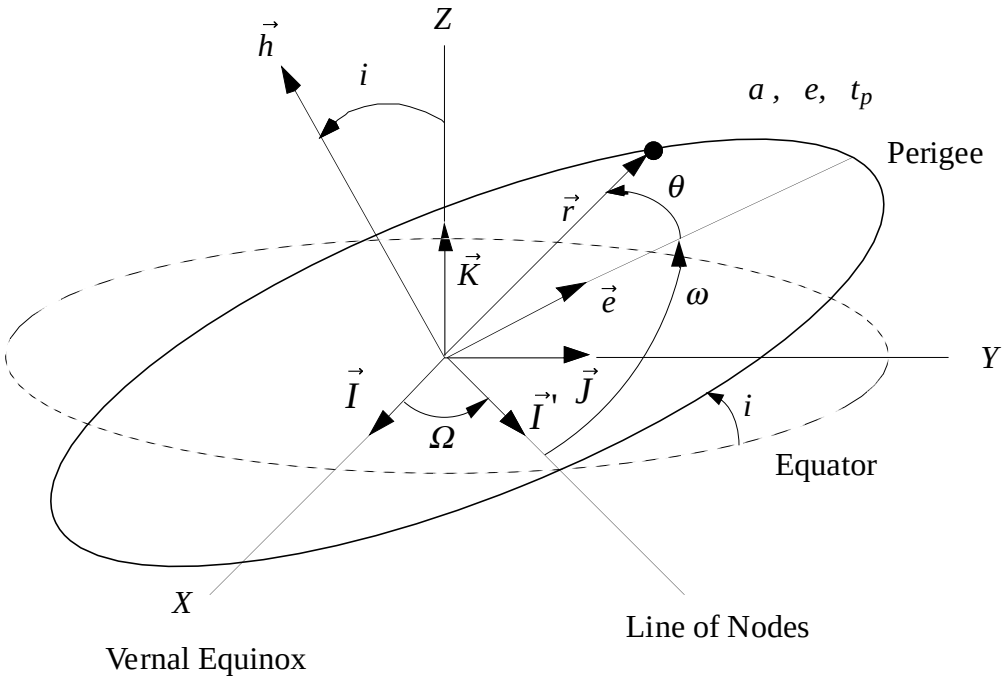

Figure 2.3: Orbit orientation with respect to the geocentric-equatorial reference frame, also called the Earth-Centered Inertial (ECI) reference system. A near circular orbit is shown in this figure.

2.1.2 Orbital Elements

In general, the two-body system characterized by Eq. (3) has three degrees of freedom, and the orbit is uniquely determined if six initial conditions are specified, three of which are associated with $\vec{r}$ at some initial time, and three of which are associated with $\vec{v} \equiv \dot{\vec{r}}$. In orbital mechanics, the constants of integration or integrals of the motion are also referred to as *orbital elements* and such initial conditions can be considered as six possible orbital elements.

To describe a satellite orbit about the earth, we often employ six other scalars, called the *six orbital elements*. Three of these scalars specify the orientation of the orbit plane with respect to the *geocentric-equatorial* reference frame, often called the Earth-Centered Inertial (ECI) reference system, which has its origin at the center of the earth. The fundamental plane in the ECI system, which is the earth's equatorial plane, has an inclination of approximately 23.45 deg with respect to the plane of the earth's heliocentric orbit, known as the ecliptic plane. A set of orthogonal unit vectors $\{\vec{I}, \vec{J}, \vec{K}\}$ is selected as basis vectors of the ECI reference frame with (X, Y, Z) coordinates, as shown in Figure 2.3.

Note that the ECI reference frame is not fixed to the earth and is not rotating with it; rather the earth rotates about it. The (X, Y) plane of the geocentric-equatorial reference

frame is the earth's equatorial plane, simply called the *equator*. The Z-axis is along the earth's polar axis of rotation. The X-axis is pointing toward the *vernal equinox*, the point in the sky where the sun crosses the equator from south to north on the first day of spring. The vernal equinox direction is often denoted by the symbol Υ.

The six orbital elements consist of five independent quantities, which are sufficient to completely describe the size, shape, and orientation of an orbit, and one quantity required to pinpoint the position of a satellite along the orbit at any particular time. The six classical orbital elements are:

$$\begin{aligned} a &= \text{ the semimajor axis} \\ e &= \text{ the eccentricity} \\ i &= \text{the inclination of the orbit plane} \\ \Omega &= \text{the right ascension of the ascending node} \\ \omega &= \text{the argument of the perigee} \\ M &= \text{the mean anomaly} \end{aligned}$$

A traditional set of the six classical orbital elements includes the perigee passage time, t_p, instead of the mean anomaly, M.

The elements a and e determine the size and shape of the elliptic orbit, respectively, and t_p or M relates position in orbit to time. The angles Ω and i specify the orientation of the orbit plane with respect to the geocentric-equatorial reference frame. The angle ω specifies the orientation of the orbit in its plane. Orbits with $i < 90$ deg are called *prograde orbits*, while orbits with $i > 90$ deg are called *retrograde orbits*. The term *prograde* means the easterly direction in which the sun, earth, and most of the planets and their moons rotate on their axes. The term *retrograde* means westerly direction, which is simply the opposite of prograde. An orbit whose inclination is near 90 deg is called a *polar orbit*. An *equatorial orbit* has zero inclination.

The line of nodes does not exist for equatorial orbits with zero inclination and also the line of apsides does not exist for circular orbits with zero eccentricity. Because a set of orbit equations with such classical orbital elements has a singularity problem when $e = 0$ or $\sin i = 0$, we often employ the so-called *equinoctial* orbital elements defined in terms of the classical orbital elements, as follows [16]:

$$\begin{aligned} a &= a \\ P_1 &= e \sin(\Omega + \omega) \\ P_2 &= e \cos(\Omega + \omega) \\ Q_1 &= \tan(i/2) \sin \Omega \\ Q_2 &= \tan(i/2) \cos \Omega \\ \ell &= \Omega + \omega + M \end{aligned}$$

where ℓ is called the mean longitude.

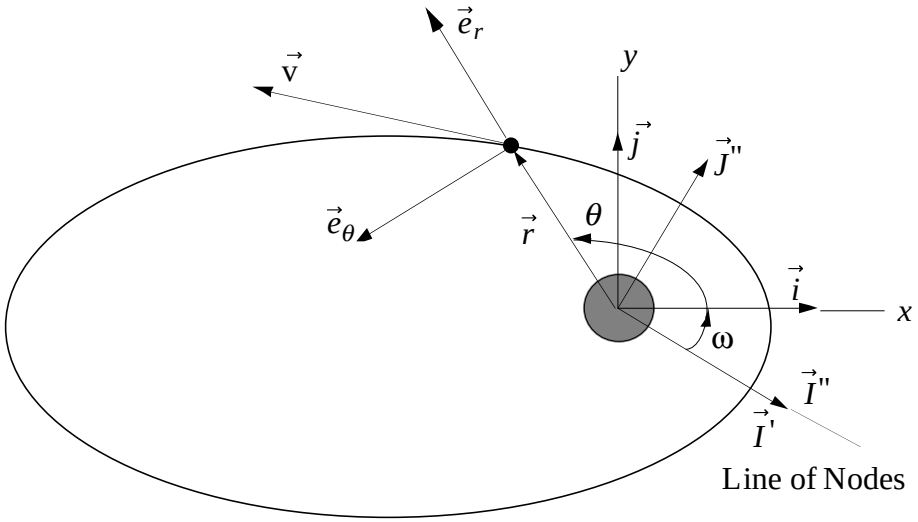

Figure 2.4: Perifocal reference frame.

2.1.3 Orbital Position and Velocity

Given the geocentric-equatorial (X, Y, Z) reference frame with basis vectors $\{\vec{I}, \vec{J}, \vec{K}\}$ and a perifocal (x, y, z) reference frame with basis vectors $\{\vec{i}, \vec{j}, \vec{k}\}$, the position vector is represented as

$$\vec{r} = X\vec{I} + Y\vec{J} + Z\vec{K} = x\vec{i} + y\vec{j} + z\vec{k} \tag{29}$$

The position vector $\vec{r}$ can also be expressed as

$$\vec{r} = X'\vec{I}' + Y'\vec{J}' + Z'\vec{K}' = X''\vec{I}'' + Y''\vec{J}'' + Z''\vec{K}'' \tag{30}$$

where (X', Y', Z') and (X'', Y'', Z'') are the components of the position vector $\vec{r}$ in two intermediate reference frames with basis vectors $\{\vec{I}', \vec{J}', \vec{K}'\}$ and $\{\vec{I}'', \vec{J}'', \vec{K}''\}$, respectively.

The perifocal reference frame is then related to the geocentric-equatorial reference frame through three successive rotations as follows:

$$\begin{bmatrix} \vec{I}' \\ \vec{J}' \\ \vec{K}' \end{bmatrix} = \begin{bmatrix} \cos\Omega & \sin\Omega & 0 \\ -\sin\Omega & \cos\Omega & 0 \\ 0 & 0 & 1 \end{bmatrix} \begin{bmatrix} \vec{I} \\ \vec{J} \\ \vec{K} \end{bmatrix} \tag{31a}$$

$$\begin{bmatrix} \vec{I}'' \\ \vec{J}'' \\ \vec{K}'' \end{bmatrix} = \begin{bmatrix} 1 & 0 & 0 \\ 0 & \cos i & \sin i \\ 0 & -\sin i & \cos i \end{bmatrix} \begin{bmatrix} \vec{I}' \\ \vec{J}' \\ \vec{K}' \end{bmatrix} \tag{31b}$$

$$\begin{bmatrix} \vec{i} \\ \vec{j} \\ \vec{k} \end{bmatrix} = \begin{bmatrix} \cos\omega & \sin\omega & 0 \\ -\sin\omega & \cos\omega & 0 \\ 0 & 0 & 1 \end{bmatrix} \begin{bmatrix} \vec{I}'' \\ \vec{J}'' \\ \vec{K}'' \end{bmatrix} \tag{31c}$$

The orbital elements Ω, i, and ω are in fact the Euler angles of the so-called $\mathbf{C}_3(\omega) \leftarrow \mathbf{C}_1(i) \leftarrow \mathbf{C}_3(\Omega)$ rotational sequence.

By combining the sequence of rotations above, we obtain

$$\begin{bmatrix} \vec{i} \\ \vec{j} \\ \vec{k} \end{bmatrix} = \begin{bmatrix} \cos\omega & \sin\omega & 0 \\ -\sin\omega & \cos\omega & 0 \\ 0 & 0 & 1 \end{bmatrix} \begin{bmatrix} 1 & 0 & 0 \\ 0 & \cos i & \sin i \\ 0 & -\sin i & \cos i \end{bmatrix} \begin{bmatrix} \cos\Omega & \sin\Omega & 0 \\ -\sin\Omega & \cos\Omega & 0 \\ 0 & 0 & 1 \end{bmatrix} \begin{bmatrix} \vec{I} \\ \vec{J} \\ \vec{K} \end{bmatrix}$$

which becomes

$$\begin{bmatrix} \vec{i} \\ \vec{j} \\ \vec{k} \end{bmatrix} = \begin{bmatrix} C_{11} & C_{12} & C_{13} \\ C_{21} & C_{22} & C_{23} \\ C_{31} & C_{32} & C_{33} \end{bmatrix} \begin{bmatrix} \vec{I} \\ \vec{J} \\ \vec{K} \end{bmatrix} \tag{32}$$

where

$$\begin{aligned} C_{11} &= \cos\Omega\cos\omega - \sin\Omega\sin\omega\cos i \\ C_{12} &= \sin\Omega\cos\omega + \cos\Omega\sin\omega\cos i \\ C_{13} &= \sin\omega\sin i \\ C_{21} &= -\cos\Omega\sin\omega - \sin\Omega\cos\omega\cos i \\ C_{22} &= -\sin\Omega\sin\omega + \cos\Omega\cos\omega\cos i \\ C_{23} &= \cos\omega\sin i \\ C_{31} &= \sin\Omega\sin i \\ C_{32} &= -\cos\Omega\sin i \\ C_{33} &= \cos i \end{aligned}$$

The matrix $\mathbf{C} = [C_{ij}]$ is called the *direction cosine matrix* which describes the orientation of the perifocal reference frame with respect to the geocentric-equatorial reference frame.

The components (x, y, z) of the position vector in the perifocal reference frame are then related to the components (X, Y, Z) of the position vector in the geocentric-equatorial reference frame via the same direction cosine matrix $\mathbf{C}$ as:

$$\begin{bmatrix} x \\ y \\ z \end{bmatrix} = \begin{bmatrix} C_{11} & C_{12} & C_{13} \\ C_{21} & C_{22} & C_{23} \\ C_{31} & C_{32} & C_{33} \end{bmatrix} \begin{bmatrix} X \\ Y \\ Z \end{bmatrix} \tag{33}$$

Since the direction cosine matrix $\mathbf{C}$ is an orthonormal matrix, i.e., $\mathbf{C}^{-1} = \mathbf{C}^T$, we also have

$$\begin{bmatrix} X \\ Y \\ Z \end{bmatrix} = \begin{bmatrix} C_{11} & C_{21} & C_{31} \\ C_{12} & C_{22} & C_{32} \\ C_{13} & C_{23} & C_{33} \end{bmatrix} \begin{bmatrix} x \\ y \\ z \end{bmatrix} \tag{34}$$

The components of the velocity vector represented as

$$\vec{v} = \dot{X}\vec{I} + \dot{Y}\vec{J} + \dot{Z}\vec{K} = \dot{x}\vec{i} + \dot{y}\vec{j} + \dot{z}\vec{k} \tag{35}$$

are also related as

$$\begin{bmatrix} \dot{x} \\ \dot{y} \\ \dot{z} \end{bmatrix} = \begin{bmatrix} C_{11} & C_{12} & C_{13} \\ C_{21} & C_{22} & C_{23} \\ C_{31} & C_{32} & C_{33} \end{bmatrix} \begin{bmatrix} \dot{X} \\ \dot{Y} \\ \dot{Z} \end{bmatrix} \tag{36}$$

or

$$\begin{bmatrix} \dot{X} \\ \dot{Y} \\ \dot{Z} \end{bmatrix} = \begin{bmatrix} C_{11} & C_{21} & C_{31} \\ C_{12} & C_{22} & C_{32} \\ C_{13} & C_{23} & C_{33} \end{bmatrix} \begin{bmatrix} \dot{x} \\ \dot{y} \\ \dot{z} \end{bmatrix} \tag{37}$$

Using the following relationships

$$\begin{bmatrix} x \\ y \\ z \end{bmatrix} = \begin{bmatrix} r\cos\theta \\ r\sin\theta \\ 0 \end{bmatrix} \quad \text{and} \quad \begin{bmatrix} \dot{x} \\ \dot{y} \\ \dot{z} \end{bmatrix} = \begin{bmatrix} -\sqrt{\mu/p}\sin\theta \\ \sqrt{\mu/p}(e+\cos\theta) \\ 0 \end{bmatrix} \tag{38}$$

where $p = a(1-e^2)$ is the parameter, we also obtain

$$\begin{bmatrix} X \\ Y \\ Z \end{bmatrix} = \begin{bmatrix} C_{11} & C_{21} & C_{31} \\ C_{12} & C_{22} & C_{32} \\ C_{13} & C_{23} & C_{33} \end{bmatrix} \begin{bmatrix} r\cos\theta \\ r\sin\theta \\ 0 \end{bmatrix} \tag{39}$$

$$\begin{bmatrix} \dot{X} \\ \dot{Y} \\ \dot{Z} \end{bmatrix} = \begin{bmatrix} C_{11} & C_{21} & C_{31} \\ C_{12} & C_{22} & C_{32} \\ C_{13} & C_{23} & C_{33} \end{bmatrix} \begin{bmatrix} -\sqrt{\mu/p}\sin\theta \\ \sqrt{\mu/p}(e+\cos\theta) \\ 0 \end{bmatrix} \tag{40}$$

2.1.4 Geosynchronous Orbits

If the period of a satellite in a circular prograde equatorial orbit is exactly one siderial day (23 h 56 min 4 s), it will appear to hover motionlessly over a point on the equator. Such a satellite, located at 42,164 km ($\approx 6.6R_\oplus$) from the earth center (or at an altitude of 35,786 km), is called a *geostationary* satellite. A satellite with the orbital period of one siderial day but with a non-zero inclination is called a *geosynchronous* satellite. Its ground track is often characterized by a "figure-eight" curve. Note that regardless of the satellite's orbital inclination, geosynchronous satellites still take 23 hr 56 min 4 s to make one complete revolution around the earth.

2.2 Orbital Perturbations

Thus far in this chapter, we have considered two bodies whose relative motion is described by an ideal or Keplerian orbit in which the plane of the orbit is fixed in inertial space. The Keplerian orbit is a consequence of the assumptions that the primary body has a spherically symmetric mass distribution, the second body is a particle, and the *only* forces exerted on the two bodies are those of mutual gravitational attraction. In

general, however, the mass of the primary body is distributed *aspherically*; the two bodies are subject to the gravitational attraction of other bodies, and to other perturbational forces. As a result, the orbit of the two bodies is non-Keplerian, and the plane of the orbit does not remain fixed in inertial space. The small deviations from the ideal Keplerian orbital motion are often called orbital perturbations. This section presents a non-Keplerian orbit model of satellites influenced by the earth's oblateness and triaxiality, gravitational perturbations from the Sun and Moon, and solar radiation pressure force.

2.2.1 Non-Keplerian Orbit Dynamics

Consider the general equation of motion of a satellite about the earth described by

$$\ddot{\vec{r}} + \frac{\mu}{r^3}\vec{r} = \vec{f} \tag{41}$$

where $\vec{r}$ is the position vector of the satellite from the center of the earth, $\ddot{\vec{r}}$ indicates the second derivative of $\vec{r}$ with respect to time in an inertial reference frame, $\mu \approx \mu_{\oplus}$, and $\vec{f}$, called the *perturbing acceleration*, represents the resultant perturbing force per unit mass acting on the satellite, added to the negative of the resultant perturbing force per unit mass acting on the earth. The position of a satellite acted upon by the perturbing acceleration is often referred to a plane containing $\vec{r}$ and $\dot{\vec{r}}$, called the *osculating orbital* plane.

Taking the dot product of Eq. (41) with $\dot{\vec{r}}$ yields

$$\ddot{\vec{r}} \cdot \dot{\vec{r}} + \frac{\mu}{r^3}\vec{r} \cdot \dot{\vec{r}} = \vec{f} \cdot \dot{\vec{r}} \tag{42}$$

which is rewritten as

$$\frac{d}{dt}\left(\frac{v^2}{2} - \frac{\mu}{r}\right) = \vec{f} \cdot \dot{\vec{r}} \tag{43}$$

Substituting the specific energy $\mathcal{E}$ defined as

$$\mathcal{E} = \frac{v^2}{2} - \frac{\mu}{r} = -\frac{\mu}{2a}$$

into Eq. (43), we obtain

$$\dot{a} = \frac{2a^2}{\mu}\vec{f} \cdot \dot{\vec{r}} \tag{44}$$

Note that $\mathcal{E}$ is not a constant unless $\vec{f} = 0$ or $\vec{f} \cdot \dot{\vec{r}} = 0$.

Taking the cross product of Eq. (41) with $\vec{r}$, we have

$$\vec{r} \times \ddot{\vec{r}} = \vec{r} \times \vec{f} \tag{45}$$

Differentiating the specific angular momentum defined as

$$\vec{h} = \vec{r} \times \dot{\vec{r}} \tag{46}$$

we obtain

$$\dot{\vec{h}} = \vec{r} \times \ddot{\vec{r}} = \vec{r} \times \vec{f} \tag{47}$$

Note that $\vec{h}$ is not a constant vector unless $\vec{f} = 0$ or $\vec{r} \times \vec{f} = 0$.

Taking the post-cross product of Eq. (41) with $\vec{h}$, we have

$$\ddot{\vec{r}} \times \vec{h} + \frac{\mu}{r^3} \vec{r} \times \vec{h} = \vec{f} \times \vec{h} \tag{48}$$

which is rewritten as

$$\frac{d}{dt} \left(\dot{\vec{r}} \times \vec{h} - \frac{\mu}{r} \vec{r} \right) = \dot{\vec{r}} \times \dot{\vec{h}} + \vec{f} \times \vec{h} \tag{49}$$

Substituting the eccentricity vector $\vec{e}$ defined as

$$\mu \vec{e} = \dot{\vec{r}} \times \vec{h} - \frac{\mu}{r} \vec{r} \tag{50}$$

and Eq. (47) into Eq. (49), we obtain

$$\mu \dot{\vec{e}} = \dot{\vec{r}} \times (\vec{r} \times \vec{f}) + \vec{f} \times \vec{h} \tag{51}$$

Here, $\vec{e}$ is not a constant vector unless the right-hand side of Eq. (51) is zero.

Let $\vec{e}_r$, $\vec{e}_\theta$, and $\vec{e}_z$ be unit vectors along the radial vector direction, the transverse orbit direction, and the direction normal to the orbit plane, respectively, such that $\vec{e}_r \times \vec{e}_\theta = \vec{e}_z$. Then the perturbing acceleration $\vec{f}$ and the velocity vector $\vec{v} \equiv \dot{\vec{r}}$ are represented in terms of the unit vectors $\{\vec{e}_r, \vec{e}_\theta, \vec{e}_z\}$, as follows:

$$\vec{f} = f_r \vec{e}_r + f_\theta \vec{e}_\theta + f_z \vec{e}_z \tag{52}$$

$$\vec{v} = v_r \vec{e}_r + v_\theta \vec{e}_\theta + v_z \vec{e}_z \tag{53}$$

We also have

$$v_r \equiv \dot{r} = \sqrt{\frac{\mu}{p}}\, e \sin\theta \tag{54}$$

$$v_\theta \equiv r\dot{\theta} = \sqrt{\frac{\mu}{p}}\, (1 + e\cos\theta) \tag{55}$$

and $v_z = 0$ due to the assumptions of the osculating orbit. Consequently, the term $\vec{f} \cdot \dot{\vec{r}}$ in Eq. (44) becomes

$$\vec{f} \cdot \dot{\vec{r}} = f_r v_r + f_\theta v_\theta \tag{56}$$

and we obtain

$$\dot{a} = \frac{2a^2}{\sqrt{\mu p}} \{ f_r e \sin\theta + f_\theta (1 + e\cos\theta) \} \tag{57}$$

Differentiating the specific angular momentum vector expressed as

$$\vec{h} = \sqrt{\mu p}\,\vec{k} \tag{58}$$

where $\vec{k}$ $(= \vec{e}_z)$ is a unit vector normal to the orbit plane, we obtain

$$\dot{\vec{h}} = \frac{1}{2}\sqrt{\frac{\mu}{p}}\,\dot{p}\vec{k} + \sqrt{\mu p}\,\dot{\vec{k}} \tag{59}$$

Furthermore, we have

$$\begin{aligned}\dot{\vec{k}} &= (\dot{\Omega}\vec{K} + \dot{i}\vec{I}' + \dot{\omega}\vec{k}) \times \vec{k} \\ &= \dot{\Omega}\sin i\vec{I}'' - \dot{i}\vec{J}''\end{aligned} \tag{60}$$

where $\vec{I}''$ is a unit vector toward the ascending node and $\vec{J}''$ is orthogonal to $\vec{I}''$ (see Figure 2.3). Thus, we have

$$\dot{\vec{h}} = \frac{1}{2}\sqrt{\frac{\mu}{p}}\,\dot{p}\vec{k} + \sqrt{\mu p}(\dot{\Omega}\sin i\vec{I}'' - \dot{i}\vec{J}'') \tag{61}$$

The term $\vec{r} \times \vec{f}$ in Eq. (47) is also written as

$$\vec{r} \times \vec{f} = r f_\theta \vec{k} - r f_z \vec{e}_\theta \tag{62}$$

In terms of unit vectors $\vec{I}''$, $\vec{J}''$, and $\vec{k}$, this equation becomes

$$\vec{r} \times \vec{f} = r f_\theta \vec{k} - r f_z[-\sin(\omega+\theta)\vec{I}'' + \cos(\omega+\theta)\vec{J}''] \tag{63}$$

Since $\dot{\vec{h}} = \vec{r} \times \vec{f}$, equating the coefficients of Eqs. (61) and (63) gives

$$\dot{p} = 2\sqrt{\frac{p}{\mu}}\,r f_\theta \tag{64}$$

$$\dot{\Omega}\sin i = \frac{r f_z}{\sqrt{\mu p}}\sin(\omega+\theta) \tag{65}$$

$$\dot{i} = \frac{r f_z}{\sqrt{\mu p}}\cos(\omega+\theta) \tag{66}$$

Differentiating the relation, $p = a(1-e^2)$, gives

$$\dot{e} = \frac{1}{2ea}[\dot{a}(1-e^2) - \dot{p}] \tag{67}$$

Combining this equation with Eqs. (57) and (64) and using the following relationships

$$\begin{aligned} p &= a(1-e^2) \\ r &= a(1-e\cos E)\end{aligned}$$

we obtain

$$\dot{e} = \sqrt{\frac{p}{\mu}}\,[f_r \sin\theta + f_\theta(\cos\theta + \cos E)] \tag{68}$$

Similar to the preceding derivation of $\dot{e}$, the rotation of the major axis can also be obtained as

$$\dot{\omega} + \dot{\Omega}\cos i = \frac{1}{e}\sqrt{\frac{p}{\mu}}\,[-f_r \cos\theta + f_\theta(1 + r/p)\sin\theta] \tag{69}$$

Since the mean anomaly is defined as $M = E - e\sin E$, we obtain

$$\dot{M} = \dot{E} - \dot{e}\sin E - e\dot{E}\cos E \tag{70}$$

and $\dot{E}$ may be found by differentiating $r = a(1 - e\cos E)$, as follows:

$$\dot{E} = \frac{\dot{r} - \dot{a}(1 - e\cos E) + a\dot{e}\cos E}{ae\sin E} \tag{71}$$

where $\dot{r} = \sqrt{\mu/p}\,e\sin\theta$. Combining these relationships and using

$$\cos E = \frac{e + \cos\theta}{1 + e\cos\theta}$$
$$\sin E = \frac{\sqrt{1 - e^2}\sin\theta}{1 + e\cos\theta}$$

we obtain

$$\dot{M} = n - \frac{2rf_r}{na^2} + \frac{1 - e^2}{nae}[f_r\cos\theta - f_\theta(1 + r/p)\sin\theta] \tag{72}$$

In summary, we have the so-called Gauss form of Lagrange's planetary equations as

$$\dot{a} = \frac{2a^2}{\sqrt{\mu p}}[f_r e\sin\theta + f_\theta(1 + e\cos\theta)] \tag{73}$$

$$\dot{e} = \sqrt{\frac{p}{\mu}}\left[f_r\sin\theta + f_\theta\left(\cos\theta + \frac{e + \cos\theta}{1 + e\cos\theta}\right)\right] \tag{74}$$

$$\dot{i} = \frac{rf_z\cos(\omega + \theta)}{\sqrt{\mu p}} \tag{75}$$

$$\dot{\Omega} = \frac{rf_z\sin(\omega + \theta)}{\sqrt{\mu p}\sin i} \tag{76}$$

$$\dot{\omega} = -\frac{f_z r\sin(\omega + \theta)\cos i}{\sqrt{\mu p}\sin i} - \frac{1}{e}\sqrt{\frac{p}{\mu}}\,[f_r\cos\theta - f_\theta(1 + r/p)\sin\theta] \tag{77}$$

$$\dot{M} = n - \frac{2rf_r}{na^2} + \frac{1 - e^2}{nae}[f_r\cos\theta - f_\theta(1 + r/p)\sin\theta] \tag{78}$$

where $p = a(1 - e^2)$, $n = \sqrt{\mu/a^3}$, and $r = p/(1 + e\cos\theta)$.

Because this set of equations has a singularity problem when $e = 0$ and/or $\sin i = 0$, another set of equations that are free of singularities is often considered by employing a set of the so-called equinoctial orbital elements defined in terms of the classical orbital elements, as follows [16]:

$$\begin{aligned} a &= a \\ P_1 &= e\sin(\Omega+\omega) \\ P_2 &= e\cos(\Omega+\omega) \\ Q_1 &= \tan(i/2)\sin\Omega \\ Q_2 &= \tan(i/2)\cos\Omega \\ \ell &= \Omega+\omega+M \end{aligned}$$

where ℓ is called the mean longitude.

Furthermore, using the true longitude and eccentric longitude defined, respectively, as

$$L = \Omega+\omega+\theta \tag{79}$$

$$K = \Omega+\omega+E \tag{80}$$

we rewrite Kepler's orbit equation, $r = a(1-\cos E)$, as

$$r = a(1 - P_1\sin K - P_2\cos K) \tag{81}$$

and Kepler's time equation, $M = E - e\sin E$, as

$$\ell = K + P_1\cos K - P_2\sin K \tag{82}$$

The true longitude, L, can be obtained from the eccentric longitude,K, using the following relationships [16]:

$$\sin L = \frac{a}{r}\left[\left(1-\frac{a}{a+b}P_2^2\right)\sin K + \frac{a}{a+b}P_1P_2\cos K - P_1\right] \tag{83}$$

$$\cos L = \frac{a}{r}\left[\left(1-\frac{a}{a+b}P_1^2\right)\cos K + \frac{a}{a+b}P_1P_2\sin K - P_2\right] \tag{84}$$

where

$$\frac{a}{a+b} = \frac{1}{1+\sqrt{1-e^2}} = \frac{1}{\sqrt{1-P_1^2-P_2^2}}$$

From Battin [16], we have Gauss' variational equations in terms of the equinoctial elements, as

$$\dot{a} = \frac{2a^2}{h}\left[(P_2\sin L - P_1\cos L)f_r + \frac{p}{r}f_\theta\right] \tag{85}$$

$$\dot{P}_1 = \frac{r}{h}\left\{-\frac{p}{r}\cos L\ f_r + \left[P_1 + \left(1+\frac{p}{r}\right)\sin L\right] f_\theta - P_2(Q_1\cos L - Q_2\sin L) f_z\right\} \quad (86)$$

$$\dot{P}_2 = \frac{r}{h}\left\{\frac{p}{r}\sin L\ f_r + \left[P_2 + \left(1+\frac{p}{r}\right)\cos L\right] f_\theta + P_1(Q_1\cos L - Q_2\sin L) f_z\right\} \quad (87)$$

$$\dot{Q}_1 = \frac{r}{2h}(1+Q_1^2+Q_2^2)\sin L\ f_z \quad (88)$$

$$\dot{Q}_2 = \frac{r}{2h}(1+Q_1^2+Q_2^2)\cos L\ f_z \quad (89)$$

$$\dot{\ell} = n - \frac{r}{h}\left\{\left[\frac{a}{a+b}\left(\frac{p}{r}\right)(P_1\sin L + P_2\cos L) + \frac{2b}{a}\right] f_r \quad (90)$$

$$+ \frac{a}{a+b}\left(1+\frac{p}{r}\right)(P_1\cos L - P_2\sin L) f_\theta + (Q_1\cos L - Q_2\sin L) f_z\right\} \quad (91)$$

where

$$b = a\sqrt{1-P_1^2-P_2^2}$$
$$h = nab$$
$$\frac{p}{r} = 1 + P_1\sin L + P_2\cos L$$
$$\frac{r}{h} = \frac{h}{\mu(1+P_1\sin L + P_2\cos L)}$$

By defining

$$\vec{r} = X\vec{I} + Y\vec{J} + Z\vec{K}$$
$$\vec{f} = F_X\vec{I} + F_Y\vec{J} + F_Z\vec{K}$$

where (X, Y, Z) are the so-called ECI coordinates, we also obtain the orbital dynamic equations of the following simple form:

$$\ddot{X} = -\mu\frac{X}{r^3} + F_X \quad (92a)$$

$$\ddot{Y} = -\mu\frac{Y}{r^3} + F_Y \quad (92b)$$

$$\ddot{Z} = -\mu\frac{Z}{r^3} + F_Z \quad (92c)$$

where $r = \sqrt{X^2+Y^2+Z^2}$.

2.2.2 Asphericity

The earth is not a perfect sphere; it more closely resembles an oblate spheroid, a body of revolution flattened at the poles. At a finer level of detail the earth can be thought of as pear shaped, but the orbital motion of geosynchronous spacecraft can be analyzed adequately by accounting for the mass distribution associated with the polar flattening

and ignoring the pear shape. The equatorial bulge caused by the polar flattening is only about 21 km; however, this bulge continuously distorts the path of a satellite. The attractive force from the bulge shifts the satellite path northward as the satellite approaches the equatorial plane from the south. As the satellite leaves the equatorial plane, the path is shifted southward. The net result is the ascending node shifts or regresses; it moves westward when the satellite's orbit is prograde, and eastward for a retrograde orbit. In this section, we analyze the effects of the earth's oblateness, characterized by the gravitational coefficient J_2, on the precession of the node line and the regression of the apsidal line of satellite's orbits.

The equatorial cross-section of the earth is elliptical rather than circular, with a 65 m deviation from circular; thus, an oblate spheroid (with a circular cross section at the equator) is a less precise representation of the earth than an ellipsoid with axes of three distinct lengths. When modeling the earth as an ellipsoid, one therefore refers to its *triaxiality*. The tesseral gravitational harmonic coefficient J_{22} of the earth is related to the ellipticity of the earth's equator. There are four equilibrium points separated by approximately 90 deg along the equator: two stable points and two unstable points. The effect of the triaxiality is to cause geosynchronous satellites to oscillate about the nearest stable point on the minor axis. These two stable points, at 75° E longitude and 255° E longitude, are called gravitational valleys. A geosynchronous satellite at the bottom of a gravitational valley is in stable equilibrium. Satellites placed at other longitudes will drift with a 5-year period of oscillation; thus, they require "east-west" stationkeeping maneuvers to maintain their orbital positions. The stable equilibrium points are used among other things as a "junk-yard" for deactivated geosynchronous satellites.

2.2.3 Earth's Anisotropic Gravitational Potential

As discussed in Section 2.2.2, the earth's shape is better represented by an ellipsoid than a sphere, and its mass distribution is not that of a uniform sphere. To account for the nonuniform mass distribution and the resulting nonuniformity in the earth's gravitational field, a gravitational potential is given in general terms by a series of spherical harmonics,

$$U_\oplus(r,\phi,\lambda) = \frac{\mu}{r}\left\{1 + \sum_{n=2}^{\infty}\sum_{m=0}^{n}\left(\frac{R_\oplus}{r}\right)^n P_{nm}(\sin\phi)[C_{nm}\cos m\lambda + S_{nm}\sin m\lambda]\right\} \qquad (93)$$

where the point of interest is described by its geocentric distance r, geocentric latitude ϕ, and geographic longitude λ measured eastward from the Greenwich meridian, and where $R_\oplus$ is the mean equatorial radius of the earth, $\mu = \mu_\oplus$ is the gravitational parameter of the earth, C_{nm} and S_{nm} are the tesseral ($n \neq m$), sectoral ($n = m$), and zonal ($m = 0$) harmonic coefficients characterizing the earth's mass distribution, and P_{nm} is the associated Legendre function of degree n and order m.

The perturbing gravitational potential, U, such that $\vec{f} = (1 + m_2/m_1)\nabla U \approx \nabla U$ becomes the perturbation acceleration, is then defined as

$$\begin{aligned} U &= U_\oplus - \frac{\mu}{r} \\ &= \frac{\mu}{r} \sum_{n=2}^{\infty} \sum_{m=0}^{n} \left(\frac{R_\oplus}{r}\right)^n P_{nm}(\sin\phi)[C_{nm}\cos m\lambda + S_{nm}\sin m\lambda] \end{aligned} \tag{94}$$

By separating the terms independent of longitude, we find

$$\begin{aligned} U =& \frac{\mu}{r}\left\{ -\sum_{n=2}^{\infty} J_n \left(\frac{R_\oplus}{r}\right)^n P_n(\sin\phi) \right. \\ &\left. + \sum_{n=2}^{\infty} \sum_{m=1}^{n} J_{nm} \left(\frac{R_\oplus}{r}\right)^n P_{nm}(\sin\phi)[\cos m(\lambda - \lambda_{nm})] \right\} \end{aligned} \tag{95}$$

where the zonal harmonic coefficient, J_n, is often defined as $J_n \equiv -C_{n0}$ (e.g., $J_2 = +1082.63 \times 10^{-6}$), P_n is Legendre polynomial of degree n defined as $P_n \equiv P_{n0}$, and

$$\begin{aligned} J_{nm} &= \sqrt{C_{nm}^2 + S_{nm}^2} \\ \lambda_{nm} &= \frac{1}{m}\tan^{-1}\left(\frac{S_{nm}}{C_{nm}}\right) \\ P_1(\sin\phi) &= \sin\phi \\ P_2(\sin\phi) &= (3\sin^2\phi - 1)/2 \\ P_3(\sin\phi) &= (5\sin^3\phi - 3\sin\phi)/2 \\ P_4(\sin\phi) &= (35\sin^4\phi - 30\sin^2\phi + 3)/8 \\ P_{11}(\sin\phi) &= (1 - \sin^2\phi)^{1/2} \\ P_{21}(\sin\phi) &= 3\sin\phi(1 - \sin^2\phi)^{1/2} \\ P_{22}(\sin\phi) &= 3(1 - \sin^2\phi) \\ P_{31}(\sin\phi) &= 3(1 - \sin^2\phi)^{1/2}(5\sin^2\phi - 1)/2 \\ P_{32}(\sin\phi) &= 15(1 - \sin^2\phi)\sin\phi \\ P_{33}(\sin\phi) &= 15(1 - \sin^2\phi)^{3/2} \end{aligned}$$

Note that P_n and P_{nm} can be determined from the following formulas:

$$\begin{aligned} P_n(x) &= \frac{1}{2^n n!}\frac{d^n}{dx^n}(x^2 - 1)^n \\ P_{nm}(x) &= \frac{(1 - x^2)^{m/2}}{2^n n!}\frac{d^{n+m}}{dx^{n+m}}(x^2 - 1)^n \end{aligned}$$

A set of numerical values for the coefficients and constants in Eq. (93) is known as a gravitational model. The Goddard Earth Model (GEM) T1 is reported by Marsh et al. [21], with $R_\oplus = 6{,}378.137$ km, and $\mu_\oplus = 398{,}600.436$ km^3/s^2. The normalized values of gravitational coefficients in Ref. [21] have been unnormalized into the following values for J_r and C_{rs}, and used to calculate other parameters, J_{rs} and λ_{rs}:

$J_2 = 1082.63\text{E-}6$	$J_3 = -2.5326\text{E-}6$	$J_4 = -1.6162\text{E-}6$	$J_5 = -0.22812\text{E-}6$
$C_{21} = 0$	$S_{21} = 0$	$C_{22} = 1.57432\text{E-}6$	$S_{22} = -0.903593\text{E-}6$
$C_{31} = 2.192406\text{E-}6$	$S_{31} = 0.269593\text{E-}6$	$C_{32} = 0.30862\text{E-}6$	$S_{32} = -0.211914\text{E-}6$
$C_{33} = 0.100537\text{E-}6$	$S_{33} = 0.197057\text{E-}6$		
$J_{22} = 1.81520\text{E-}6$	$J_{31} = 2.20892\text{E-}6$	$J_{32} = 0.37437\text{E-}6$	$J_{33} = 0.22122\text{E-}6$
$\lambda_{22} = -0.26052$	$\lambda_{31} = 0.12235$	$\lambda_{32} = -0.30085$	$\lambda_{33} = 0.366343$

2.2.4 Earth's Oblateness

The effects of the earth's oblateness on the precession of the node line and the regression of the apsidal line of satellite's orbits can now be analyzed considering the perturbing gravitational potential of the oblate earth given by

$$U = \frac{\mu}{r}\left\{-\frac{J_2 R_\oplus^2}{2r^2}(3\sin^2\phi - 1) - \frac{J_3 R_\oplus^3}{2r^3}(5\sin^3\phi - 3\sin\phi) - \cdots\right\} \tag{96}$$

where r, ϕ, $R_\oplus$, μ, J_2, and J_3 have the same meanings and numerical values as given in Sec. 2.2.3.

As illustrated in Figure 2.5, the angle between the equatorial plane and the radius from the geocenter is called geocentric latitude, while the angle between the equatorial plane and the normal to the surface of the ellipsoid is called geodetic latitude. The commonly used geodetic altitude is also illustrated in Figure 2.5.

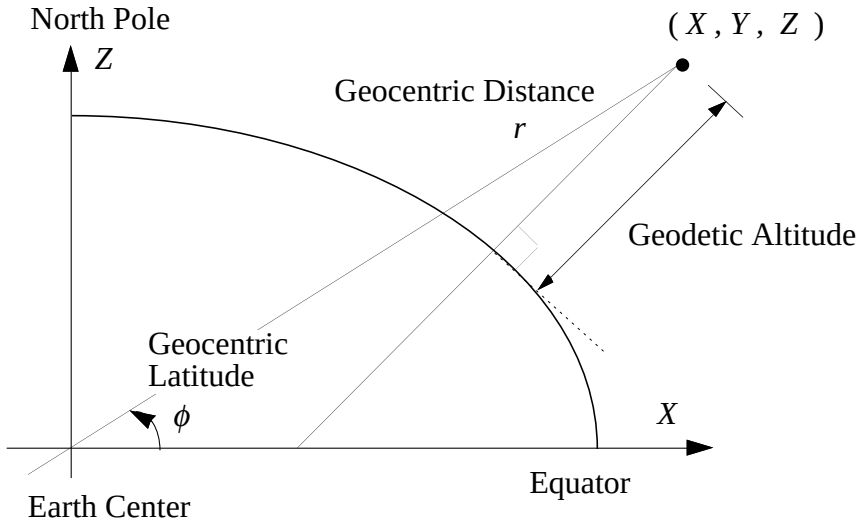

Figure 2.5: A two-dimensional view of the oblate earth.

Ignoring higher-order terms, we consider the perturbing gravitational potential due to J_2, as follows:

$$U = \frac{\mu J_2 R_\oplus^2}{2r^3}(1 - 3\sin^2\phi) \tag{97}$$

Since the geocentric latitude ϕ is related to the orbital elements as:

$$\sin\phi = \frac{Z}{r} = \frac{r\sin(\omega+\theta)\sin i}{r} = \sin(\omega+\theta)\sin i \tag{98}$$

Eq. (97) is rewritten as

$$U = \frac{\mu J_2 R_\oplus^2}{2}\left\{\frac{1}{r^3} - \frac{3\sin^2 i\,\sin^2(\omega+\theta)}{r^3}\right\} \tag{99}$$

Noting that $\vec{r} = r\vec{e}_r$ and $dz = r\sin(\omega+\theta)di$, we can express the perturbing acceleration as

$$\vec{f} = \nabla U = \frac{\partial U}{\partial r}\vec{e}_r + \frac{1}{r}\frac{\partial U}{\partial \theta}\vec{e}_\theta + \frac{1}{r\sin(\omega+\theta)}\frac{\partial U}{\partial i}\vec{e}_z \tag{100}$$

Taking the partial derivatives of U with respect to r, θ, and i, and substituting them into Eq. (100), we obtain the radial, transverse, and normal components of $\vec{f}$, as follows;

$$f_r = -\frac{3\mu J_2 R_\oplus^2}{2r^4}\{1 - 3\sin^2 i\,\sin^2(\omega+\theta)\} \tag{101}$$

$$f_\theta = -\frac{3\mu J_2 R_\oplus^2}{2r^4}\sin^2 i\sin 2(\omega+\theta) \tag{102}$$

$$f_z = -\frac{3\mu J_2 R_\oplus^2}{2r^4}\sin 2i\sin(\omega+\theta) \tag{103}$$

Substituting Eq. (103) into Eq. (65), we obtain the precession of the node line as:

$$\dot{\Omega} = -\frac{3\mu J_2 R_\oplus^2}{r^3\sqrt{\mu p}}\cos i\sin^2(\omega+\theta) \tag{104}$$

Integrating this equation over an entire orbit of period P yields

$$\Delta\Omega = -\frac{3\mu J_2 R_\oplus^2}{\sqrt{\mu p}}\cos i\int_0^P \frac{\sin^2(\omega+\theta)}{r^3}dt \tag{105}$$

where $\Delta\Omega$ denotes the change of Ω over an entire orbit, assuming that changes in other orbital elements are second-order terms. (Note that the average rate of change of i over the orbital period is zero.)

Since the angular momentum $h \equiv |\vec{h}|$ can be expressed as

$$h = \sqrt{\mu p} \approx r^2(\dot{\Omega}\cos i + \dot{\omega} + \dot{\theta}) \tag{106}$$

we have

$$\dot{\omega} + \dot{\theta} \approx \frac{\sqrt{\mu p}}{r^2} \tag{107}$$

in which the second-order term $\dot{\Omega}\cos i$ is further neglected. This equation is used to change the independent variable t into $(\omega + \theta)$, as follows:

$$d(\omega + \theta) = \frac{\sqrt{\mu p}}{r^2} dt$$

Thus, Eq. (105) can be rewritten as

$$\begin{aligned}\Delta\Omega &= -\frac{3J_2 R_\oplus^2}{p}\cos i \int_0^{2\pi} \frac{\sin^2(\omega+\theta)}{r} d(\omega+\theta) \\ &= -\frac{3J_2 R_\oplus^2}{p}\cos i \int_0^{2\pi} \frac{1-\cos 2(\omega+\theta)}{2r} d(\omega+\theta)\end{aligned}$$

Performing the integration after a substitution of $r = p/(1 + e\cos\theta)$ yields

$$\Delta\Omega = -\frac{3\pi J_2 R_\oplus^2}{p^2}\cos i + \text{ higher-order terms} \tag{108}$$

Dividing this by the average orbital period, $P = 2\pi/n$, where $n = \sqrt{\mu/a^3}$ is the orbital mean motion, we obtain the average rate of change of Ω, as follows:

$$\dot{\Omega} \approx -\frac{3J_2 R_\oplus^2}{2p^2} n\cos i \tag{109}$$

Similarly, assuming that the eccentricity and the semimajor axis of the orbit remain unperturbed by the oblateness of the earth to a first-order approximation, we can obtain the average rate of change of ω, as follows:

$$\dot{\omega} \approx -\frac{3J_2 R_\oplus^2}{2p^2} n\left(\frac{5\sin^2 i}{2} - 2\right) \tag{110}$$

For geostationary satellites, we have $\Delta\Omega \approx -4.9$ deg/year and $\Delta\omega \approx 9.8$ deg/year due to the oblateness of the earth.

2.2.5 Earth's Triaxiality

The earth's ellipsoidal shape, or triaxiality, was discussed in Section 2.2.2, where it is noted that the equatorial cross-section is elliptical with one axis 65 m longer than the other. The elliptical nature of the equator is characterized by the tesseral harmonic coefficients C_{22}, S_{22}, C_{32}, S_{32}, etc. The primary tesseral harmonic is denoted by J_{22}, which combines C_{22} and S_{22}, as

$$J_{22} = \sqrt{C_{22}^2 + S_{22}^2}$$

The earth's elliptical equator gives rise to a gravitational acceleration that causes a drift in the longitudinal position of geostationary satellites, which is a major perturbation that must be dealt with.

There are four equilibrium points separated by approximately 90 deg along the equator: two stable points and two unstable points. The effect of the triaxiality is to cause geosynchronous satellites to oscillate about the nearest stable point on the minor axis. These two stable points, at 75° E longitude and 255° E longitude, are called gravitational valleys. A geosynchronous satellite at the bottom of a gravitational valley is in stable equilibrium. Satellites placed at other longitudes will drift with a 5-year period of oscillation; thus, they require "east-west" stationkeeping maneuvers to maintain their orbital positions. The stable equilibrium points are used among other things as a "junk-yard" for deactivated geosynchronous satellites.

Ignoring higher-order terms, the perturbing gravitational potential due to tesseral harmonics C_{22} and S_{22} is defined as

$$\begin{aligned} U &= \frac{3\mu R_\oplus^2}{r^3}(C_{22}\cos 2\lambda + S_{22}\sin 2\lambda)\cos^2\phi \\ &\equiv \frac{3\mu R_\oplus^2}{r^3}\sqrt{C_{22}^2+S_{22}^2}\cos 2(\lambda-\lambda_{22})\cos^2\phi \\ &\equiv \frac{3\mu R_\oplus^2}{r^3}J_{22}\cos 2(\lambda-\lambda_{22})\cos^2\phi \end{aligned} \tag{111}$$

where r is the geocentric distance, λ is the geographic longitude, ϕ is the geocentric latitude, $C_{22} = 1.574321 \times 10^{-6}$, $S_{22} = -0.903593 \times 10^{-6}$, $J_{22} = 1.815204 \times 10^{-6}$, and λ_{22} is defined as

$$\lambda_{22} = \frac{1}{2}\tan^{-1}\left(\frac{S_{22}}{C_{22}}\right) = -0.26052 \text{ rad } = -15 \text{ deg}$$

Using the following relationships

$$\begin{aligned} X &= r\cos\phi\cos\lambda \\ Y &= r\cos\phi\sin\lambda \\ Z &= r\sin\phi \end{aligned}$$

we obtain

$$U = \frac{3\mu R_\oplus^2}{r^5}[C_{22}(X^2-Y^2)+2S_{22}XY] \tag{112}$$

and

$$\begin{aligned} \vec{f} = \nabla U &= \frac{3\mu R_\oplus^2}{r^6}[-5\{C_{22}(X^2-Y^2)+2S_{22}XY\}\vec{e}_r \\ &\quad +2r(C_{22}X+S_{22}Y)\vec{e}_1 + 2r(S_{22}X-C_{22}Y)\vec{e}_2] \\ &\equiv f_r\vec{e}_r + f_\theta\vec{e}_\theta + f_z\vec{k} \end{aligned} \tag{113}$$

where mutually perpendicular unit vectors $\vec{e}_1$ and $\vec{e}_2$ are fixed in the earth: $\vec{e}_1$ lies in the equatorial plane parallel to a line intersecting earth's geometric center and the

Greenwich meridian, and $\vec{e}_2$ lies in the equatorial plane 90 deg eastward of $\vec{e}_1$. Note that in Eqs. (112) and (113), X, Y, and Z mark the position of the satellite in an earth-fixed coordinate system; they do not have the same meanings as in Eq. (29).

The radial, transverse, and normal components of $\vec{f}$ can then be found as

$$\begin{aligned} f_r &= -\frac{9\mu R_\oplus^2}{r^4}(C_{22}\cos 2\lambda + S_{22}\sin 2\lambda)\cos^2\phi \\ f_\theta &= -\frac{6\mu R_\oplus^2}{r^4}(C_{22}\sin 2\lambda - S_{22}\cos 2\lambda)\cos\phi \\ f_z &= -\frac{6\mu R_\oplus^2}{r^4}(C_{22}\cos 2\lambda + S_{22}\sin 2\lambda)\sin\phi\cos\phi \end{aligned} \tag{114}$$

For a geosynchronous satellite with $i \approx 0$ and $r = a$ (i.e., $\phi = 0$), we have

$$\begin{aligned} f_r &= -\frac{9\mu R_\oplus^2}{a^4}(C_{22}\cos 2\lambda + S_{22}\sin 2\lambda) \\ f_\theta &= -\frac{6\mu R_\oplus^2}{a^4}(C_{22}\sin 2\lambda - S_{22}\cos 2\lambda) \\ f_z &= 0 \end{aligned} \tag{115}$$

Using

$$\frac{da}{dt} = \frac{2}{n}f_\theta \quad \text{where} \quad n = \sqrt{\mu/a^3} \tag{116}$$

we can express the longitudinal perturbation acceleration as

$$\ddot{\lambda} = \frac{dn}{dt} = -\frac{3n}{2a}\frac{da}{dt} = -\frac{3n}{2a}\frac{2}{n}f_\theta = -\frac{3}{a}f_\theta \tag{117}$$

and we find

$$\begin{aligned} \ddot{\lambda} &= \frac{18\mu R_\oplus^2}{a^5}(C_{22}\sin 2\lambda - S_{22}\cos 2\lambda) \\ &= \frac{18\mu R_\oplus^2}{a^5}J_{22}\sin 2(\lambda - \lambda_{22}) \end{aligned} \tag{118}$$

where $\lambda_{22} = -0.26052$ rad $= -15$ deg. The equilibrium longitudes, denoted as λ^*, for $\ddot{\lambda} = 0$ can be found as:

$$\begin{aligned} \tan 2\lambda^* &= \frac{S_{22}}{C_{22}} = \frac{-0.90359 \times 10^{-6}}{1.57432 \times 10^{-6}} = -0.57395 \\ &\Rightarrow \lambda^* = 75, 165, 255, 345 \text{ deg} \end{aligned}$$

and λ_{22} corresponds to λ^* of 345 deg. It can be shown that λ^* of 75 deg and 255 deg are stable equilibrium longitudes and that λ^* of 165 deg and 345 deg are unstable equilibrium longitudes.

Since the stable equilibrium points are separated by ±90 deg from λ_{22}, we obtain the following:

$$\begin{aligned}\ddot{\lambda} &= \frac{18\mu R_{\oplus}^2}{a^5} J_{22} \sin 2(\lambda - \lambda_{22}) \\ &= \frac{18\mu R_{\oplus}^2}{a^5} J_{22} \sin 2(\lambda - (\lambda_s \pm \pi/2)) \\ &= -\frac{18\mu R_{\oplus}^2}{a^5} J_{22} \sin 2(\lambda - \lambda_s) \\ &= -0.0017 \sin 2(\lambda - \lambda_s) \ \ \text{deg/day}^2 \end{aligned} \tag{119}$$

where $\lambda_s = 75.3$ and 255.3 deg (stable longitudes).

2.2.6 Luni-Solar Gravitational Perturbations

The gravitational forces exerted by the Sun and Moon on the two bodies of interest, the earth and a geostationary satellite, are referred to as the *luni-solar perturbation*. The equation describing motion of a satellite subject to perturbations is given by

$$\ddot{\vec{r}} + \frac{\mu_{\oplus}}{r^3}\vec{r} = \vec{f} \tag{120}$$

where $\vec{f}$ is the perturbing acceleration caused, in this case, by the luni-solar gravitational effects on the satellite and earth, described by

$$\vec{f} = -\mu_{\otimes}\left(\frac{\vec{r}_{\otimes}}{r_{\otimes}^3} + \frac{\vec{Q}}{Q^3}\right) - \mu_{\odot}\left(\frac{\vec{r}_{\odot}}{r_{\odot}^3} + \frac{\vec{R}}{R^3}\right) \tag{121}$$

and

$$\begin{aligned}\vec{r} &= \text{ position vector of satellite from the earth} \\ &\equiv \vec{Q} + \vec{r}_{\otimes} \ \text{ for the earth-moon-satellite system} \\ &\equiv \vec{R} + \vec{r}_{\odot} \ \text{ for the earth-sun-satellite system} \\ \vec{Q} &= \text{ position vector of the moon from the earth, } Q = 3.84398 \times 10^8 \text{ m} \\ \vec{R} &= \text{ position vector of the sun from the earth, } R = 1AU = 1.496 \times 10^{11} \text{ m} \\ \vec{r}_{\otimes} &= \text{ position vector of satellite from the moon} \\ \vec{r}_{\odot} &= \text{ position vector of satellite from the sun} \\ \mu_{\oplus} &= \text{ the earth's gravitational parameter } = 398,601 \text{ km}^3/\text{s}^2 \\ \mu_{\otimes} &= \text{ the moon's gravitational parameter } = 4,902.8 \text{ km}^3/\text{s}^2 \\ \mu_{\odot} &= \text{ the sun's gravitational parameter } = 1.32686 \times 10^{11} \text{ km}^3/\text{s}^2 \end{aligned}$$

Defining

$$\begin{aligned}
\vec{r} &= X\vec{I} + Y\vec{J} + Z\vec{K} \\
\vec{Q} &= Q_X\vec{I} + Q_Y\vec{J} + Q_Z\vec{K} \\
\vec{R} &= R_X\vec{I} + R_Y\vec{J} + R_Z\vec{K} \\
\vec{f} &= F_X\vec{I} + F_Y\vec{J} + F_Z\vec{K}
\end{aligned}$$

where (X, Y, Z) are the ECI coordinates, we can obtain the components of the luni-solar perturbation vector, as follows:

$$\begin{aligned}
F_X \approx & \frac{\mu_\otimes}{Q^3}\left\{-X + \frac{3r}{Q}\left[\cos\theta_\otimes + \frac{r}{2Q}(5\cos^2\theta_\otimes - 1)\right](Q_X - X)\right\} \\
& + \frac{\mu_\odot}{R^3}\left\{-X + \frac{3r}{R}\left[\cos\theta_\odot + \frac{r}{2R}(5\cos^2\theta_\odot - 1)\right](R_X - X)\right\} \qquad (122) \\
F_Y \approx & \frac{\mu_\otimes}{Q^3}\left\{-Y + \frac{3r}{Q}\left[\cos\theta_\otimes + \frac{r}{2Q}(5\cos^2\theta_\otimes - 1)\right](Q_Y - Y)\right\} \\
& + \frac{\mu_\odot}{R^3}\left\{-Y + \frac{3r}{R}\left[\cos\theta_\odot + \frac{r}{2R}(5\cos^2\theta_\odot - 1)\right](R_Y - Y)\right\} \qquad (123) \\
F_Z \approx & \frac{\mu_\otimes}{Q^3}\left\{-Z + \frac{3r}{Q}\left[\cos\theta_\otimes + \frac{r}{2Q}(5\cos^2\theta_\otimes - 1)\right](Q_Z - Z)\right\} \\
& + \frac{\mu_\odot}{R^3}\left\{-Z + \frac{3r}{R}\left[\cos\theta_\odot + \frac{r}{2R}(5\cos^2\theta_\odot - 1)\right](R_Z - Z)\right\} \qquad (124)
\end{aligned}$$

where $\theta_\otimes$ is the angle between the earth-satellite line and the earth-moon line, $\theta_\odot$ is the angle between the earth-satellite line and the earth-sun line, and

$$\begin{aligned}
Q_X &= Q(\cos\Omega_\otimes\cos\omega_\otimes t - \sin\Omega_\otimes\cos i_\otimes\sin\omega_\otimes t) \\
Q_Y &= Q(\sin\Omega_\otimes\cos\omega_\otimes t + \cos\Omega_\otimes\cos i_\otimes\sin\omega_\otimes t) \\
Q_Z &= Q\sin i_\otimes\sin\omega_\otimes t \\
R_X &= R(\cos\Omega_\odot\cos\omega_\odot t - \sin\Omega_\odot\cos i_\odot\sin\omega_\odot t) \\
R_Y &= R(\sin\Omega_\odot\cos\omega_\odot t + \cos\Omega_\odot\cos i_\odot\sin\omega_\odot t) \\
R_Z &= R\sin i_\odot\sin\omega_\odot t \\
\omega_\otimes &= \text{ orbit rate of the moon } = 2\pi/27.3 \text{ rad/day} \\
\Omega_\otimes &= \text{ the right ascension of the moon} \\
i_\otimes &= \text{the inclination angle of the moon} \\
\omega_\odot &= \text{ orbit rate of the sun } = 2\pi/365.25 \text{ rad/day} \\
\Omega_\odot &= \text{ the right ascension of the Sun} \\
i_\odot &= \text{the declination angle of the Sun}
\end{aligned}$$

The luni-solar gravitational perturbations for typical geosynchronous communications satellites with $i \approx 0$ are summarized by Agrawal [22], as follows:

$$\text{Lunar gravitational perturbation} < 9 \times 10^{-6} \text{ m/s}^2$$
$$\text{Solar gravitational perturbation} < 4 \times 10^{-6} \text{ m/s}^2$$

$$\begin{aligned}\frac{di}{dt} &\approx \frac{3\mu_{\otimes} r^2}{4hr_{\otimes}^3} \sin(\Omega - \Omega_{\otimes}) \sin i_{\otimes} \cos i_{\otimes} + \frac{3\mu_{\odot} r^2}{4hr_{\odot}^3} \sin\Omega \sin i_{\odot} \cos i_{\odot} \\ &\approx 0.478 \text{ to } 0.674 \text{ deg/year} + 0.269 \text{ deg/year}\end{aligned}$$

where Ω is chosen as 90 deg, $\Omega_{\otimes} = 0$ for min/max $i_{\otimes}$, and

$$\mu_{\otimes} = 4.9028 \times 10^3 \text{ km}^3/\text{s}^2$$
$$\mu_{\odot} = 1.32686 \times 10^{11} \text{ km}^3/\text{s}^2$$
$$r_{\otimes} \approx 3.844 \times 10^5 \text{ km}$$
$$r_{\odot} \approx 1.49592 \times 10^8 \text{ km}$$
$$i_{\otimes} = 18.3^{\circ} \text{ to } 28.6^{\circ}$$
$$i_{\odot} = 23.45^{\circ}$$
$$r = 42,164 \text{ km}$$
$$h = 129,640 \text{ km}^2/\text{s}$$

2.2.7 Solar Radiation Pressure

The significant orbital perturbation effect of the solar pressure force on large spacecraft with large area-to-mass ratios has been investigated by many researchers in the past, [10]-[15]. A detailed physical description of the solar radiation pressure can be found in a recent book on solar sailing by McInnes [14]. The solar pressure effects on formation flying of satellites with different area-to-mass ratios were also recently investigated in Ref. [15].

The solar radiation forces are due to photons impinging on a surface in space, as illustrated in Figure 2.6. It is assumed that a fraction, ρ_s, of the impinging photons is specularly reflected, a fraction, ρ_d, is diffusely reflected, and a fraction, ρ_a, is absorbed by the surface. And we have

$$\rho_s + \rho_d + \rho_a = 1 \tag{125}$$

The solar radiation pressure (SRP) force acting on an ideal flat surface is then expressed as

$$\vec{F} = PA(\vec{n} \cdot \vec{s}) \left\{ (\rho_a + \rho_d)\vec{s} + \left(2\rho_s + \frac{2}{3}\rho_d\right)\vec{n} \right\} \tag{126}$$

where $P = 4.5 \times 10^{-6}$ N/m^2 is the nominal solar radiation pressure constant, A is the surface area, $\vec{n}$ is a unit vector normal to the surface, and $\vec{s}$ is a unit vector pointing from the sun to satellite.

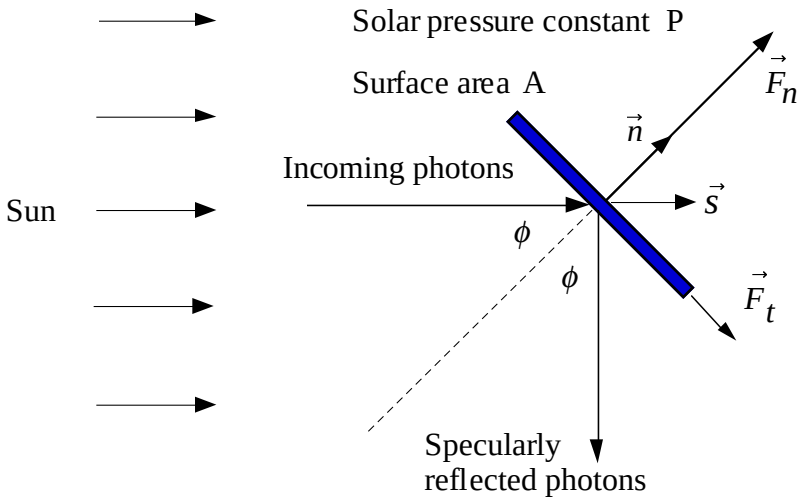

Figure 2.6: Solar radiation pressure force acting on an ideal flat surface (a case with 45-deg pitch angle ϕ is shown here).

For an ideal case of a perfect mirror with $\rho_d = \rho_a = 0$ and $\rho_s = 1$, we have $\vec{F}_t = 0$ and

$$\vec{F} = \vec{F}_n = P(A\cos\phi)2\vec{n}$$

where $A\cos\phi$ is called the projected area of the surface under consideration. Also for an ideal case of a black body with $\rho_s = \rho_d = 0$ and $\rho_a = 1$, we have

$$\vec{F} = P(A\cos\phi)\vec{s}$$

For most practical cases of satellites with small pitch angles, the SRP perturbation force per unit mass is simply modeled as

$$\vec{f} = P(1+\rho)(A/m)\vec{s} \tag{127}$$

where ρ is the overall surface reflectance (0 for a black body and 1 for a mirror) and A/m is the area-to-mass ratio.

Defining $\vec{f} = f_r\vec{e}_r + f_\theta\vec{e}_\theta + f_z\vec{e}_z$ and ignoring the effects of seasonal variations of the sun vector, we have

$$f_r \approx f\sin\theta$$
$$f_\theta \approx f\cos\theta$$

where $f = P(1+\rho)(A/m)$.

From the orbit perturbation analysis, we have

$$\frac{da}{dt} = \frac{2}{n\sqrt{1-e^2}}\{f_r e\sin\theta + f_\theta(1+e\cos\theta)\}$$
$$\frac{de}{dt} = \frac{\sqrt{1-e^2}}{na}\{f_r\sin\theta + f_\theta(\cos\theta+\cos E)\}$$

For geosynchronous satellites with $e \approx 0$, we obtain

$$\begin{aligned} \frac{da}{dt} &= \frac{2}{n} f_\theta = \frac{2f}{n} \sin\theta \\ &\Rightarrow \Delta a = 0 \text{ per day} \end{aligned} \tag{128}$$

and

$$\begin{aligned} \frac{de}{dt} &= \frac{1}{na}(f_r \sin\theta + 2 f_\theta \cos\theta) \\ &= \frac{1}{na}(f \sin^2\theta + 2f\cos^2\theta) \\ &= \frac{f}{na}\left(\frac{3}{2} + \frac{1}{2}\cos 2\theta\right) \\ \Rightarrow \quad \Delta e &\approx \frac{3\pi f}{n^2 a} \text{ per day} \end{aligned} \tag{129}$$

The solar radiation pressure effect on the longitude change can also be found as

$$\begin{aligned} \ddot{\lambda} = \frac{dn}{dt} &= -\frac{3n}{2a}\frac{da}{dt} = -\frac{3n}{2a}\frac{2}{n} f_\theta = -\frac{3}{a} f_\theta \\ &= -\frac{3f}{a}\cos\theta \end{aligned} \tag{130}$$

2.2.8 Orbit Simulation Results

Orbit simulation results for the Abacus satellite with the effects of the earth's oblateness and triaxiality, luni-solar perturbations, and 60-N solar pressure force are shown in Figures 2.7 and 2.8. The significance of the orbital perturbation effects on the eccentricity and inclination can be seen in these figures.

Orbit control simulation results with the effects of earth's oblateness and triaxiality, luni-solar perturbations, 60-N solar pressure force, and simultaneous orbit and attitude control thruster firings are shown in Figures 2.9 and 2.10. In Figure 2.9, F_Z is the orbit inclination control force and F_X is the solar pressure countering force resulting from countering the pitch gravity-gradient torque. It can be seen that the inclination, eccentricity, satellite longitude location, and the Z-axis orbital position are all properly maintained. The feasibility of using continuous (non-impulsive) firings of ion thrusters for simultaneous eccentricity and inclination control is demonstrated.

The initial values used in the simulations correspond to a circular, equatorial orbit of radius 42164.169 km; therefore, the initial orbital elements are

$$\begin{aligned} a &= 42164.169 \text{ km} \\ e &= 0 \\ i &= 0 \text{ deg} \\ \Omega &= 0 \text{ deg} \\ \omega &= 0 \text{ deg} \end{aligned}$$

The epoch used to calculate the solar and lunar positions, as well as the Earth's orientation in inertial space, is March 21, 2000. In order to place the spacecraft at an initial terrestrial longitude of 75.07 deg (one of the stable longitudes), a true anomaly θ of 253.89 deg is used.

These elements correspond to an initial position and velocity of

$$\begin{aligned} \vec{r} &= -11698.237\,\vec{I} - 40508.869\,\vec{J} + 0\vec{K} \text{ km} \\ \vec{v} &= \quad 2.954\,\vec{I} - \quad 0.853\,\vec{J} + 0\vec{K} \text{ km/s} \end{aligned}$$

The orbit control problem of geosynchronous satellites is a topic of continuing practical interest. Detailed technical descriptions of standard north-south and east-west stationkeeping control techniques as well as more advanced orbit control concepts can be found in Refs. [11]-[13] and [18]-[20].

In the next section, we develop an attitude dynamics model of sun-pointing spacecraft in geosynchronous orbit for attitude control systems architecture design.

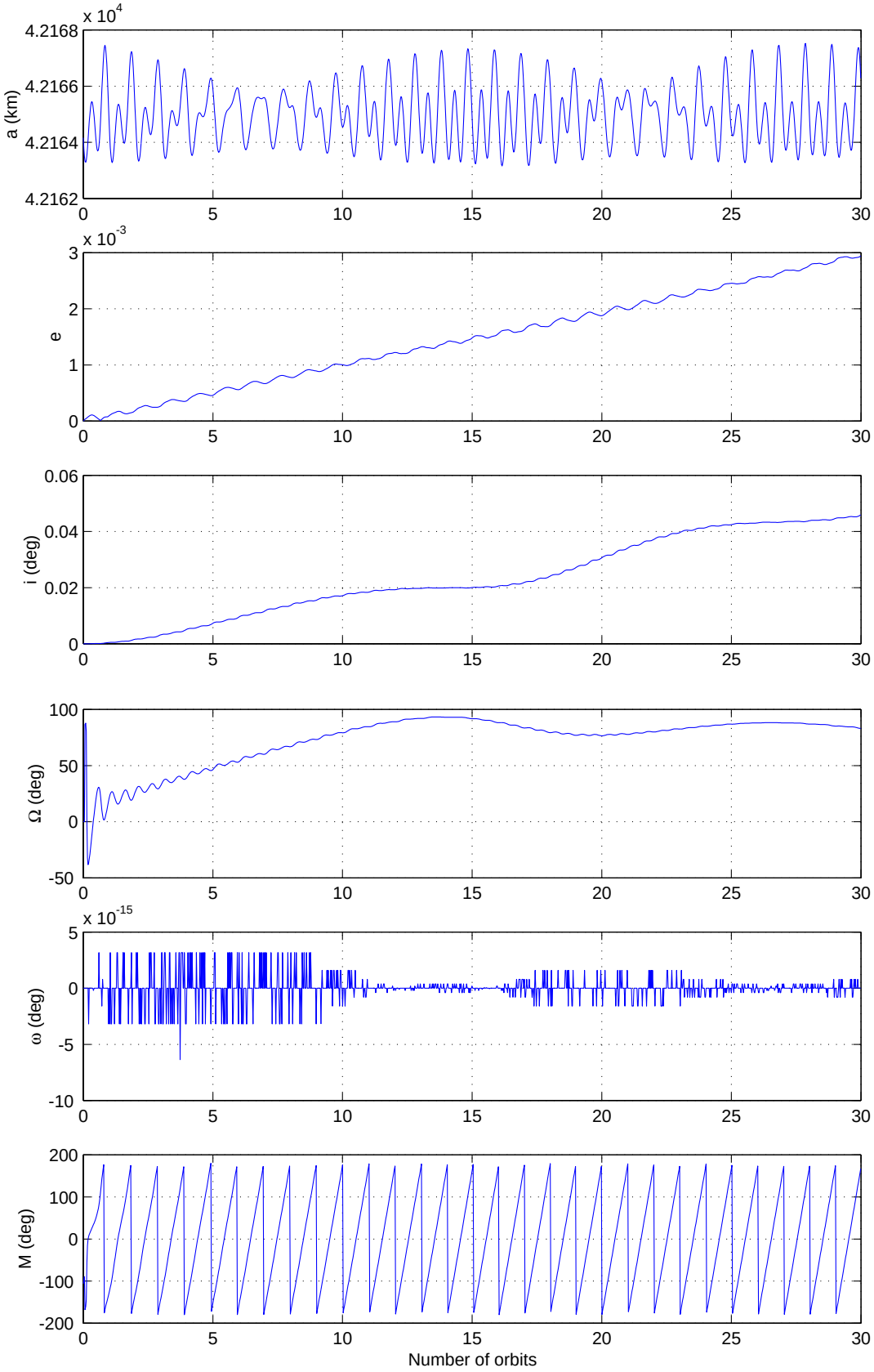

Figure 2.7: Orbit simulation results with the effects of the earth's oblateness and triaxiality, luni-solar perturbations, and 60-N solar pressure force.

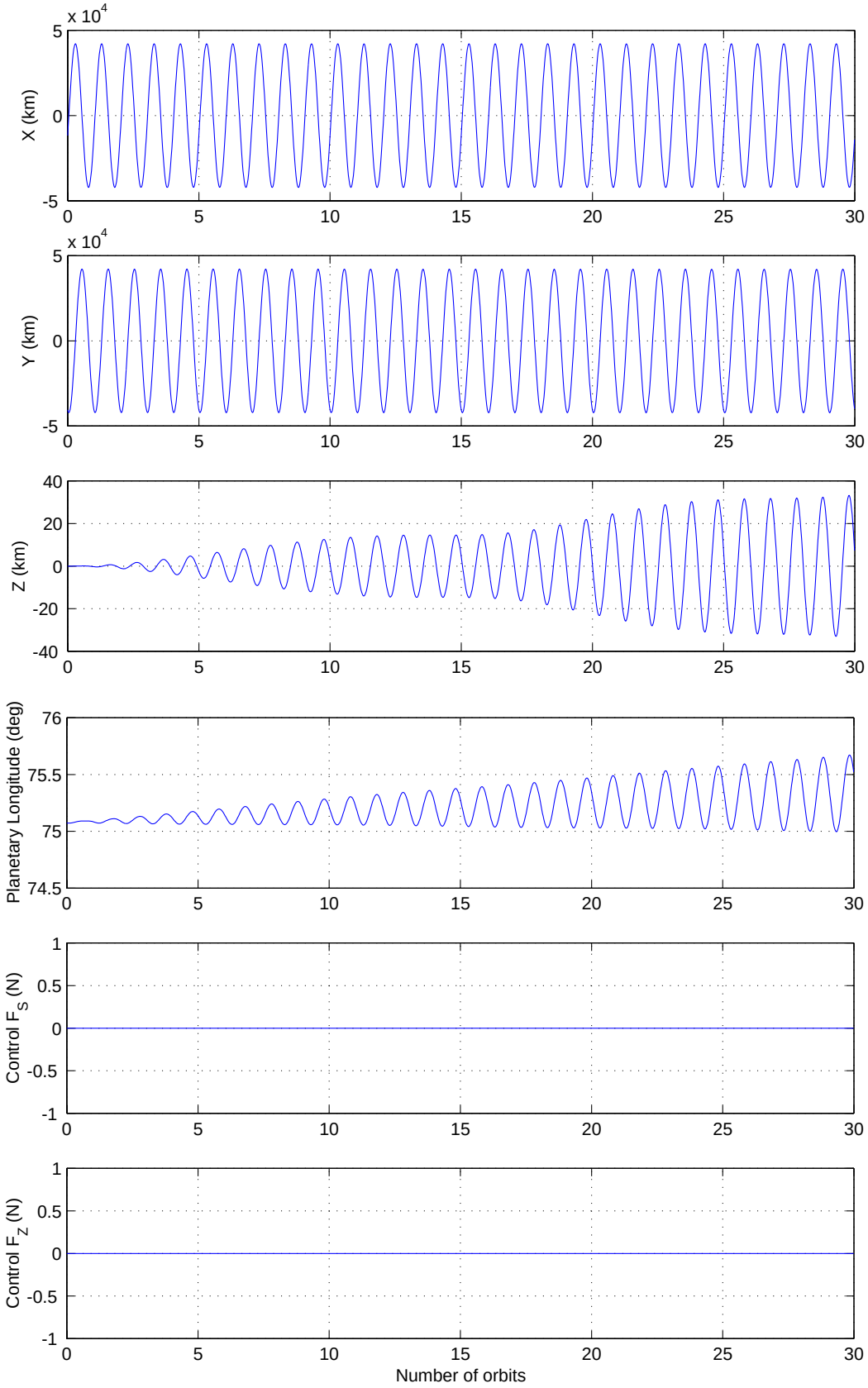

Figure 2.8: Orbit simulation results with the effects of the earth's oblateness and triaxiality, luni-solar perturbations, and 60-N solar pressure force (continued).

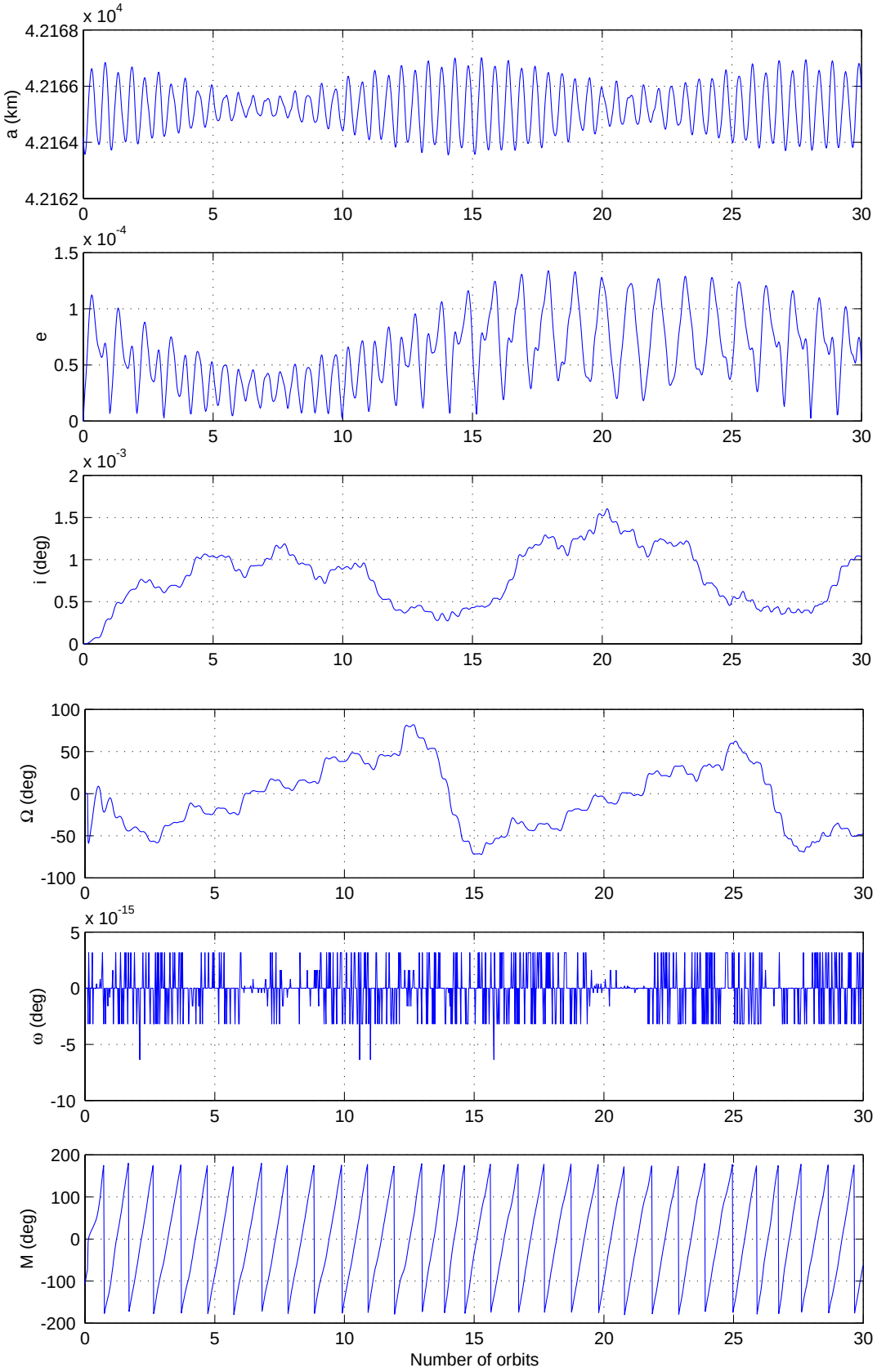

Figure 2.9: Orbit control simulation results with continuous (non-impulsive) eccentricity and inclination control.

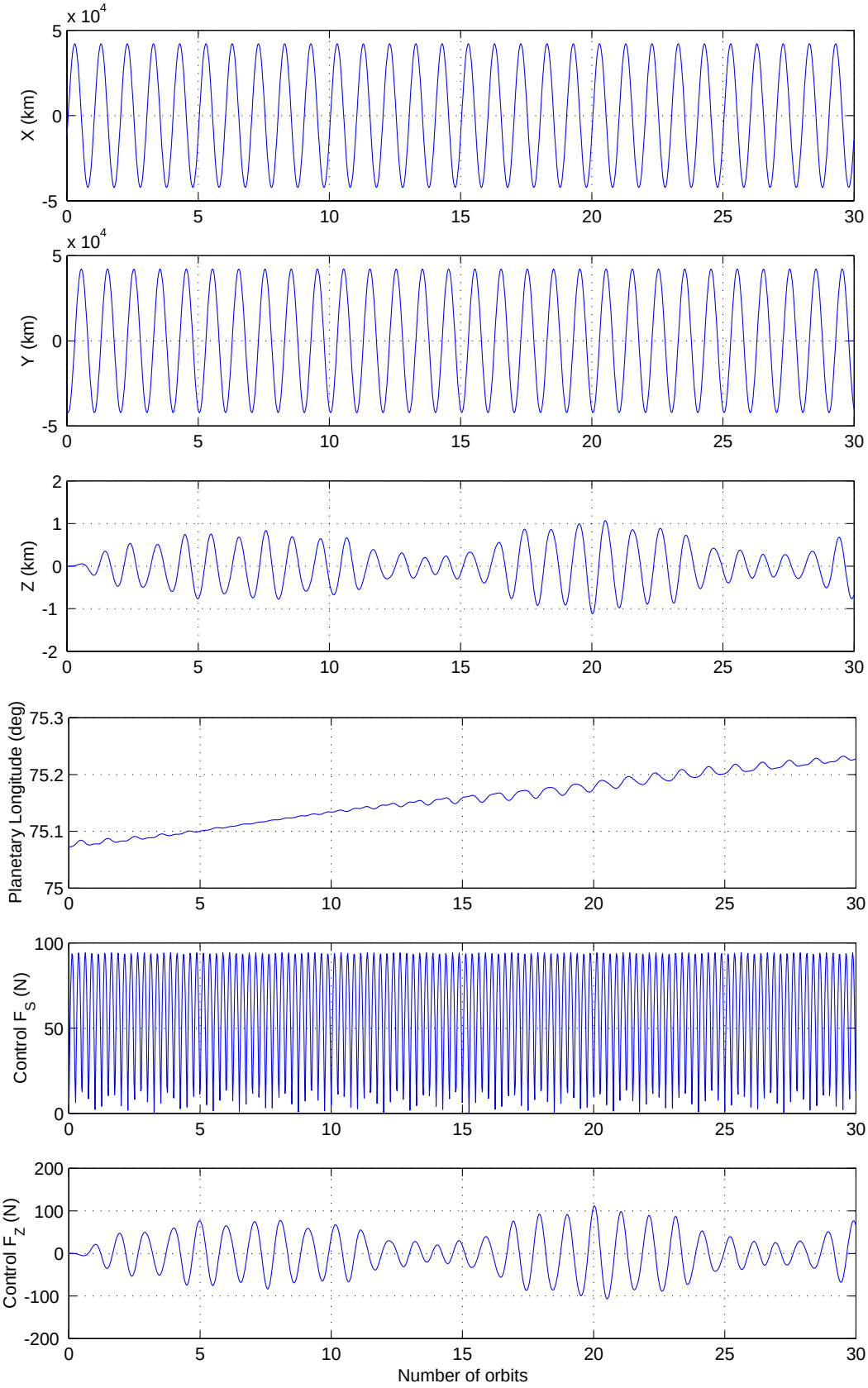

Figure 2.10: Orbit control simulation results with continuous (non-impulsive) eccentricity and inclination control (continued).

2.3 Rigid-Body Attitude Equations of Motion

Consider a rigid body in a circular orbit. A *local vertical and local horizontal (LVLH)* reference frame A with its origin at the center of mass of an orbiting spacecraft has a set of unit vectors $\{\vec{a}_1, \vec{a}_2, \vec{a}_3\}$ with $\vec{a}_1$ along the orbit direction, $\vec{a}_2$ perpendicular to the orbit plane, and $\vec{a}_3$ toward the earth, as illustrated in Figure 2.11. The angular velocity of A with respect to an inertial or Newtonian reference frame N is

$$\vec{\omega}^{A/N} = -n\vec{a}_2 \tag{131}$$

where n is the constant orbital rate. The angular velocity of the body-fixed reference frame B with basis vectors $\{\vec{b}_1, \vec{b}_2, \vec{b}_3\}$ is then given by

$$\vec{\omega}^{B/N} = \vec{\omega}^{B/A} + \vec{\omega}^{A/N} = \vec{\omega}^{B/A} - n\vec{a}_2 \tag{132}$$

where $\vec{\omega}^{B/A}$ is the angular velocity of B relative to A.

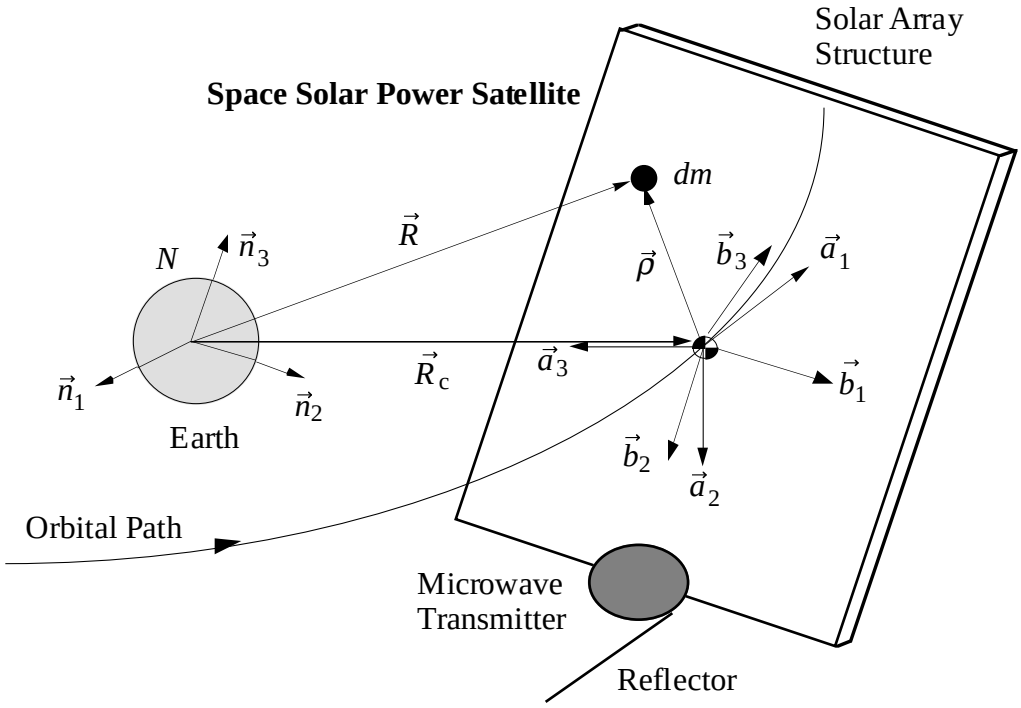

Figure 2.11: A large space solar power satellite in geosynchronous orbit.

The orientation of the body-fixed reference frame B with respect to the LVLH reference frame A is in general described by the direction cosine matrix $\mathbf{C}$ as follows:

$$\begin{bmatrix} \vec{b}_1 \\ \vec{b}_2 \\ \vec{b}_3 \end{bmatrix} = \begin{bmatrix} C_{11} & C_{12} & C_{13} \\ C_{21} & C_{22} & C_{23} \\ C_{31} & C_{32} & C_{33} \end{bmatrix} \begin{bmatrix} \vec{a}_1 \\ \vec{a}_2 \\ \vec{a}_3 \end{bmatrix} \tag{133}$$

or

$$\begin{bmatrix} \vec{a}_1 \\ \vec{a}_2 \\ \vec{a}_3 \end{bmatrix} = \begin{bmatrix} C_{11} & C_{21} & C_{31} \\ C_{12} & C_{22} & C_{32} \\ C_{13} & C_{23} & C_{33} \end{bmatrix} \begin{bmatrix} \vec{b}_1 \\ \vec{b}_2 \\ \vec{b}_3 \end{bmatrix} \tag{134}$$

When earth is modeled as a sphere with uniform mass distribution, the gravitational force acting on a small mass element with a mass of dm is given by

$$d\vec{f} = -\frac{\mu \vec{R} dm}{|\vec{R}|^3} = -\frac{\mu(\vec{R}_c + \vec{\rho})dm}{|\vec{R}_c + \vec{\rho}|^3} \tag{135}$$

where μ is the gravitational parameter of the earth, $\vec{R}$ and $\vec{\rho}$ are the position vectors of the small mass element from the earth's center and the spacecraft's mass center, respectively, and $\vec{R}_c$ is the position vector of the spacecraft's mass center from the earth's center.

The gravity-gradient torque about the spacecraft's mass center is then expressed as:

$$\vec{M} = \int \vec{\rho} \times d\vec{f} = -\mu \int \frac{\vec{\rho} \times \vec{R}_c}{|\vec{R}_c + \vec{\rho}|^3} dm \tag{136}$$

and we have the following approximation

$$\begin{aligned} |\vec{R}_c + \vec{\rho}|^{-3} &= R_c^{-3} \left\{ 1 + \frac{2(\vec{R}_c \cdot \vec{\rho})}{R_c^2} + \frac{\rho^2}{R_c^2} \right\}^{-3/2} \\ &= {R_c}^{-3} \left\{ 1 - \frac{3(\vec{R}_c \cdot \vec{\rho})}{R_c^2} + \text{higher-order terms} \right\} \end{aligned} \tag{137}$$

where $R_c = |\vec{R}_c|$ and $\rho = |\vec{\rho}|$. By definition of the mass center, $\int \vec{\rho} dm = \vec{0}$; therefore, the gravity-gradient torque neglecting the higher-order terms can be written as

$$\vec{M} = \frac{3\mu}{R_c^5} \int (\vec{R}_c \cdot \vec{\rho})(\vec{\rho} \times \vec{R}_c) dm \tag{138}$$

This equation is further manipulated as follows:

$$\begin{aligned} \vec{M} &= -\frac{3\mu}{R_c^5} \vec{R}_c \times \int \vec{\rho}(\vec{\rho} \cdot \vec{R}_c) dm \\ &= -\frac{3\mu}{R_c^5} \vec{R}_c \times \int \vec{\rho}\vec{\rho} dm \cdot \vec{R}_c \\ &= -\frac{3\mu}{R_c^5} \vec{R}_c \times [\int \rho^2 \hat{I} dm - \hat{J}] \cdot \vec{R}_c \\ &= -\frac{3\mu}{R_c^5} \vec{R}_c \times \int \rho^2 \hat{I} dm \cdot \vec{R}_c + \frac{3\mu}{R_c^5} \vec{R}_c \times \hat{J} \cdot \vec{R}_c \\ &= \frac{3\mu}{R_c^5} \vec{R}_c \times \hat{J} \cdot \vec{R}_c \end{aligned}$$

since $\hat{J} = \int(\rho^2\hat{I} - \vec{\rho}\vec{\rho})dm$ and $\vec{R}_c \times \hat{I} \cdot \vec{R}_c = \vec{R}_c \times \vec{R}_c = 0$. The inertia dyadic of the spacecraft with respect to its mass center is denoted by $\hat{J}$, and $\hat{I}$ represents the unit dyadic.

Finally, the gravity-gradient torque is expressed in vector-dyadic form [17], [23] as:

$$\vec{M} = 3n^2\vec{a}_3 \times \hat{J} \cdot \vec{a}_3 \tag{139}$$

where $n = \sqrt{\mu/R_c^3}$ is the orbital rate and $\vec{a}_3 \equiv -\vec{R}_c/R_c$.

In addition to the contribution to gravitational force (see Sec. 2.2.4), earth's oblateness makes a contribution to gravity-gradient torque, shown in Ref. [23] to have a coefficient of $3\mu J_2 R_\oplus^2/R_c^5$. By comparing this to the coefficient above, $3\mu/R_c^3$, it is seen that at geosynchronous orbit the contribution of J_2 to gravity-gradient torque is approximately 5 orders of magnitude less than the main term.

The rotational equation of motion of a rigid body with an angular momentum $\vec{H} = \hat{J} \cdot \vec{\omega}^{B/N}$ in a circular orbit is then given by

$$\left\{\frac{d\vec{H}}{dt}\right\}_N \equiv \left\{\frac{d\vec{H}}{dt}\right\}_B + \vec{\omega}^{B/N} \times \vec{H} = \vec{M}$$

where $\{d/dt\}_N$ indicates differentiation with respect to time in reference frame N, and $\{d/dt\}_B$ indicates differentiation with respect to time in reference frame B. The relationship can be rewritten as

$$\hat{J} \cdot \dot{\vec{\omega}} + \vec{\omega} \times \hat{J} \cdot \vec{\omega} = 3n^2\vec{a}_3 \times \hat{J} \cdot \vec{a}_3 \tag{140}$$

where $\vec{\omega} \equiv \vec{\omega}^{B/N}$, and note that $\dot{\vec{\omega}} = \{d\vec{\omega}/dt\}_N \equiv \{d\vec{\omega}/dt\}_B$.

Since $\vec{\omega}$, $\vec{a}_3$, and $\hat{J}$ can be expressed in terms of basis vectors of the body-fixed reference frame B as

$$\vec{\omega} = \omega_1\vec{b}_1 + \omega_2\vec{b}_2 + \omega_3\vec{b}_3 \tag{141}$$

$$\vec{a}_3 = C_{13}\vec{b}_1 + C_{23}\vec{b}_2 + C_{33}\vec{b}_3 \tag{142}$$

$$\hat{J} = \sum_{i=1}^{3}\sum_{j=1}^{3} J_{ij}\vec{b}_i\vec{b}_j$$

the nonlinear equations of motion in matrix form become

$$\begin{bmatrix} J_{11} & J_{12} & J_{13} \\ J_{21} & J_{22} & J_{23} \\ J_{31} & J_{32} & J_{33} \end{bmatrix} \begin{bmatrix} \dot{\omega}_1 \\ \dot{\omega}_2 \\ \dot{\omega}_3 \end{bmatrix} + \begin{bmatrix} 0 & -\omega_3 & \omega_2 \\ \omega_3 & 0 & -\omega_1 \\ -\omega_2 & \omega_1 & 0 \end{bmatrix} \begin{bmatrix} J_{11} & J_{12} & J_{13} \\ J_{21} & J_{22} & J_{23} \\ J_{31} & J_{32} & J_{33} \end{bmatrix} \begin{bmatrix} \omega_1 \\ \omega_2 \\ \omega_3 \end{bmatrix}$$
$$= 3n^2 \begin{bmatrix} 0 & -C_{33} & C_{23} \\ C_{33} & 0 & -C_{13} \\ -C_{23} & C_{13} & 0 \end{bmatrix} \begin{bmatrix} J_{11} & J_{12} & J_{13} \\ J_{21} & J_{22} & J_{23} \\ J_{31} & J_{32} & J_{33} \end{bmatrix} \begin{bmatrix} C_{13} \\ C_{23} \\ C_{33} \end{bmatrix}$$

To describe the orientation of the body-fixed reference frame B with respect to the LVLH reference frame A in terms of three Euler angles θ_i $(i = 1, 2, 3)$, consider the sequence of $\mathbf{C}_1(\theta_1) \leftarrow \mathbf{C}_3(\theta_3) \leftarrow \mathbf{C}_2(\theta_2)$ from the LVLH reference frame A to a body-fixed reference frame B. For this rotational sequence, we have

$$\begin{aligned}
\begin{bmatrix} \vec{b}_1 \\ \vec{b}_2 \\ \vec{b}_3 \end{bmatrix} &= \begin{bmatrix} C_{11} & C_{12} & C_{13} \\ C_{21} & C_{22} & C_{23} \\ C_{31} & C_{32} & C_{33} \end{bmatrix} \begin{bmatrix} \vec{a}_1 \\ \vec{a}_2 \\ \vec{a}_3 \end{bmatrix} \\
&= \begin{bmatrix} \mathrm{c}\,\theta_2\,\mathrm{c}\,\theta_3 & \mathrm{s}\,\theta_3 & -\mathrm{s}\,\theta_2\,\mathrm{c}\,\theta_3 \\ -\mathrm{c}\,\theta_1\,\mathrm{c}\,\theta_2\,\mathrm{s}\,\theta_3 + \mathrm{s}\,\theta_1\,\mathrm{s}\,\theta_2 & \mathrm{c}\,\theta_1\,\mathrm{c}\,\theta_3 & \mathrm{c}\,\theta_1\,\mathrm{s}\,\theta_2\,\mathrm{s}\,\theta_3 + \mathrm{s}\,\theta_1\,\mathrm{c}\,\theta_2 \\ \mathrm{s}\,\theta_1\,\mathrm{c}\,\theta_2\,\mathrm{s}\,\theta_3 + \mathrm{c}\,\theta_1\,\mathrm{s}\,\theta_2 & -\mathrm{s}\,\theta_1\,\mathrm{c}\,\theta_3 & -\mathrm{s}\,\theta_1\,\mathrm{s}\,\theta_2\,\mathrm{s}\,\theta_3 + \mathrm{c}\,\theta_1\,\mathrm{c}\,\theta_2 \end{bmatrix} \begin{bmatrix} \vec{a}_1 \\ \vec{a}_2 \\ \vec{a}_3 \end{bmatrix}
\end{aligned}$$

where $\mathrm{c}\,\theta_i = \cos\theta_i$ and $\mathrm{s}\,\theta_i = \sin\theta_i$.

And also we have the following kinematic differential equations:

$$\begin{bmatrix} \dot{\theta}_1 \\ \dot{\theta}_2 \\ \dot{\theta}_3 \end{bmatrix} = \frac{1}{\cos\theta_3} \begin{bmatrix} \cos\theta_3 & -\cos\theta_1 \sin\theta_3 & \sin\theta_1 \sin\theta_3 \\ 0 & \cos\theta_1 & -\sin\theta_1 \\ 0 & \sin\theta_1 \cos\theta_3 & \cos\theta_1 \cos\theta_3 \end{bmatrix} \begin{bmatrix} \omega_1 \\ \omega_2 \\ \omega_3 \end{bmatrix} + \begin{bmatrix} 0 \\ n \\ 0 \end{bmatrix} \tag{143}$$

The dynamical equations of motion about the body-fixed principal axes become

$$J_1\dot{\omega}_1 - (J_2 - J_3)\omega_2\omega_3 = -3n^2(J_2 - J_3)C_{23}C_{33} \tag{144}$$
$$J_2\dot{\omega}_2 - (J_3 - J_1)\omega_3\omega_1 = -3n^2(J_3 - J_1)C_{33}C_{13} \tag{145}$$
$$J_3\dot{\omega}_3 - (J_1 - J_2)\omega_1\omega_2 = -3n^2(J_1 - J_2)C_{13}C_{23} \tag{146}$$

where

$$\begin{aligned}
C_{13} &= -\sin\theta_2 \cos\theta_3 \\
C_{23} &= \cos\theta_1 \sin\theta_2 \sin\theta_3 + \sin\theta_1 \cos\theta_2 \\
C_{33} &= -\sin\theta_1 \sin\theta_2 \sin\theta_3 + \cos\theta_1 \cos\theta_2
\end{aligned}$$

for the sequence of $\mathbf{C}_1(\theta_1) \leftarrow \mathbf{C}_3(\theta_3) \leftarrow \mathbf{C}_2(\theta_2)$.

One may linearize Eqs. (143)–(146) "about" an LVLH orientation while admitting a large pitch angle as follows. Assume θ_1 and θ_3 remain small, allow θ_2 to be large, assume ω_1 and ω_3 are small, and ω_2 is equal to the sum of a small quantity and $-n$. Equations that are linear in the small quantities are

$$\begin{aligned}
&J_1\ddot{\theta}_1 + (1 + 3\cos^2\theta_2)n^2(J_2 - J_3)\theta_1 - n(J_1 - J_2 + J_3)\dot{\theta}_3 \\
&\qquad + 3(J_2 - J_3)n^2(\sin\theta_2 \cos\theta_2)\theta_3 = u_1 + d_1 \\
&J_2\ddot{\theta}_2 + 3n^2(J_1 - J_3)\sin\theta_2 \cos\theta_2 = u_2 + d_2 \\
&J_3\ddot{\theta}_3 + (1 + 3\sin^2\theta_2)n^2(J_2 - J_1)\theta_3 + n(J_1 - J_2 + J_3)\dot{\theta}_1 \\
&\qquad + 3(J_2 - J_1)n^2(\sin\theta_2 \cos\theta_2)\theta_1 = u_3 + d_3
\end{aligned}$$

where u_i and d_i are control and disturbance torques, respectively.

For a quasi-inertially stabilized, sun-pointing SSP satellite in geosynchronous orbit with small body rates, ω_i $(i = 1, 2, 3)$, and small roll/yaw angles, θ_1 and θ_3, the kinematic differential equations, (143), can be linearized in the small quantities:

$$\begin{aligned}
\dot{\theta}_1 &\approx \omega_1 \\
\dot{\theta}_2 &\approx \omega_2 + n \\
\dot{\theta}_3 &\approx \omega_3
\end{aligned}$$

Finally, the equations of motion of a sun-pointing spacecraft with small roll and yaw angles can be found as

$$J_1\ddot{\theta}_1 = -3n^2(J_2 - J_3)(\cos^2\theta_2)\theta_1 - 3(J_2 - J_3)n^2(\sin\theta_2\cos\theta_2)\theta_3 + u_1 + d_1 \quad (147a)$$

$$J_2\ddot{\theta}_2 = -3n^2(J_1 - J_3)\sin\theta_2\cos\theta_2 + u_2 + d_2 \quad (147b)$$

$$J_3\ddot{\theta}_3 = -3n^2(J_2 - J_1)(\sin^2\theta_2)\theta_3 - 3(J_2 - J_1)n^2(\sin\theta_2\cos\theta_2)\theta_1 + u_3 + d_3 \quad (147c)$$

The pitch angle relative to LVLH, θ_2, is not restricted to be small, but it may be regarded as a sum, $\theta_2 = nt + \delta\theta_2$, where $\delta\theta_2$ is a small pitch attitude error. Kinematical and dynamical differential equations can then be made linear in the small quantities ω_1, ω_2, ω_3, θ_1, $\delta\theta_2$, and θ_3. For such a case, Eqs. (143) become

$$\begin{aligned}
\dot{\theta}_1 &\approx \omega_1 \\
\delta\dot{\theta}_2 &\approx \omega_2 \\
\dot{\theta}_3 &\approx \omega_3
\end{aligned}$$

and Eqs. (147) become

$$J_1\ddot{\theta}_1 = -3n^2(J_2 - J_3)[(\cos^2 nt)\theta_1 + (\sin nt\cos nt)\theta_3] + u_1 + d_1 \quad (148a)$$

$$J_2\,\delta\ddot{\theta}_2 = -3n^2(J_1 - J_3)[(\cos^2 nt - \sin^2 nt)\delta\theta_2 + \sin nt\cos nt] + u_2 + d_2 \quad (148b)$$

$$J_3\ddot{\theta}_3 = -3n^2(J_2 - J_1)[(\sin^2 nt)\theta_3 + (\sin nt\cos nt)\theta_1] + u_3 + d_3 \quad (148c)$$

where $(\theta_1, \delta\theta_2, \theta_3)$ are the small roll, pitch, and yaw attitude errors of a sun-pointing spacecraft, respectively.

Equations (147) or (148) are the attitude equations of motion of the Abacus satellite for control design in the presence of the external disturbances, d_i, in units of N-m, modeled as:

$$\begin{aligned}
d_1 &\approx 12,000 - 11,900\cos nt \\
d_2 &\approx 1,200 \\
d_3 &\approx -11,900\sin nt
\end{aligned}$$

However, $\pm 20\%$ uncertainties in this disturbance model as well as the inertia properties should be considered in control design.

2.4 Abacus Satellite Structural Models

In Refs. [24]-[26], dynamics and control problems of large flexible platforms in space, such as the square Abacus platform, have been investigated. The flexible structure dynamics and control problem is a topic of continuing practical as well as theoretical interest. However, a significant control-structure interaction problem, possible for such very large Abacus platform (3.2 km by 3.2 km) with the lowest structural mode frequency of about 0.002 Hz, is avoided simply by designing an attitude control system with very low bandwidth ($<$ orbit frequency of 1×10^{-5} Hz). The proposed low-bandwidth attitude control system, however, utilizes a concept of cyclic-disturbance accommodation control to provide ± 5 arcmin pointing of the Abacus platform in the presence of large external disturbances and dynamic modeling uncertainties. Consequently, the flexible structure control problem is not further investigated in this study, while a structural dynamic interaction problem with thermal distortion needs to be investigated in a future study.

Various structural concepts for providing the required stiffness and rigidity of the Abacus platform are illustrated in Figure 2.12. Finite-element modeling of the baseline Abacus platform is illustrated in Figure 2.13 and the first three vibration modes are shown in Figure 2.14. Selected node locations for control analysis and design are shown in Figure 2.15. Typical pole-zero patterns of reduced-order transfer functions can be seen in Figure 2.16. Computer simulation results of a reduced-order structural model with the lowest 16 modes, confirm that the control-structure interaction problem can be simply avoided by the low-bandwidth attitude control system. Detailed technical discussions of the dynamics and control problems of flexible spacecraft can be found in the literature (e.g., see Refs. [17] and [27]), and thus the structural control problem of the Abacus satellite is not elaborated in this report.

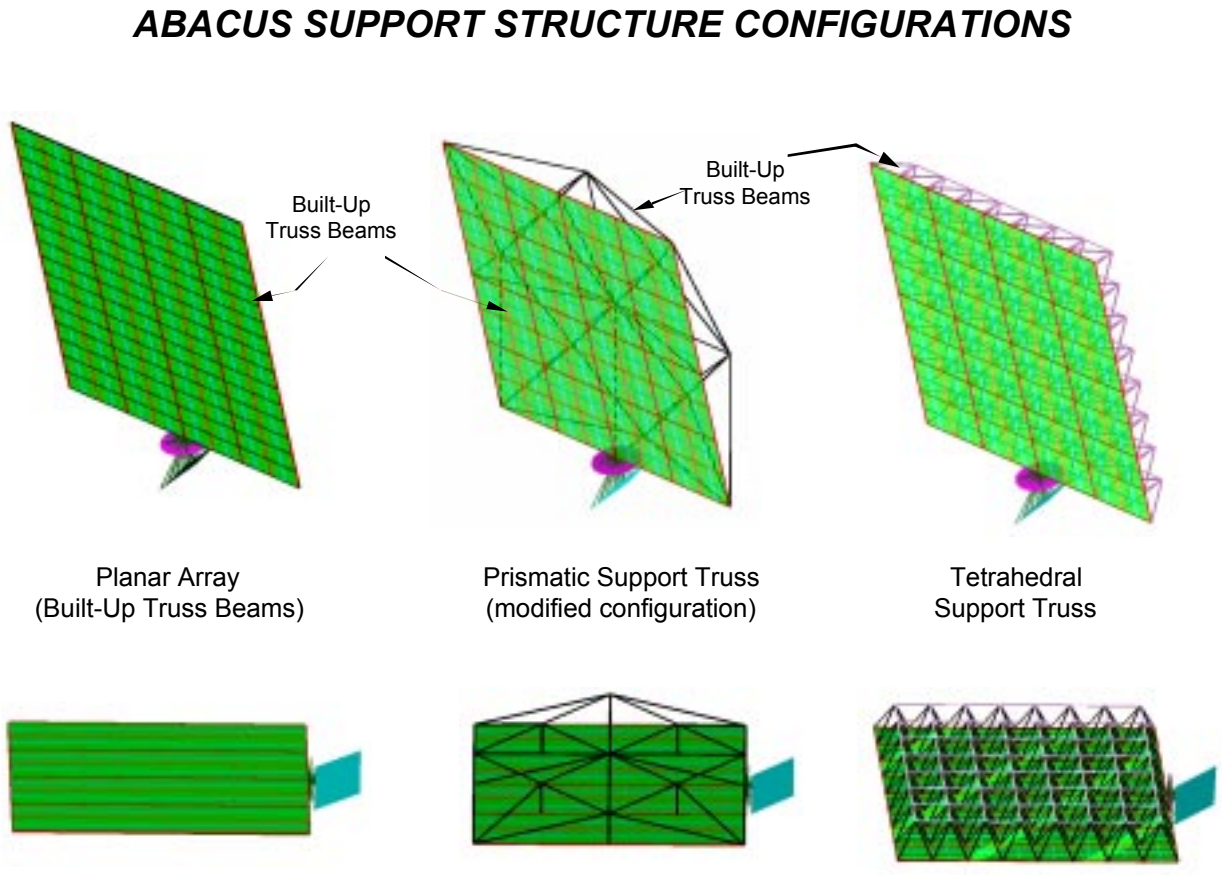

Figure 2.12: Abacus structural platform concepts (Courtesy of Tim Collins at NASA LaRC).

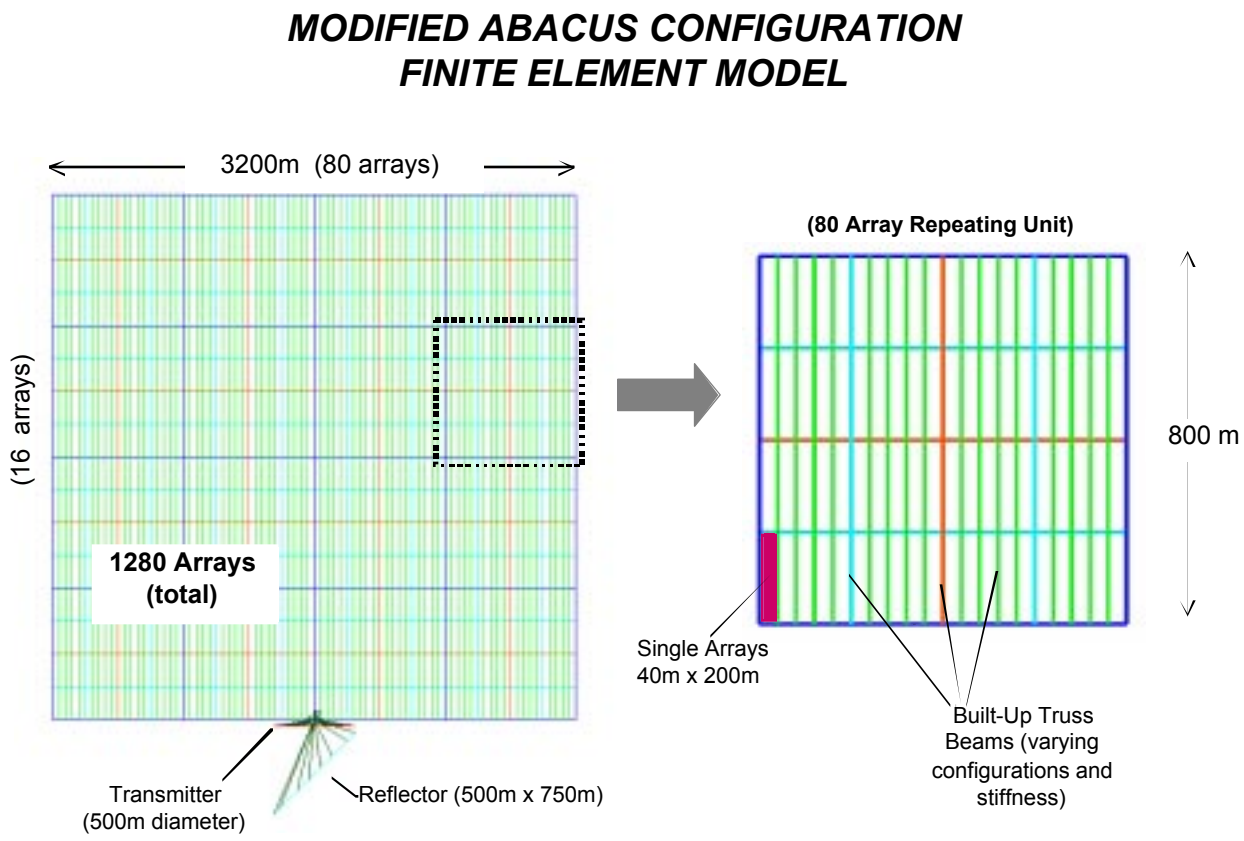

Figure 2.13: Baseline Abacus finite element model (Courtesy of Tim Collins at NASA LaRC).

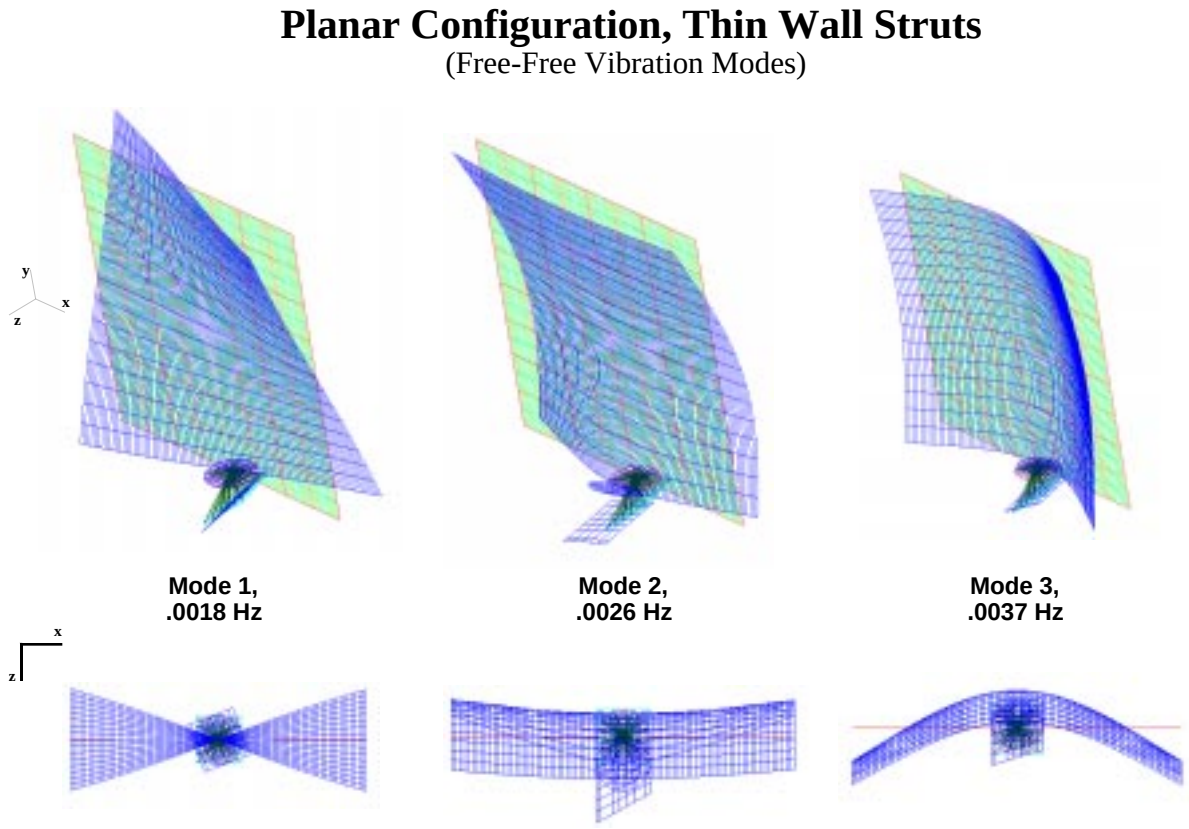

Figure 2.14: Baseline Abacus vibration modes (Courtesy of Tim Collins at NASA LaRC).

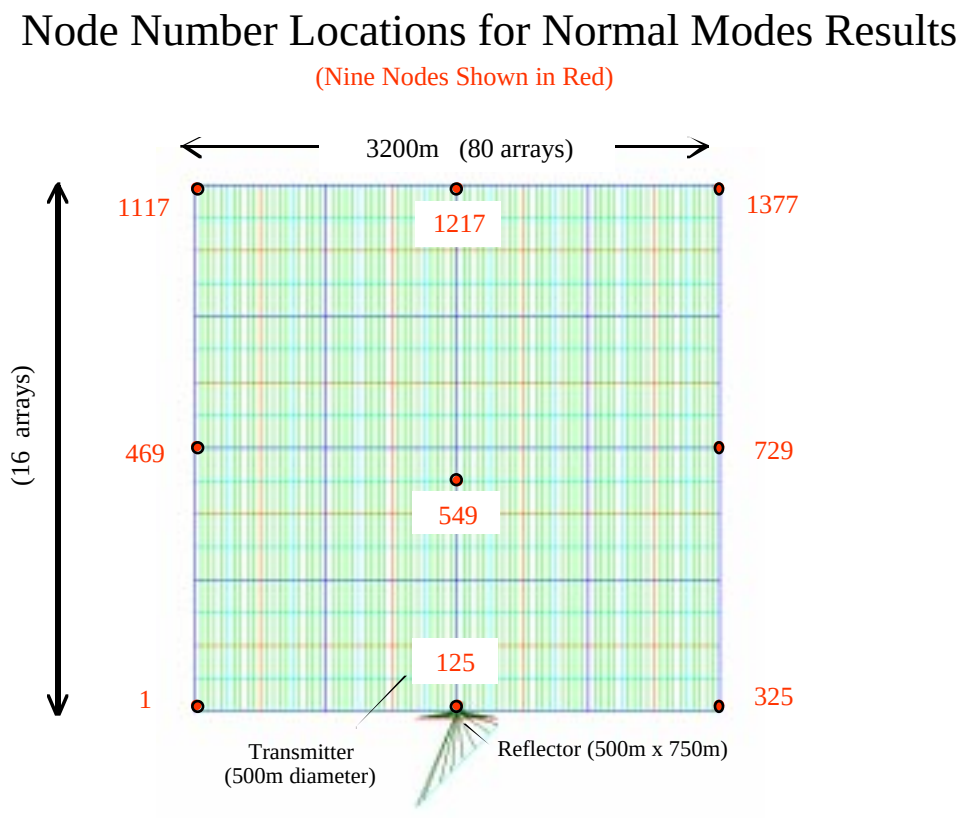

Figure 2.15: Selected FEM node locations for control analysis and design (Courtesy of Tim Collins at NASA LaRC).

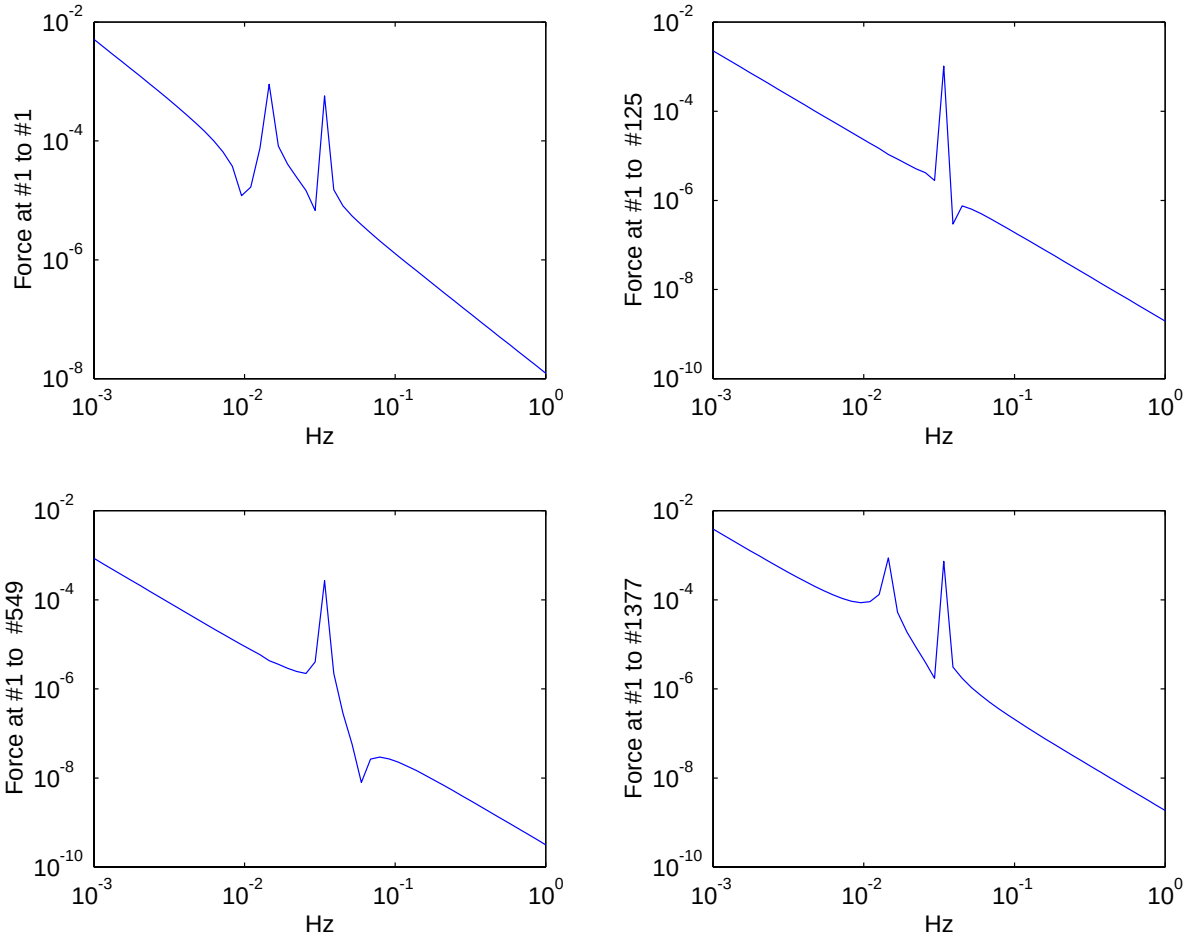

Figure 2.16: Bode magnitude plots of reduced-order transfer functions from an input force at node #1 to various output locations.

Chapter 3

Development of Abacus Control Systems Architecture

3.1 Introduction to Control Systems Design

This section provides a summary of the basic definitions and fundamentals in control systems design. It also provides the necessary background material for developing a control systems architecture for the Abacus satellite. Further detailed discussions of classical and modern control theory as applied to spacecraft control systems design can be found in Wie [17].

3.1.1 Feedback Control Systems

Block diagram representations of a feedback control system are shown in Figure 3.1. Figure 3.1(a) is called a functional block diagram representation. Any physical system to be controlled is often called a *plant*. A set of differential or difference equations used to describe a physical system is called a *mathematical model* of the system. In the analysis and design of a feedback control system, we often deal with a mathematical model of the plant, not with the actual physical plant. Consequently, special care must be taken about uncertainties in the mathematical model because no mathematical model of a physical system is exact.

A closed-loop feedback control system maintains a specified relationship between the actual output and the desired output (or the reference input) by using the difference of these, called the *error signal*. A control system in which the output has no effect on the control decision is called an *open-loop* control system. In a feedback control system, a *controller*, also called *compensator* or *control logic*, is to be designed to manipulate or process the error signal in order that certain specifications be satisfied in the presence of plant disturbances and sensor noise. In the *analysis* of control systems, we analyze the dynamical behavior or characteristics of the system under consideration. In the *design* or *synthesis*, we are concerned with designing a feedback control system so that

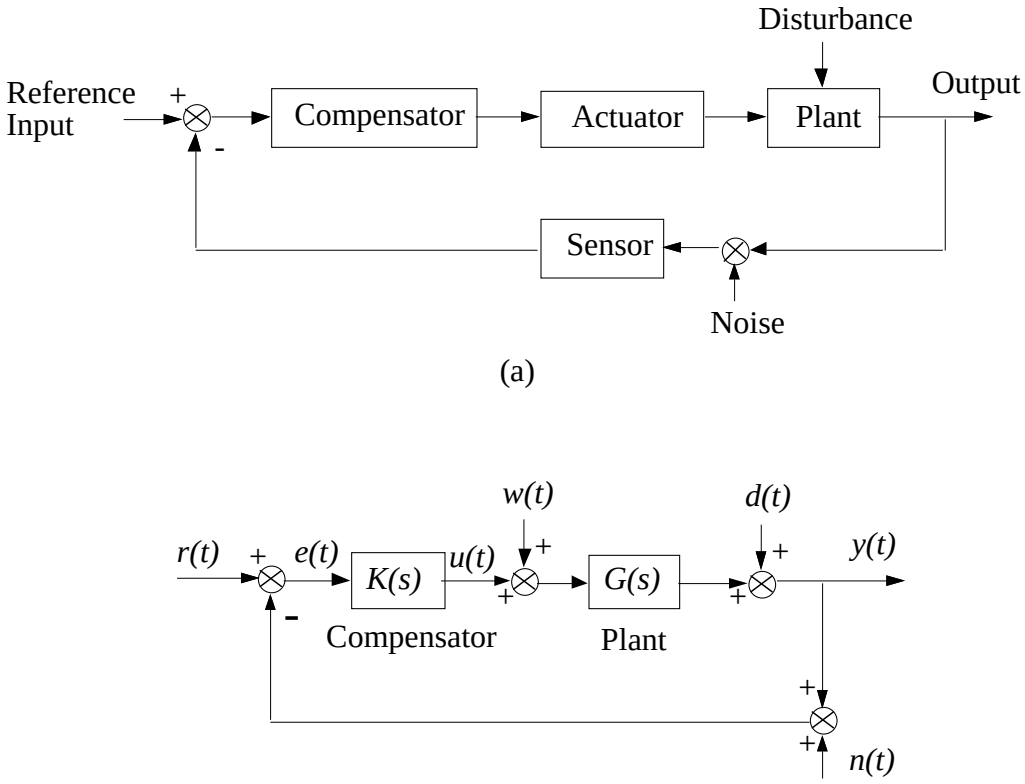

Figure 3.1: Block diagram representations of a feedback control system.

it achieves the desired system characteristics.

A feedback control system can also be represented as in Figure 3.1(b) using transfer functions. In this figure, for simplicity, the actuator and sensor dynamics are neglected, and $r(t)$ denotes the reference input, $y(t)$ the plant output, $G(s)$ the plant transfer function, $K(s)$ the compensator, $u(t)$ the control input, $e(t)$ the error signal, $w(t)$ the disturbance, $d(t)$ the output disturbance, and $n(t)$ a sensor noise.

The output of this closed-loop system, neglecting the sensor noise $n(t)$, can then be represented as

$$y(s) = \frac{K(s)G(s)}{1 + K(s)G(s)} r(s) + \frac{G(s)}{1 + K(s)G(s)} w(s) + \frac{1}{1 + K(s)G(s)} d(s) \tag{1}$$

where $y(s) = \mathcal{L}[y(t)]$, $r(s) = \mathcal{L}[r(t)]$, $w(s) = \mathcal{L}[w(t)]$, and $d(s) = \mathcal{L}[d(t)]$. In particular, the closed-loop transfer functions from $d(s)$ and $r(s)$ to $y(s)$ are

$$\frac{y(s)}{d(s)} = \frac{1}{1 + K(s)G(s)} = S(s) \tag{2}$$

$$\frac{y(s)}{r(s)} = \frac{K(s)G(s)}{1 + K(s)G(s)} = T(s) \tag{3}$$

and $S(s)$ and $T(s)$ are called the *sensitivity function* and the *complementary sensitivity function*, respectively. Furthermore, we have the following relationship:

$$S(s) + T(s) = 1 \tag{4}$$

The *closed-loop characteristic equation* is defined as

$$1 + K(s)G(s) = 0 \tag{5}$$

and $K(s)G(s)$ is called the *loop transfer function*. It is also called the *open-loop transfer function* in the literature. The importance of the loop transfer function cannot be overemphasized because it is used extensively in the analysis and design of closed-loop systems. The roots of the closed-loop characteristic equation are called the *closed-loop poles*.

The error signal, ignoring the sensor noise $n(t)$, is defined as

$$e(t) = r(t) - y(t) \tag{6}$$

and the steady-state error can be found as

$$e_{ss} = \lim_{t\to\infty} e(t) = \lim_{s\to 0} se(s) \tag{7}$$

where $e(s) = \mathcal{L}[e(t)]$, provided that $e(t)$ has a final value. For the system shown in Figure 3.1, ignoring $w(s)$ and $d(s)$, we have

$$e(s) = \frac{1}{1 + K(s)G(s)} r(s) \tag{8}$$

and

$$e_{ss} = \lim_{s\to 0} \frac{sr(s)}{1 + K(s)G(s)} \tag{9}$$

Thus, it is required that

$$\lim_{s\to 0} K(s)G(s) = \infty \tag{10}$$

to have zero steady-state tracking error for a constant reference input command.

A feedback control system is often characterized by its system type. The *system type* is defined as the number of poles of the loop transfer function $K(s)G(s)$ at the origin. Therefore, a type 1 system has zero steady-state error for a constant reference input, a type 2 system has zero steady-state error for a constant or ramp reference input, and so forth.

In order to reduce the effects of the disturbance, the magnitude of the loop transfer function $K(s)G(s)$ must be large over the frequency band of the disturbance $d(t)$. For good command following at any frequency, the steady-state or D.C. gain must be large. In general, a fast transient response, good tracking accuracy, good disturbance rejection, and good sensitivity require a high loop gain over a wide band of frequencies. Because the high loop gain may degrade the overall system stability margins, proper tradeoffs between performance and stability are always necessary in practical control designs.

3.1.2 Classical Frequency-Domain Methods

Root Locus Method

One of classical control analysis and design techniques is the root locus method developed by Evans in 1950. In Evans' root locus method, the closed-loop characteristic equation is described by

$$1 + KG(s) = 0 \tag{11}$$

where $KG(s)$ denotes the loop transfer function, $G(s)$ includes both the compensator transfer function and the plant transfer function, and K is called the overall loop gain. Note that the roots of the closed-loop characteristic equation are called the closed-loop poles.

In Evans' root locus plot, the poles and zeros of the loop transfer function $KG(s)$ are shown, where the poles are represented as cross, $\times$, and zeros as circle, $\circ$. A root locus is then simply a plot of the closed-loop poles as the overall loop gain K is usually varied from 0 to ∞.

Using a root locus plot, one can easily determine a *gain margin* which is one of the most important measures of the relative stability of a feedback control system. A gain margin indicates how much the loop gain K can be increased or decreased from its chosen nominal value until the closed-loop system becomes unstable. For example, if the loop gain K can be increased by a factor of 2 until a root locus crosses the imaginary axis toward the right-half s plane, then the gain margin becomes $20 \log 2 \approx +6$ dB. In some cases of an open-loop unstable system, the closed-loop system may become unstable if the loop gain is decreased from its chosen nominal value. For example, if the gain can be decreased by a factor of 0.707 until the closed-loop system becomes unstable, then the (negative) gain margin is $20 \log 0.707 \approx -3$ dB. The root locus method also allows the designer to properly select at least some of the closed-loop pole locations and thus control the transient response characteristics.

Frequency-Response Methods

Frequency-response analysis and synthesis methods are among the most commonly used techniques for feedback control system analysis and design, and they are based on the concept of frequency-response function.

The *frequency-response function* is defined by the transfer function evaluated at $s = j\omega$; that is, the frequency response function of a transfer function $G(s)$ is given by

$$G(s)|_{s=j\omega} = G(j\omega) = \mathrm{Re}[G(j\omega)] + j\,\mathrm{Im}[G(j\omega)] = |G(j\omega)|e^{j\phi(\omega)} \tag{12}$$

where $|G(j\omega)|$ and $\phi(\omega)$ denote, respectively, the magnitude and phase of $G(j\omega)$ defined as

$$|G(j\omega)| = \sqrt{\{\mathrm{Re}[G(j\omega)]\}^2 + \{\mathrm{Im}[G(j\omega)]\}^2}$$

$$\phi(\omega) = \tan^{-1}\frac{\mathrm{Im}[G(j\omega)]}{\mathrm{Re}[G(j\omega)]}$$

For a given value of ω, $G(j\omega)$ is a complex number. Thus, the frequency-response function $G(j\omega)$ is a complex function of ω. Mathematically, the frequency response function is a mapping from the s plane to the $G(j\omega)$ plane. The upper half of the $j\omega$-axis, which is a straight line, is mapped into the complex plane via mapping $G(j\omega)$.

One common method of displaying the frequency-response function is a *polar plot* (also called a *Nyquist plot*) where the magnitude and phase angle of $G(j\omega)$, or its real and imaginary parts, are plotted in a plane as the frequency ω is varied. Another form of displaying $G(j\omega)$ is to plot the magnitude of $G(j\omega)$ versus ω and to plot the phase angle of $G(j\omega)$ versus ω. In a *Bode plot*, the magnitude and phase angle are plotted with frequency on a logarithmic scale. Also, we often plot the magnitude of the frequency-response function in decibels (dB); that is, we plot $20 \log |G(j\omega)|$. A plot of the logarithmic magnitude in dB versus the phase angle for a frequency range of interest is called a *Nichols plot*.

For a feedback control system shown in Figure 3.1, the loop transfer function, $K(s)G(s)$ evaluated at $s = j\omega$, is used extensively in the analysis and design of the system using frequency-response methods. The closed-loop frequency response functions defined as

$$\frac{y(j\omega)}{d(j\omega)} = S(j\omega) = \frac{1}{1 + K(j\omega)G(j\omega)} \tag{13}$$

$$\frac{y(j\omega)}{r(j\omega)} = T(j\omega) = \frac{K(j\omega)G(j\omega)}{1 + K(j\omega)G(j\omega)} \tag{14}$$

are also used in classical frequency-domain control systems design.

One of the most important measures of the relative stability of a feedback control system is the gain and phase margins as defined as follows.

Gain Margin. Given the loop transfer function $K(s)G(s)$ of a feedback control system, the *gain margin* is defined to be the reciprocal of the magnitude $|K(j\omega)G(j\omega)|$ at the phase-crossover frequency at which the phase angle $\phi(\omega)$ is -180 deg; that is, the gain margin, denoted by g_m, is defined as

$$g_m = \frac{1}{|K(j\omega_c)G(j\omega_c)|} \tag{15}$$

or

$$g_m = -20 \log |K(j\omega_c)G(j\omega_c)| \quad \text{dB} \tag{16}$$

where ω_c is the phase-crossover frequency. For a stable minimum-phase system, the gain margin indicates how much the gain can be increased before the closed-loop system becomes unstable.

Phase Margin. The *phase margin* is the amount of additional phase lag at the gain-crossover frequency ω_c at which $|K(j\omega_c)G(j\omega_c)| = 1$ required to make the system unstable; that is,

$$\phi_m = \phi[K(j\omega_c)G(j\omega_c)] + 180^\circ \tag{17}$$

Although the gain and phase margins may be obtained directly from a Nyquist plot, they can also be determined from a Bode plot or a Nichols plot of the loop transfer function $K(j\omega)G(j\omega)$.

3.1.3 Classical PID Control Design

The PID (proportional-integral-derivative) control logic is commonly used in most feedback controllers. To illustrate the basic concept of the PID control, consider a cart of mass m on a frictionless horizontal surface, as shown in Figure 3.2(a). This so-called double integrator plant is described by

$$m\ddot{y}(t) = u(t) + w(t) \tag{18}$$

where y is the output displacement of the cart, u is the input force acting on the cart, and w is a disturbance force. This system with a rigid-body mode is unstable, thus the system needs to be stabilized and the desired output is assumed to be zero.

Assuming that the position and velocity of the system can be directly measured, consider a direct velocity and position feedback control logic expressed as:

$$u(t) = -ky(t) - c\dot{y}(t) \tag{19}$$

or

$$u = -(k + cs)y$$

where k and c are controller gains to be determined. The closed-loop system illustrated by Figure 3.2(b) is then described by

$$m\ddot{y}(t) + c\dot{y}(t) + ky(t) = w(t)$$

which is, in fact, a mathematical representation of a mass-spring-damper system forced by an external disturbance $w(t)$, as illustrated in Figure Figure 3.2(c).

The closed-loop characteristic equation of the system shown in Figure 3.2 is

$$ms^2 + cs + k = 0$$

The control design task is to tune the "active damper" and "active spring" to meet given performance/stability specifications of the closed-loop system. Let ω_n and ζ be the desired natural frequency and damping ratio of the closed-loop poles. Then the desired closed-loop characteristic equation becomes

$$s^2 + 2\zeta\omega_n s + \omega_n^2 = 0$$

and the controller gains c and k can be determined as

$$c = 2m\zeta\omega_n \tag{20a}$$

$$k = m\omega_n^2 \tag{20b}$$

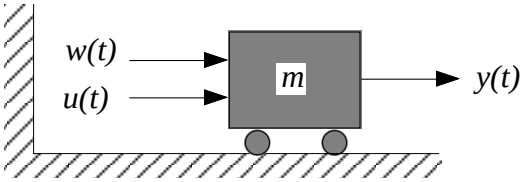

(a) Open-loop system

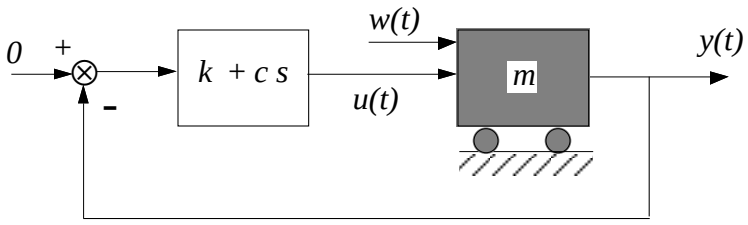

(b) Closed-loop system with position and velocity feedback

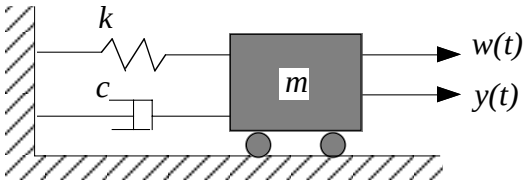

(c) Equivalent closed-loop system representation

Figure 3.2: Control of a double integrator plant by direct velocity and position feedback.

The damping ratio ζ is often selected as: $0.5 \leq \zeta \leq 0.707$, and the natural frequency ω_n is then considered as the *bandwidth* of the PD controller of a system with a rigid-body mode. For a unit-step disturbance, this closed-loop system with the PD controller results in a nonzero steady-state output $y(\infty) = 1/k$. However, the steady-state output error $y(\infty)$ can be made small by designing a high-bandwidth control system.

Consider the control problem of a double integrator plant with measurement of position only. A common method of stabilizing the double integrator plant with noisy position measurement is to employ a phase-lead compensator of the form:

$$u(s) = -K\frac{T_1 s + 1}{T_2 s + 1}\, y(s)$$

as illustrated in Figure 3.3(a). An equivalent closed-loop system can be represented using two springs and a damper as in Figure 3.3(b) and that

$$K = k_1; \qquad T_1 = \frac{c(k_1 + k_2)}{k_1 k_2}; \qquad T_2 = \frac{c}{k_2}$$

For further details of designing a passive three-parameter isolator known as the D-Strut^{TM} that can be modeled as Figure 3.3(b), see Davis, L. P., Cunningham, D., and Harrell, J., "Advanced 1.5 Hz Passive Viscous Isolation System," *Proceedings of AIAA Structures, Structural Dynamics, and Materials Conference*, AIAA, Washington, DC, April 1994.

In order to keep the cart at the desired position $y = 0$ at steady state in the presence of a constant disturbance, consider a PID controller of the form:

$$u(t) = -K_P y(t) - K_I \int y(t)dt - K_D \dot{y}(t) \tag{21}$$

or

$$u(s) = -[K_P + \frac{K_I}{s} + K_D s]\, y(s)$$

In practical analog circuit implementation of a PID controller when $\dot{y}$ is not directly measured, differentiation is always preceded by a lowpass filter to reduce noise effects. It can be shown that for a constant disturbance, the closed-loop system with the PID controller, in fact, results in a zero steady-state output $y(\infty) = 0$.

The closed-loop characteristic equation can be found as

$$ms^3 + K_D s^2 + K_P s + K_I = 0$$

and let the desired closed-loop characteristic equation be expressed as

$$(s^2 + 2\zeta\omega_n s + \omega_n^2)(s + 1/T) = 0$$

where ω_n and ζ denote, respectively, the natural frequency and damping ratio of the complex poles associated with the rigid-body mode and T is the time constant of the real pole associated with integral control.

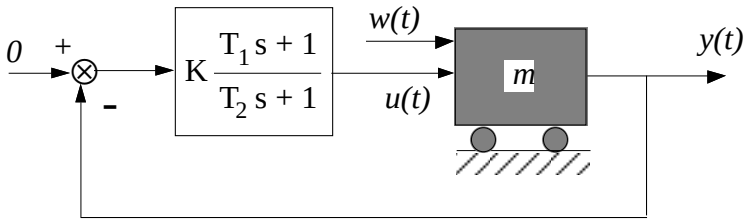

(a) Closed-loop system with a phase-lead compensator

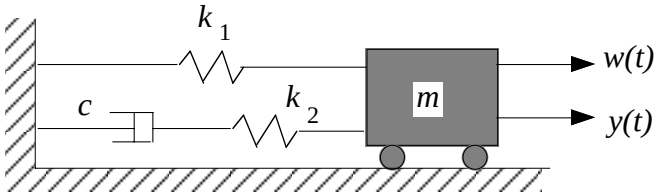

(b) Equivalent closed-loop system representation using springs and a damper

Figure 3.3: Control of a double integrator plant using a phase-lead compensator.

The PID controller gains can then be determined as

$$K_P = m(\omega_n^2 + \frac{2\zeta\omega_n}{T}) \tag{22a}$$

$$K_I = m\frac{\omega_n^2}{T} \tag{22b}$$

$$K_D = m(2\zeta\omega_n + \frac{1}{T}) \tag{22c}$$

The time constant T of integral control is often selected as

$$T \approx \frac{10}{\zeta\omega_n}$$

3.1.4 Digital PID Controller

Consider a continuous-time PID controller represented as

$$u(t) = -K_P y(t) - K_I \int y(t)dt - K_D \dot{y}(t)$$

Using Euler's approximation of differentiation:

$$s \approx \frac{1 - z^{-1}}{T} = \frac{z - 1}{Tz} \tag{23}$$

we obtain an equivalent digital PID controller represented in z-domain transfer function form as:

$$u = -\left\{ K_P + K_I \frac{T}{1 - z^{-1}} + K_D \frac{1 - z^{-1}}{T} \right\} y \tag{24}$$

This digital PID control logic can be implemented in a computer as follows:

$$u(k) = -K_P y(k) - K_I \hat{u}(k) - K_D \frac{y(k) - y(k-1)}{T} \tag{25}$$

where

$$\hat{u}(k) = \hat{u}(k-1) + Ty(k)$$

A single-axis block diagram representation of a digital control system of the Hubble Space Telescope is shown in Figure 3.4. As can be seen in this figure, the baseline digital control system of the Hubble Space Telescope, with a sampling period $T = 0.025$ sec and a computational delay of $T_d = 0.008$ sec, is in fact a digital PID controller with a finite impulse response (FIR) filter in the rate loop.

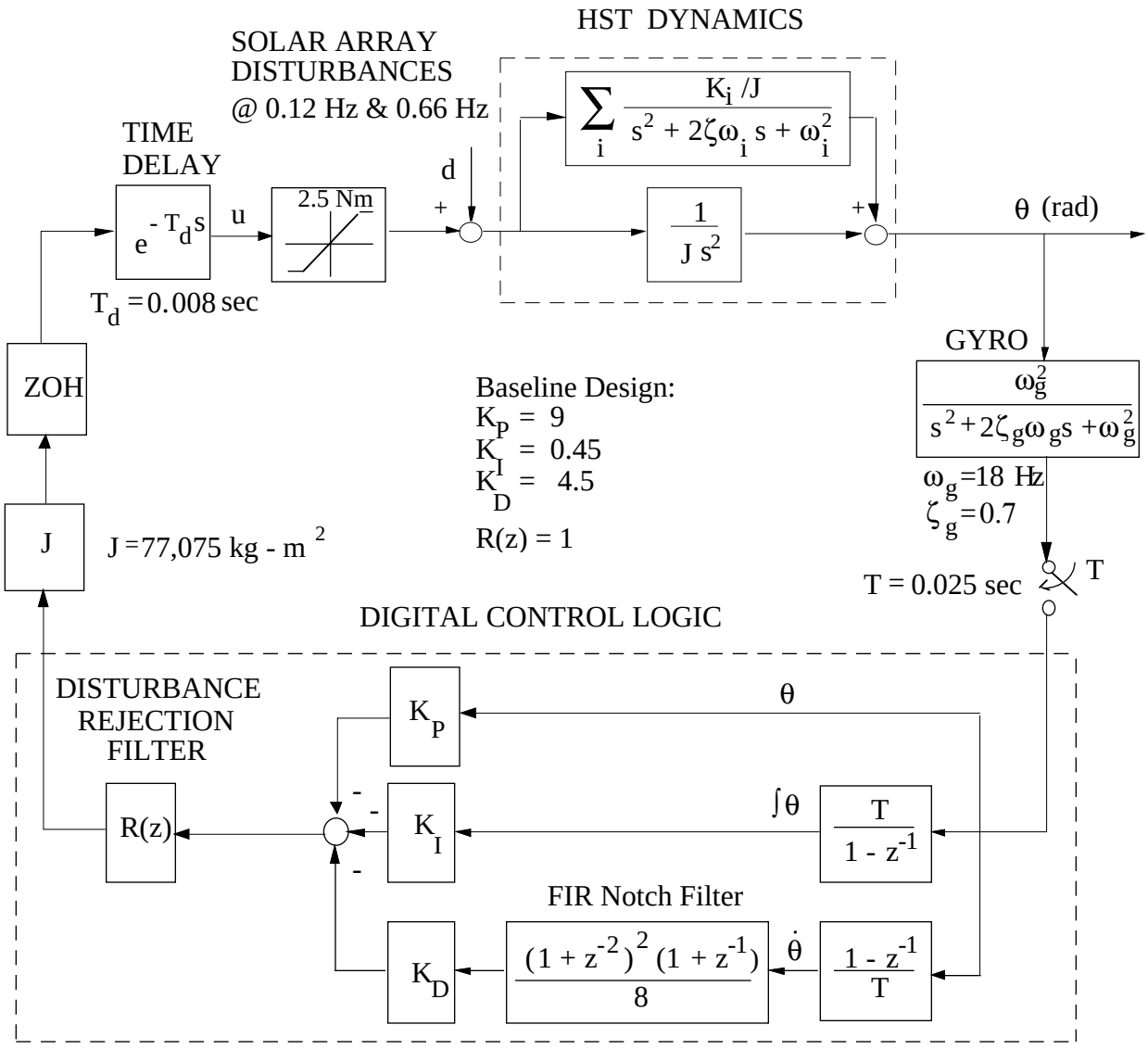

Figure 3.4: Simplified block diagram of the pitch-axis pointing control system of the Hubble Space Telescope [17], [28].

3.1.5 Classical Gain-Phase Stabilization

In the preceding sections, we have introduced the fundamentals of classical control. In this section, we present a classical gain-phase stabilization approach to compensator design, in particular, for a flexible spacecraft which has a rigid-body mode and lightly damped, oscillatory flexible modes. The approach allows the control designer to properly gain-phase stabilize each mode, one-by-one, resulting in a meaningful control design with physical insight. The classical gain-phase stabilization method is primarily restricted to the single-input single-output control problems, however.

The classical concepts of gain-phase stabilization of a rigid-body and flexible modes can be summarized briefly as follows:

1) *Gain stabilization* of a flexible mode provides attenuation of the control loop gain at the desired frequency to ensure stability regardless of the control loop phase uncertainty. A lightly damped, flexible mode is said to be *gain stabilized* if it is closed-loop stable for the selected loop gain, but it becomes unstable if the loop gain is raised or its passive damping reduced. Hence, a gain stabilized mode has a finite gain margin, but is closed-loop stable regardless of the phase uncertainty.

2) *Phase stabilization* of a flexible mode provides the proper phase characteristics at the desired frequency to obtain a closed-loop damping that is greater than the passive damping of the mode. A lightly damped, flexible mode is said to be *phase stabilized* if it is closed-loop stable for arbitrarily small passive damping. Hence, a phase stabilized mode has a finite phase margin, but is closed-loop stable regardless of the loop gain uncertainty.

3) A rigid-body or flexible mode is said to be *gain-phase stabilized* if it is closed-loop stable with finite gain and phase margins.

When an actuator and a sensor are "colocated" on flexible structures in space, the rigid-body mode and all the flexible modes are said to be "stably interacting" with each other. For such a colocated case, position feedback with a phase-lead compensator or direct rate and position feedback can be used to stabilize all the flexible and rigid-body modes. Because all the modes are phase stabilized in this case, special care must be taken about the phase uncertainty from the control loop time delay and actuator/sensor dynamics. As frequency increases, the phase lag due to a time delay will eventually exceed the maximum phase lead of 90 degrees from the direct rate feedback. Thus, roll-off filtering (i.e., gain stabilization) of high-frequency modes is often needed to attenuate the control loop gain at frequencies above the control bandwidth. The selection of roll-off filter corner frequency depends on many factors. When a colocated actuator/sensor pair is used, the corner frequency is often selected between the primary flexible modes and the secondary flexible modes. An attempt to gain stabilize all the flexible modes should be avoided, unless the spacecraft or structures are nearly rigid. In practice, the actual phase uncertainty of the control loop must be taken into account for the proper tradeoff between phase stabilization and gain stabilization.

When an actuator and a sensor are not colocated, the rigid body mode and some of the flexible modes are said to be "unstably interacting" with each other. Unless gain stabilization of all the flexible modes is possible for a low-bandwidth control, a proper combination of gain-phase stabilization is unavoidable. Gain stabilization of an unstably interacting flexible mode can be achieved only if that mode has a certain amount of passive damping. The larger the passive damping at a particular mode, the more conveniently it can be gain stabilized. Usually, gain stabilization is applied in order to stabilize high-frequency modes that have no significant effects on the overall performance. In practice, a structure has always a certain amount of passive damping, which allows for the convenient gain stabilization of such flexible modes.

Notch filtering is a conventional way of suppressing an unwanted oscillatory signal in the control loop, resulting in gain stabilization of a particular flexible mode. The use of notch filtering ensures that the specific mode is not destabilized by feedback control; however, it does not introduce any active damping, which often results in too much "ringing" that may not be acceptable in certain cases. In general, roll-off of the control loop gain at frequencies above the control bandwidth is always needed to avoid destabilizing unmodeled high-frequency modes and to attenuate high-frequency noise, and it is often simply achieved by using a double-pole lowpass filter. To sharply attenuate a signal at high frequencies while affecting the magnitude and phase of the signal at low frequencies as little as possible, various high-order lowpass filters, such as Bessel, Butterworth, Chebyshev, or elliptical filters, are also used in feedback control systems, but mostly in open-loop signal processing. The common characteristic of these conventional filters is that they are minimum-phase filters.

Although the last several decades have brought major developments in advanced control theory, the most usual approach to the design of practical control systems has been repetitive, trial-and-error synthesis using the root locus method by Evans and/or the frequency-domain methods by Bode, Nyquist, and Nichols. Classical control designs employ primarily a PID-type controller with notch and/or roll-off filtering. However, such classical control designs for a certain class of dynamical systems become difficult, especially, if a high control bandwidth is required in the presence of many closely spaced, unstably interacting, lightly damped modes with a wide range of parameter variations.

For such case, the concept of generalized second-order filtering can be employed. The concept is a natural extension of the classical notch and phase lead/lag filtering, and it is based on various pole-zero patterns that can be realized from a second-order filter of the form

$$\frac{s^2/\omega_z^2 + 2\zeta_z s/\omega_z + 1}{s^2/\omega_p^2 + 2\zeta_p s/\omega_p + 1} \tag{26}$$

where ω_z, ζ_z, ω_p, and ζ_p are filter parameters to be properly selected.

For different choices of the coefficients of this second-order filter, several well-known filters such as notch, bandpass, lowpass, highpass, phase-lead, and phase-lag filters can be realized. In addition to these minimum-phase filters, various nonminimum-phase filters can also be realized from this second-order filter [17].

3.1.6 Persistent Disturbance Rejection

A classical approach to disturbance accommodating control of dynamical systems in the presence of persistent or quasi-periodic disturbances is presented here. The method exploits the so-called *internal model principle* for asymptotic disturbance rejection. The concept of a disturbance rejection dipole is introduced from a classical control viewpoint.

After successful stabilization of the rigid-body mode as well as any other unstably interacting flexible modes, active disturbance rejection is then simply achieved by introducing into the feedback loop a model of the disturbance. A block diagram representation of a persistent disturbance rejection control system is shown in Figure 3.5.

It is assumed that a persistent (or quasi-periodic) disturbance is represented as

$$w(t) = \sum_{i=1}^{n} A_i \sin(2\pi f_i t + \phi_i)$$

with unknown magnitudes A_i and phases ϕ_i but known frequencies f_i. Note that if, for example, $f_1 = 2f_2 = \cdots = nf_n$, then $w(t)$ becomes a periodic disturbance.

In general, the disturbance $w(t)$ can be described by a Laplace transformation

$$w(s) = \frac{N_w(s)}{D_w(s)}$$

where $N_w(s)$ is arbitrary as long as $w(s)$ remains proper. The roots of $D_w(s)$ correspond to the frequencies at which the persistent excitation takes place. The inclusion of the disturbance model $1/D_w$ inside the control loop is often referred to as the internal modeling of the disturbance. In classical design, the internal disturbance model is regarded as being part of the compensator as shown in Figure 3.5. The presence of $1/D_w$ in the control loop results in the effective cancellation of the poles of $w(s)$, provided that no root of $D_w(s)$ is a zero of the plant transfer function. This is shown in the following closed-loop transfer function:

$$\begin{aligned} y(s) &= \frac{1/D(s)}{1 + N_c(s)N(s)/D_c(s)D_w(s)D(s)} w(s) \\ &= \frac{D_c(s)D_w(s)}{D_w(s)D_c(s)D(s) + N_c(s)N(s)} \frac{N_w(s)}{D_w(s)} \end{aligned} \tag{27}$$

where we can see the cancellation of $D_w(s)$.

The compensator can be viewed as a series of individual first-order or second-order filters as follows:

$$\frac{N_c(s)}{D_c(s)} = \prod_i \frac{N_{c_i}(s)}{D_{c_i}(s)}$$

Each filter is designed to perform a specific task, like the stabilization of a particular mode. In the same manner, a disturbance rejection filter can be designed that has a

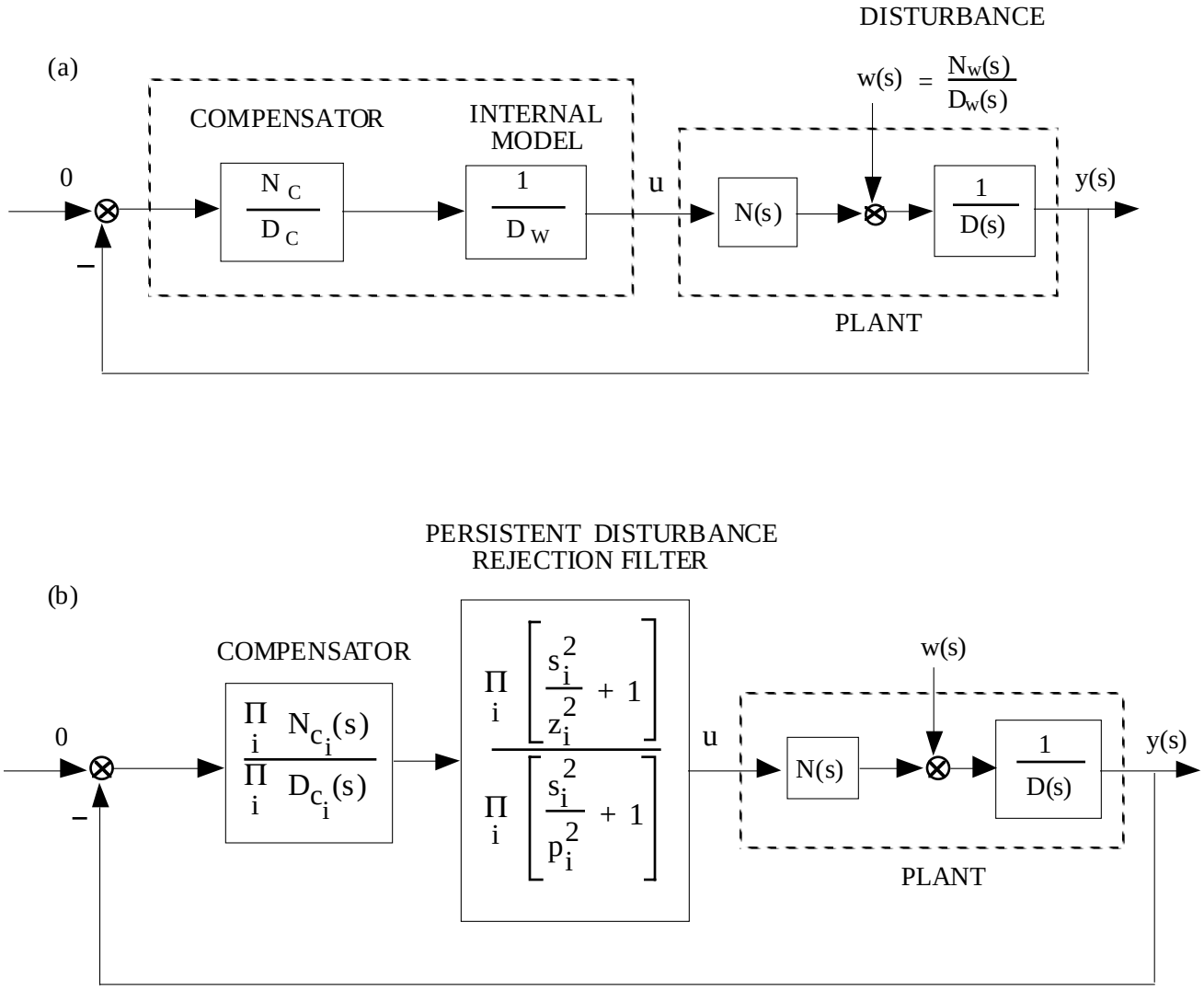

Figure 3.5: Persistent disturbance rejection control system (transfer function description).

proper transfer function and uses the internal disturbance model $1/D_w$. Thus a proper numerator is chosen in the compensator to go with the disturbance model as shown in Figure 3.5. The numerator is chosen to be of the same order as D_w so that there is a zero for each pole of the disturbance model $1/D_w$.

Although the asymptotic disturbance rejection based on the internal model principle has been well known, an interesting interpretation of the concept from a classical control viewpoint is presented here. Each pole-zero combination of the disturbance rejection filter

$$\prod_i \frac{s^2/{\omega_{z_i}}^2 + 2\zeta_{z_i} s/\omega_{z_i} + 1}{s^2/{\omega_{p_i}}^2 + 1}$$

can be called a *dipole*, where ζ_{z_i} is included for generality. The filter thus consists of as many dipoles as there are frequency components in the persistent disturbance. The separation between the zero and the pole is generally referred to as the strength of the dipole. The strength of the dipole affects the settling time of the closed-loop system; in general, the larger the separation between the pole and zero of the filter the shorter the settling time is. This is caused by the position of the closed-loop eigenvalue corresponding to the filter dipole. As the strength of the dipole is increased, this eigenvalue is pushed farther to the left, speeding up the response time of the disturbance rejection. However, this separation influences the gain-phase characteristics of the system, because the dipole causes a certain amount of gain-phase changes in its neighborhood. Moreover, at frequencies higher than the dipole there is a net gain increase or reduction. The magnitude of this gain increases with the separation between pole and zero. Therefore, as the strength of the dipole is changed to meet a chosen settling time the compensation must be readjusted. A compromise has to be reached often between the settling time and the stability of the compensated system.

The internal model principle for persistent disturbance rejection is now incorporated with the standard state-space control design problem. Active disturbance rejection for the measured output $\mathbf{y}$ is to be achieved by introducing a model of the disturbance inside the control loop, therefore using again the concept of internal modeling, as illustrated in Figure 3.6.

For example, consider a scalar disturbance $d(t)$ with one or more frequency components represented as

$$d(t) = \sum_i A_i \sin(\omega_i t + \phi_i)$$

with unknown magnitudes A_i and phases ϕ_i but known frequencies ω_i. The disturbance rejection filter is then described by

$$\dot{\mathbf{x}}_d = \mathbf{A}_d \mathbf{x}_d + \mathbf{B}_d \mathbf{y} \tag{28}$$

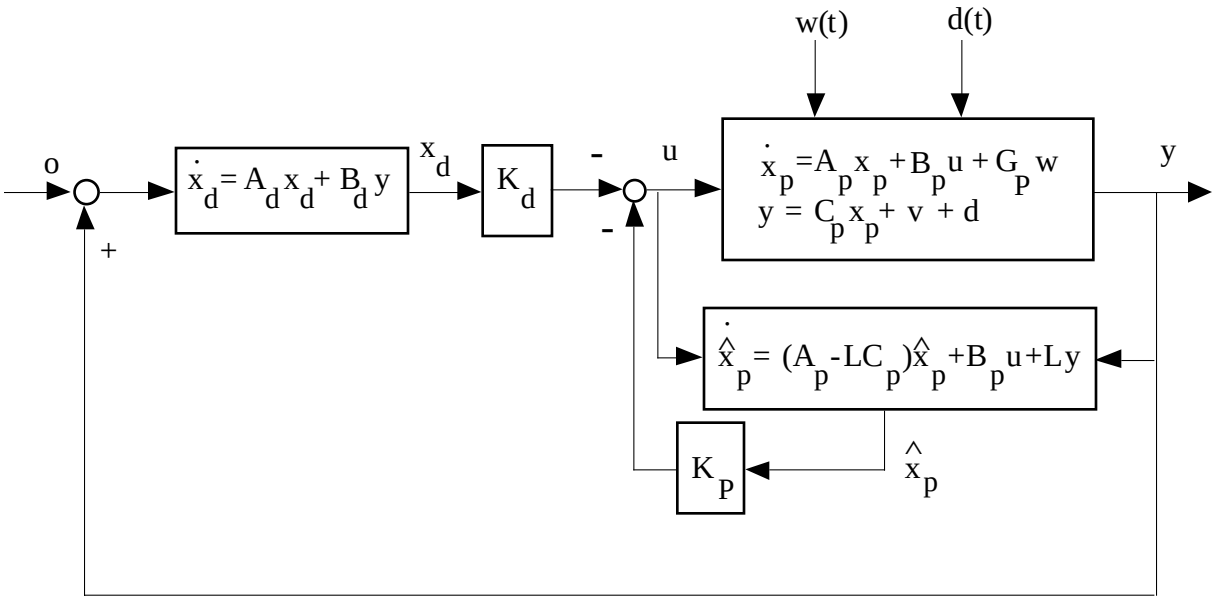

Figure 3.6: Persistent disturbance rejection control system (state-space description).

where $\mathbf{x}_d$ is the state vector introduced by the disturbance model and, for example,

$$\mathbf{A}_d = \begin{bmatrix} 0 & 1 & 0 & 0 \\ -\omega_1^2 & 0 & 0 & 0 \\ 0 & 0 & 0 & 1 \\ 0 & 0 & -\omega_2^2 & 0 \end{bmatrix} \; ; \; \mathbf{B}_d = \begin{bmatrix} 0 \\ 1 \\ 0 \\ 1 \end{bmatrix}$$

for a scalar output $y(t)$ with $d(t)$ of two frequency components. The disturbance rejection filter can include as many frequency components as the given disturbance, and is driven by the measured output $\mathbf{y}$ of the plant. This procedure is equivalent to the one used in the classical approach with the disturbance model now consisting of a state-space model.

We now consider a plant described by the state-space equation:

$$\dot{\mathbf{x}}_p = \mathbf{A}_p \mathbf{x}_p + \mathbf{B}_p \mathbf{u} + \mathbf{G}_p \mathbf{w} \tag{29a}$$

$$\mathbf{y} = \mathbf{C}_p \mathbf{x}_p + \mathbf{v} + \mathbf{d} \tag{29b}$$

where $\mathbf{x}_p$ denotes the plant's state vector, $\mathbf{u}$ the control input vector, $\mathbf{w}$ the process noise, $\mathbf{v}$ the measurement noise, and $\mathbf{d}$ the output equivalent persistent disturbance. Both $\mathbf{w}$ and $\mathbf{v}$ are assumed to be white noise processes with

$$E[\mathbf{w}(t)\mathbf{w}^T(\tau)] = \mathbf{W}\delta(t-\tau)$$
$$E[\mathbf{v}(t)\mathbf{v}^T(\tau)] = \mathbf{V}\delta(t-\tau)$$

where $\mathbf{W}$ and $\mathbf{V}$ are the corresponding spectral density matrices.

In general, a compensator designed for this plant will consist of a regulator and an estimator which will approximate the states $\mathbf{x}_p$ with estimated states $\hat{\mathbf{x}}_p$ using the information from the measured output $\mathbf{y}$. The estimator which attempts to asymptotically reduce the error term $\mathbf{e} = \mathbf{x}_p - \hat{\mathbf{x}}_p$ is given by

$$\begin{aligned}\dot{\hat{\mathbf{x}}}_p &= \mathbf{A}_p\hat{\mathbf{x}}_p + \mathbf{B}_p\mathbf{u} + \mathbf{L}(\mathbf{y} - \mathbf{C}_p\hat{\mathbf{x}}_p) \\ &= (\mathbf{A}_p - \mathbf{L}\mathbf{C}_p)\hat{\mathbf{x}}_p + \mathbf{B}_p\mathbf{u} + \mathbf{L}\mathbf{y}\end{aligned} \tag{30}$$

where the term $(\mathbf{y} - \mathbf{C}_p\hat{\mathbf{x}}_p)$ represents the error between the output of the plant and the estimated output and $\mathbf{L}$ is the estimator gain matrix to be determined.

The disturbance filter model described by Eq. (28) is then augmented to a plant described by Eq. (29) as follows:

$$\dot{\mathbf{x}} = \mathbf{A}\mathbf{x} + \mathbf{B}\mathbf{u} + \mathbf{G}\mathbf{w} \tag{31a}$$

$$\mathbf{y} = \mathbf{C}\mathbf{x} + \mathbf{v} + \mathbf{d} \tag{31b}$$

where

$$\mathbf{x} = \begin{bmatrix} \mathbf{x}_p \\ \mathbf{x}_d \end{bmatrix} \;;\; \mathbf{A} = \begin{bmatrix} \mathbf{A}_p & 0 \\ \mathbf{B}_d\mathbf{C}_p & \mathbf{A}_d \end{bmatrix} \;;\; \mathbf{B} = \begin{bmatrix} \mathbf{B}_p \\ 0 \end{bmatrix}$$

$$\mathbf{C} = \begin{bmatrix} \mathbf{C}_p & 0 \end{bmatrix} \;;\; \mathbf{G} = \begin{bmatrix} \mathbf{G}_p \\ 0 \end{bmatrix}$$

An estimated state feedback controller is then given as

$$\mathbf{u} = -\mathbf{K}\hat{\mathbf{x}}$$

where $\hat{\mathbf{x}} = \begin{bmatrix} \hat{\mathbf{x}}_p^T & \hat{\mathbf{x}}_d^T \end{bmatrix}^T$ and the gain matrix $\mathbf{K} = \begin{bmatrix} \mathbf{K}_p & \mathbf{K}_d \end{bmatrix}$ is to be determined for the augmented system described by Eq. (31).

As shown in Figure 3.6, however, $\mathbf{x}_d$ can be directly fed back as:

$$\mathbf{u} = -\begin{bmatrix} \mathbf{K}_p & \mathbf{K}_d \end{bmatrix} \begin{bmatrix} \hat{\mathbf{x}}_p \\ \mathbf{x}_d \end{bmatrix} \tag{32}$$

since $\mathbf{x}_d$ is directly available from Eq. (28).

An active disturbance rejection controller in state-space form is then given by

$$\begin{bmatrix} \dot{\hat{\mathbf{x}}}_p \\ \dot{\mathbf{x}}_d \end{bmatrix} = \begin{bmatrix} \mathbf{A}_p - \mathbf{B}_p\mathbf{K}_p - \mathbf{L}\mathbf{C}_p & -\mathbf{B}_p\mathbf{K}_d \\ 0 & \mathbf{A}_d \end{bmatrix} \begin{bmatrix} \hat{\mathbf{x}}_p \\ \mathbf{x}_d \end{bmatrix} + \begin{bmatrix} \mathbf{L} \\ \mathbf{B}_d \end{bmatrix} \mathbf{y} \tag{33}$$

$$\mathbf{u} = -\begin{bmatrix} \mathbf{K}_p & \mathbf{K}_d \end{bmatrix} \begin{bmatrix} \hat{\mathbf{x}}_p \\ \mathbf{x}_d \end{bmatrix} \tag{34}$$

And the closed-loop system with $\mathbf{w} = \mathbf{v} = \mathbf{d} = 0$ is described as

$$\begin{bmatrix} \dot{\mathbf{x}}_p \\ \dot{\hat{\mathbf{x}}}_p \\ \dot{\mathbf{x}}_d \end{bmatrix} = \begin{bmatrix} \mathbf{A}_p & -\mathbf{B}_p\mathbf{K}_p & -\mathbf{B}_p\mathbf{K}_d \\ \mathbf{L}\mathbf{C}_p & \mathbf{A}_p - \mathbf{B}_p\mathbf{K}_p - \mathbf{L}\mathbf{C}_p & -\mathbf{B}_p\mathbf{K}_d \\ \mathbf{B}_d\mathbf{C}_p & 0 & \mathbf{A}_d \end{bmatrix} \begin{bmatrix} \mathbf{x}_p \\ \hat{\mathbf{x}}_p \\ \mathbf{x}_d \end{bmatrix}$$

which can be modified using the error term, $\mathbf{e} = \mathbf{x}_p - \hat{\mathbf{x}}_p$, resulting in a partially decoupled system of equations, as follows:

$$\begin{bmatrix} \dot{\mathbf{x}}_p \\ \dot{\mathbf{x}}_d \\ \dot{\mathbf{e}} \end{bmatrix} = \begin{bmatrix} \mathbf{A}_p - \mathbf{B}_p\mathbf{K}_p & -\mathbf{B}_p\mathbf{K}_d & \mathbf{B}_p\mathbf{K}_p \\ \mathbf{B}_d\mathbf{C}_p & \mathbf{A}_d & 0 \\ 0 & 0 & \mathbf{A}_p - \mathbf{L}\mathbf{C}_p \end{bmatrix} \begin{bmatrix} \mathbf{x}_p \\ \mathbf{x}_d \\ \mathbf{e} \end{bmatrix}$$

The closed-loop characteristic equation can then be written as

$$\begin{vmatrix} s\mathbf{I} - \mathbf{A}_p + \mathbf{B}_p\mathbf{K}_p & \mathbf{B}_p\mathbf{K}_d & -\mathbf{B}_p\mathbf{K}_p \\ -\mathbf{B}_d\mathbf{C}_p & s\mathbf{I} - \mathbf{A}_d & 0 \\ 0 & 0 & s\mathbf{I} - \mathbf{A}_p + \mathbf{L}\mathbf{C}_p \end{vmatrix} = 0 \tag{35}$$

The determinant in Eq. (35) is equal to the determinants of the diagonal submatrices multiplied together, one giving the regulator eigenvalues for the augmented system including the internal model, and the other giving the estimator eigenvalues for only the plant. Hence, we have shown that the separation principle for regulator and estimator holds for a closed-loop system even with an internal model for asymptotic disturbance rejection.

3.1.7 Classical versus Modern Control Issues

State-space approaches to control design are currently emphasized in the literature and more widely explored than classical methods. This arises from the convenience of obtaining a compensator for the whole system given one set of design parameters (e.g., given weighting matrices or desired closed-loop eigenvalues). In classical design, on the other hand, a compensator must be constructed piece by piece, or mode by mode. However, both classical and state-space methods have their drawbacks as well as advantages. All these methods require, nevertheless, a certain amount of trial and error.

The question remains how to choose these parameters and what choice provides the "best" optimal design. The designer must find an acceptable set of parameters for a "good" optimal design. The use of state-space methods for control design usually results in a compensator of the same order as the system to be controlled. This means that for systems having several flexible modes, the compensator adds compensation even to modes that are stable and need no compensation. This may result in a complicated compensator design.

The classical design is particularly convenient for the control of dynamical systems with well-separated modes. The concept of nonminimum-phase compensation also provides an extremely convenient way of stabilizing unstably interacting flexible modes. The resulting compensator is usually of less order than the system to be controlled because not all flexible modes in a structure tend to be destabilized by a reduced-order controller. A helpful characteristic of most flexible space structures is their inherent passive damping. This gives the designer the opportunity of phase stabilizing significant modes and to gain stabilize all other higher frequency modes which have less influence

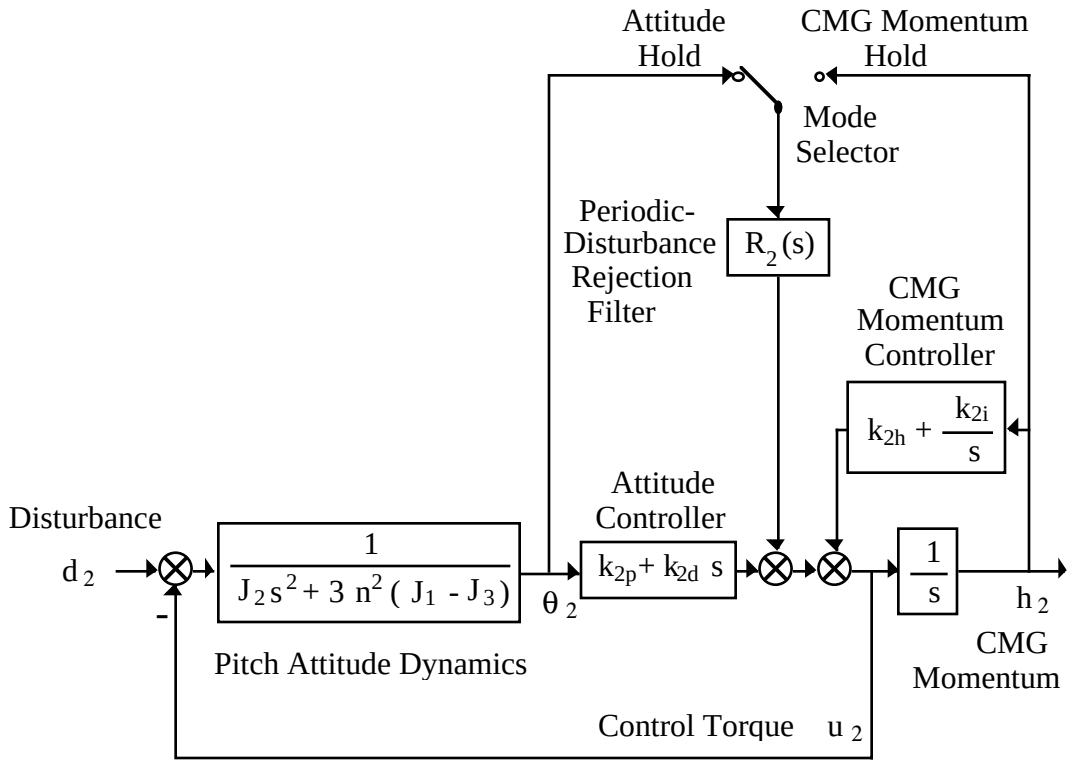

Figure 3.7: Persistent-disturbance rejection control system for the ISS.

on the structure. On the other hand, successive-mode-stabilization presents problems of its own, and a re-tuning of the compensated system becomes necessary. It is also noticed that reducing the damping in a frequency shaping filter reduces its influence on neighboring frequencies and it also reduces the phase lag at lower frequencies. However, reducing the damping of the filters increases the sensitivity of the phase stabilized modes to plant parameter uncertainties.

Active disturbance rejection can be achieved in both the classical methods and state-space methods, with the introduction of an internal model of the disturbance into the feedback loop. The concept of internal modeling of the disturbance works as well with a classical transfer function description as with a state-space description. In the classical design, the internal modeling of the disturbance leads to the introduction of a disturbance rejection dipole, or filter, for each frequency component of the disturbance. In the state-space design the introduction of the internal model results in the addition of two states for each frequency component of the disturbance.

Such a concept of persistent-disturbance rejection control has been successfully applied to the International Space Station, as illustrated in Figure 3.7. Detailed control designs using a modern state-space control technique for the ISS, the Hubble Space Telescope, and large flexible structures can be found in [28]-[33].

Table 3.1: Electric propulsion systems for the 1.2-GW Abacus satellite

Thrust, T	$\geq$ 1 N
Specific impulse, $I_{sp} = T/(\dot{m}g)$	$\geq$ 5,000 sec
Exhaust velocity, $V_e = I_{sp}g$	$\geq$ 49 km/s
Total efficiency, $\eta = P_o/P_i$	$\geq$ 80%
Power/thrust ratio, P_i/T	$\leq$ 30 kW/N
Mass/power ratio	$\leq$ 5 kg/kW
Total peak thrust	200 N
Total peak power	6 MW
Total average thrust	80 N
Total average power	2.4 MW
Number of 1-N thrusters	$\geq$ 500
Total dry mass	$\geq$ 75,000 kg
Propellant consumption	85,000 kg/year

Note: $T = \dot{m}V_e$, $P_o = \frac{1}{2}\dot{m}V_e^2 = \frac{1}{2}TV_e$, $P_o/T = \frac{1}{2}V_e$ = ideal power/thrust ratio, $P_i/T = \frac{1}{2\eta}V_e$, $I_{sp} = T/(\dot{m}g) = V_e/g$, $V_e = I_{sp}g$ where $g = 9.8$ m/s^2, $\dot{m}$ is the exhaust mass flow rate, P_i is the input power, and P_o is the output power.

3.2 Control Systems Architecture

The area-to-mass ratio of the Abacus satellite, $A/m = 0.4$ m^2/kg, relatively large when compared to 0.02 m^2/kg of typical geosynchronous communications satellites, is a key parameter characterizing the very large size of the Abacus satellite. If left uncontrolled, this can cause a cyclic drift in the longitude of the Abacus satellite of 2 deg, east and west. Thus, in addition to standard north-south and east-west stationkeeping maneuvers for $\pm$0.1 deg orbit position control, active control of the orbit eccentricity using electric thrusters with high specific impulse, I_{sp}, becomes mandatory. Furthermore, continuous sun tracking of the Abacus satellite requires large control torques to counter various disturbance torques. A control systems architecture developed in this study utilizes properly distributed electric thrusters to counter, simultaneously, the cyclic pitch gravity-gradient torque and solar radiation pressure.

Electric Propulsion Systems

Basic characteristics of electric propulsion systems for the Abacus satellite are summarized in Table 3.1.

Approximately 85,000 kg of propellant per year is required for simultaneous orbit, attitude, and structural control using 500 1-N electric propulsion thrusters with $I_{sp} =$ 5,000 sec. The yearly propellant requirement is reduced to 21,000 kg if an I_{sp} of 20,000 sec can be achieved. As I_{sp} is increased, the propellant mass decreases but the electric

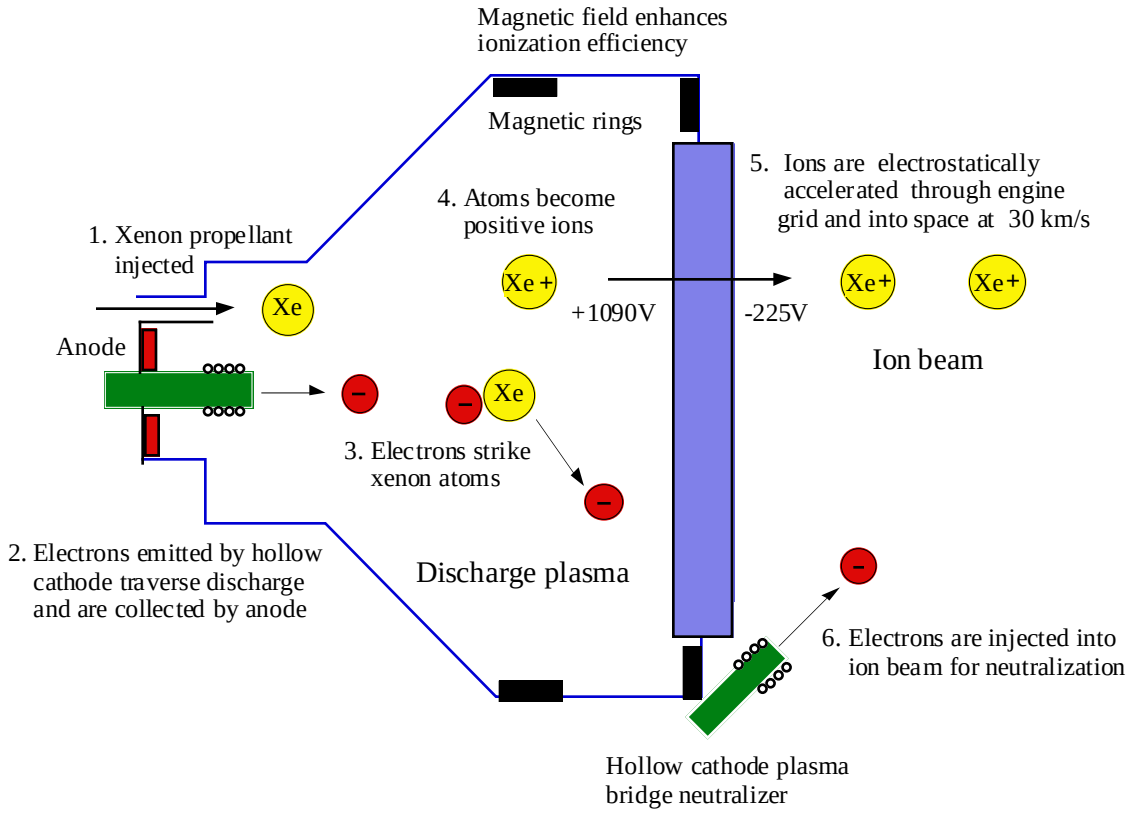

Figure 3.8: A schematic illustration of the NSTAR 2.3-kW, 30-cm diameter ion thruster on Deep Space 1 Spacecraft (92-mN maximum thrust, specific impulse ranging from 1,900 to 3,200 sec, 25 kW/N, overall efficiency of 45–65%).

power requirement increases; consequently, the mass of solar arrays and power processing units increases. Based on 500 1-N thrusters, a mass/power ratio of 5 kg/kW, and a power/thrust ratio of 30 kW/N, the total dry mass (power processing units, thrusters, tanks, feed systems, etc.) of electric propulsion systems proposed for the Abacus satellite is estimated as 75,000 kg.

A schematic illustration of the 2.3-kW, 30-cm diameter ion engine on the Deep Space 1 spacecraft is given in Figure 3.8, which is formally known as NSTAR, for NASA Solar electric propulsion Technology Application Readiness system. The maximum thrust level is about 92 mN and throttling down is achieved by feeding less electricity and xenon propellant into the propulsion system. Specific impulse ranges from 1,900 sec at the minimum throttle level to 3,200 sec.

In principle, an electric propulsion system employs electrical energy to accelerate ionized particles to extremely high velocities, giving a large total impulse for a small consumption of propellant. In contrast to standard propulsion, in which the products of chemical combustion are expelled from a rocket engine, ion propulsion is accomplished by giving a gas, such as xenon (which is like neon or helium, but heavier), an electrical

charge and electrically accelerating the ionized gas to a speed of about 30 km/s. When xenon ions are emitted at such high speed as exhaust from a spacecraft, they push the spacecraft in the opposite direction. However, the exhaust gas from an ion thruster consists of large numbers of positive and negative ions that form an essentially neutral plasma beam extending for large distances in space. It seems that little is known yet about the long-term effect of such an extensive plasma on geosynchronous satellites.

Orbit, Attitude, and Structural Control System

A control systems architecture developed in this study is shown in Figure 3.9. The proposed control systems utilize properly distributed ion thrusters to counter, simultaneously, the cyclic pitch gravity-gradient torque, the secular roll torque caused by cm-cp offset and solar pressure, the cyclic roll/yaw microwave radiation torque, and the solar pressure force whose average value is 60 N. A control-structure interaction problem of the Abacus platform with the lowest structural mode frequency of 0.002 Hz is avoided simply by designing an attitude control system with very low bandwidth ($<$ orbit frequency). However, the proposed low-bandwidth attitude control system utilizes a concept of cyclic-disturbance accommodating control to provide ± 5 arcmin pointing of the Abacus platform in the presence of large external disturbances and dynamic modeling uncertainties. High-bandwidth, colocated direct velocity feedback, active dampers may need to be properly distributed over the platform.

Placement of approximately 500 1-N electric propulsion thrusters at 12 different locations is illustrated in Figure 3.10. In contrast to a typical placement of thrusters at the four corners, e.g., employed for the 1979 SSPS reference system, the proposed placement shown in Figure 3.10 minimizes roll/pitch thruster couplings as well as the excitation of platform out-of-plane bending modes. A minimum of 500 ion engines of 1-N thrust level are required for simultaneous attitude and stationkeeping control. When reliability, lifetime, duty cycle, lower thrust level, and redundancy of ion engines are considered, this number will increase significantly.

3.3 Control System Simulation Results

Computer simulation results of a case with initial attitude errors of 10 deg in the presence various dynamic modeling uncertainties (e.g., ± 20 % uncertainties in moments and products of inertia, center-of-mass location, and principal axes, etc.), but without cyclic-disturbance rejection control, are shown in Figures 3.11–3.15. It can be seen that the pointing performance is not acceptable.

Control simulation results of a case with 10-deg initial attitude errors in the presence various dynamic modeling uncertainties (e.g., ± 20 % uncertainties for inertia, cm location, and principal axes, etc.), and with additional cyclic-disturbance rejection control, are shown in Figures 3.16–3.20. The proposed low-bandwidth attitude control system that utilizes the concept of cyclic-disturbance accommodation control satisfies the ± 5

arcmin pointing requirement of the Abacus platform in the presence of large external disturbances and dynamic modeling uncertainties. Proper roll/pitch thruster firings needed for simultaneous eccentricity and roll/pitch attitude control can be seen in Figure 3.19. Nearly linear control forces are generated by on-off modulation of individual 1-N thrusters, as can be seen in this figure. The total thrusting force from the roll/pitch thrusters #1 through #4 nearly counters the 60-N solar pressure force.

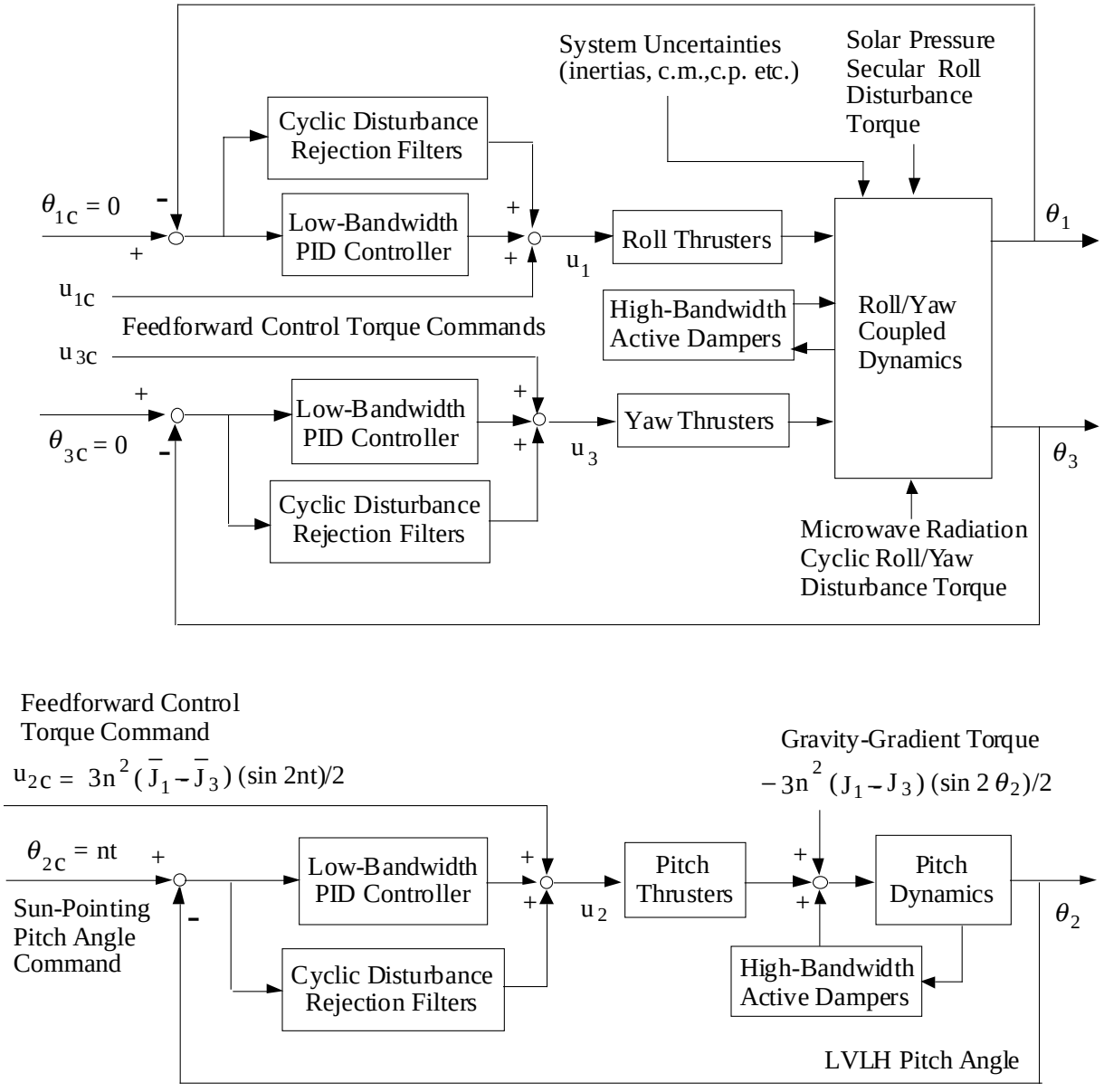

Figure 3.9: An integrated orbit, attitude, and structural control system architecture employing electric propulsion thrusters.

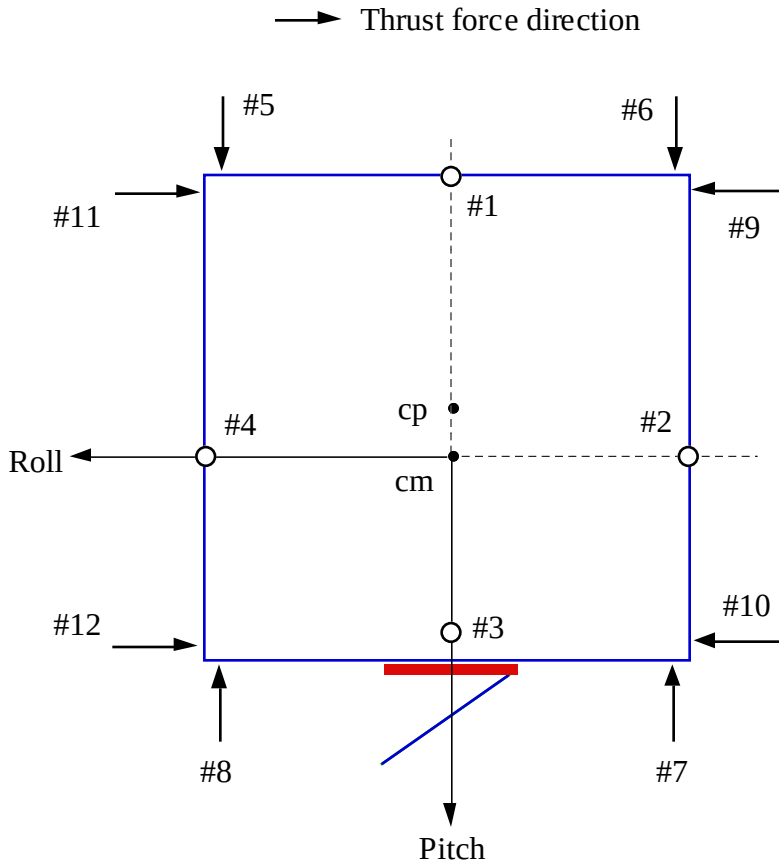

Roll: 1/3 Pitch: 2/4 Yaw: 5/6/7/8

Orbit Eccentricity, Roll/Pitch Control: 1/3, 2/4

E/W and Yaw Control: 9/10/11/12

N/S and Yaw Control: 5/6/7/8

Figure 3.10: Placement of a minimum of 500 1-N electric propulsion thrusters at 12 different locations, with 100 thrusters each at locations #2 and #4. (Note: In contrast to a typical placement of thrusters at the four corners, e.g., employed for the 1979 SSPS reference system, the proposed placement of roll/pitch thrusters at locations #1 through #4 minimizes roll/pitch thruster couplings as well as the excitation of platform out-of-plane bending modes.)

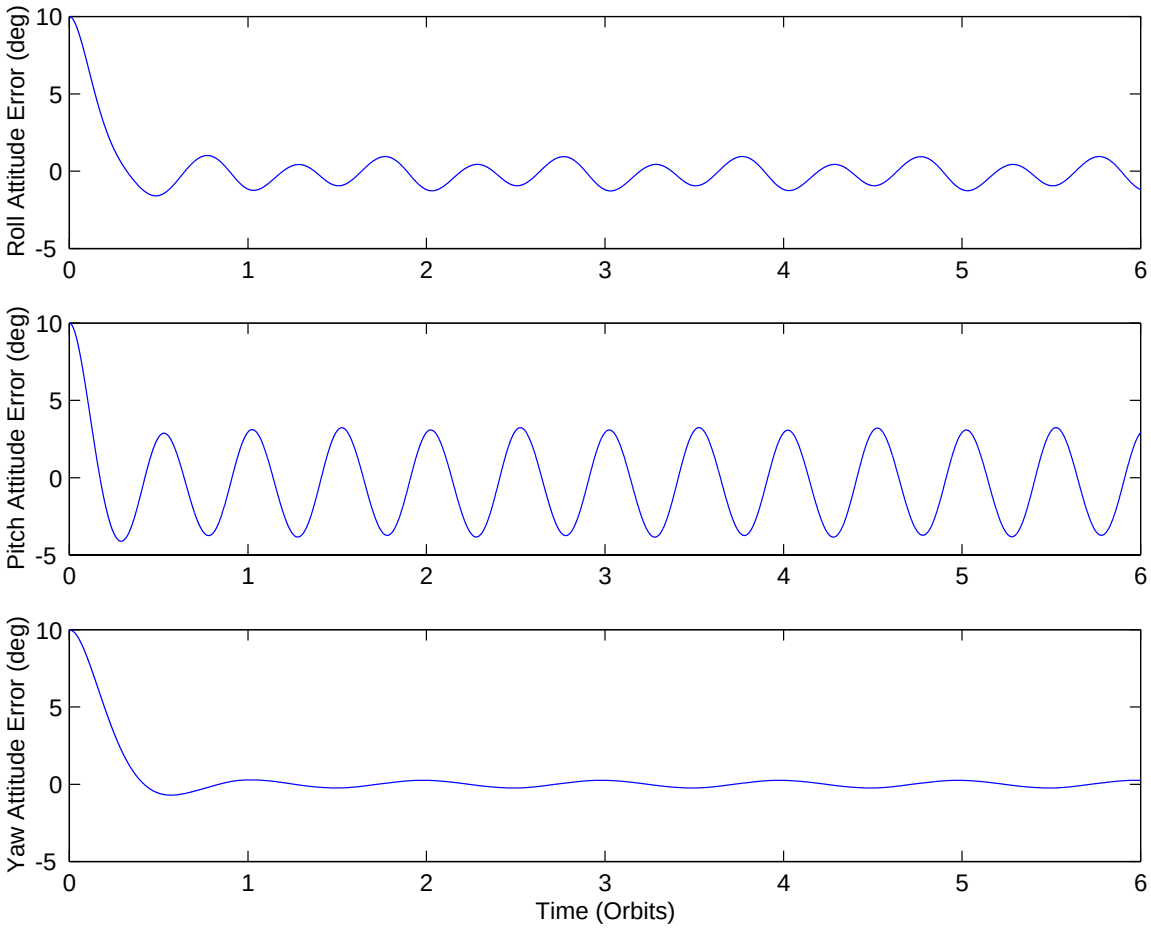

Figure 3.11: Simulation results without cyclic-disturbance rejection control.

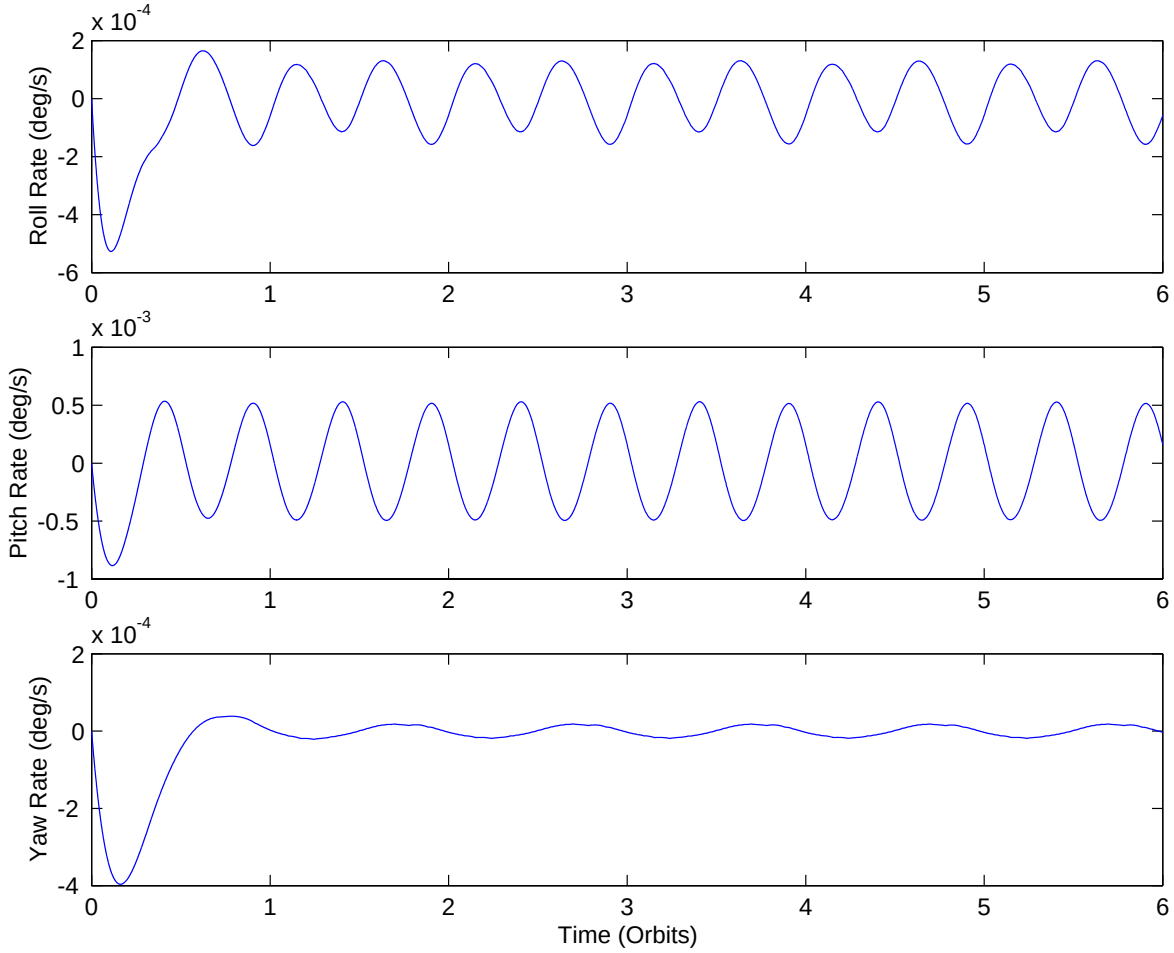

Figure 3.12: Simulation results without cyclic-disturbance rejection control (continued).

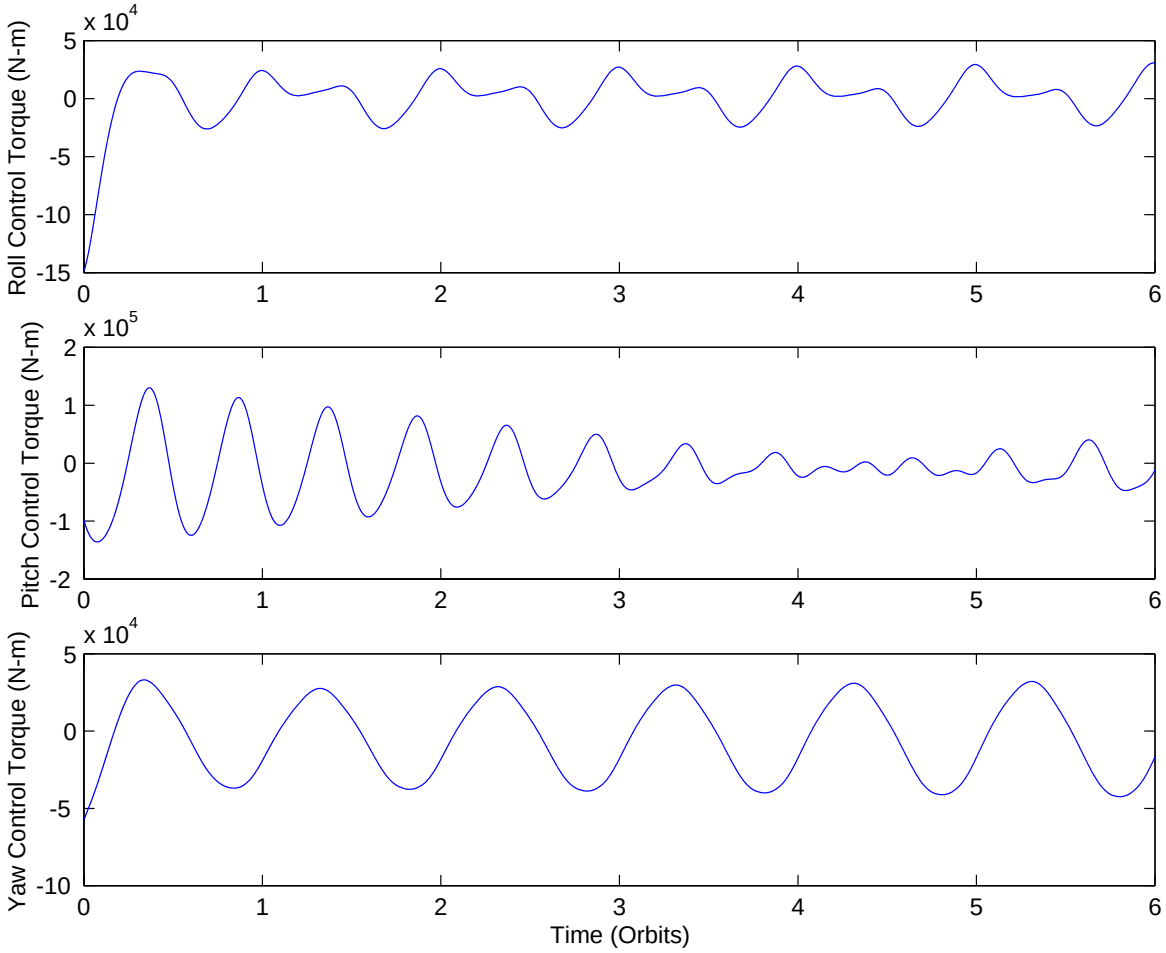

Figure 3.13: Simulation results without cyclic-disturbance rejection control (continued).

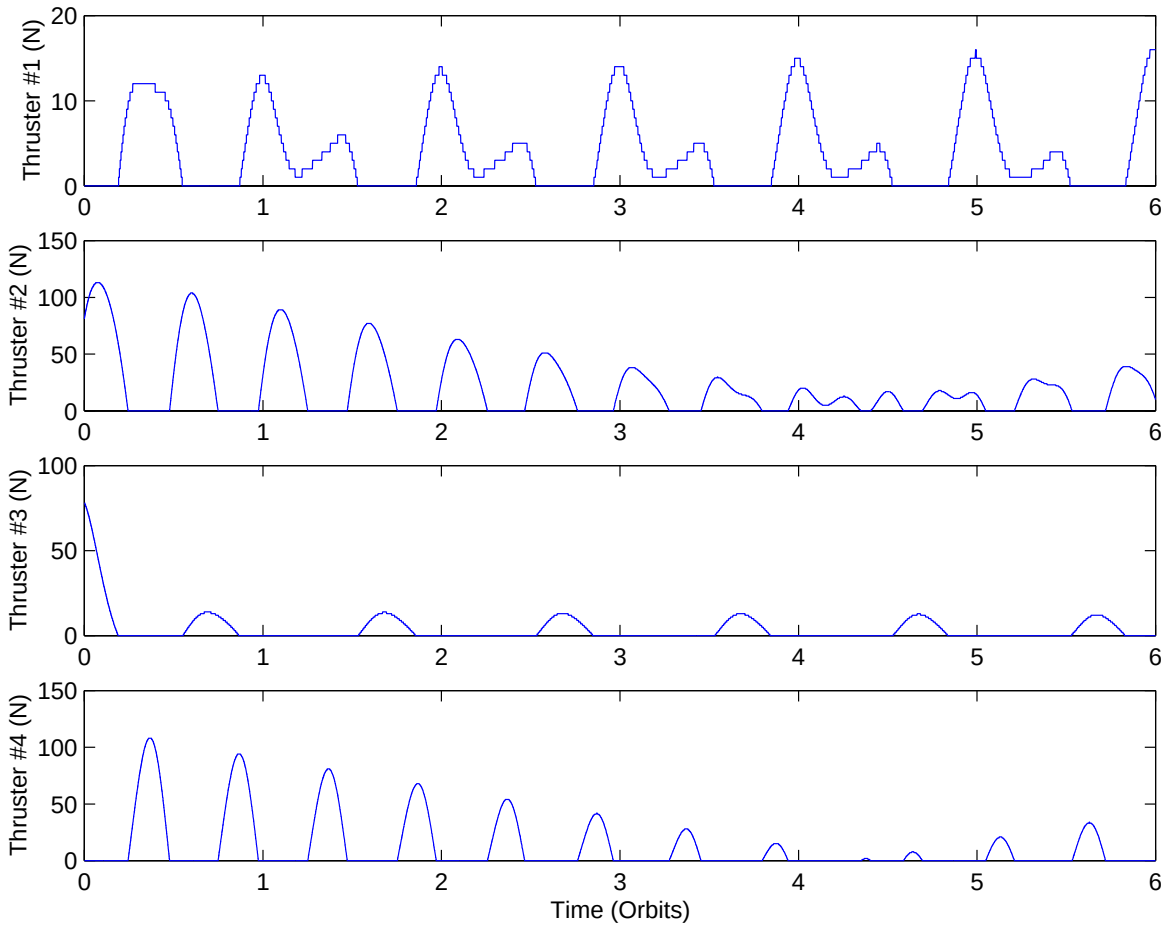

Figure 3.14: Simulation results without cyclic-disturbance rejection control (continued).

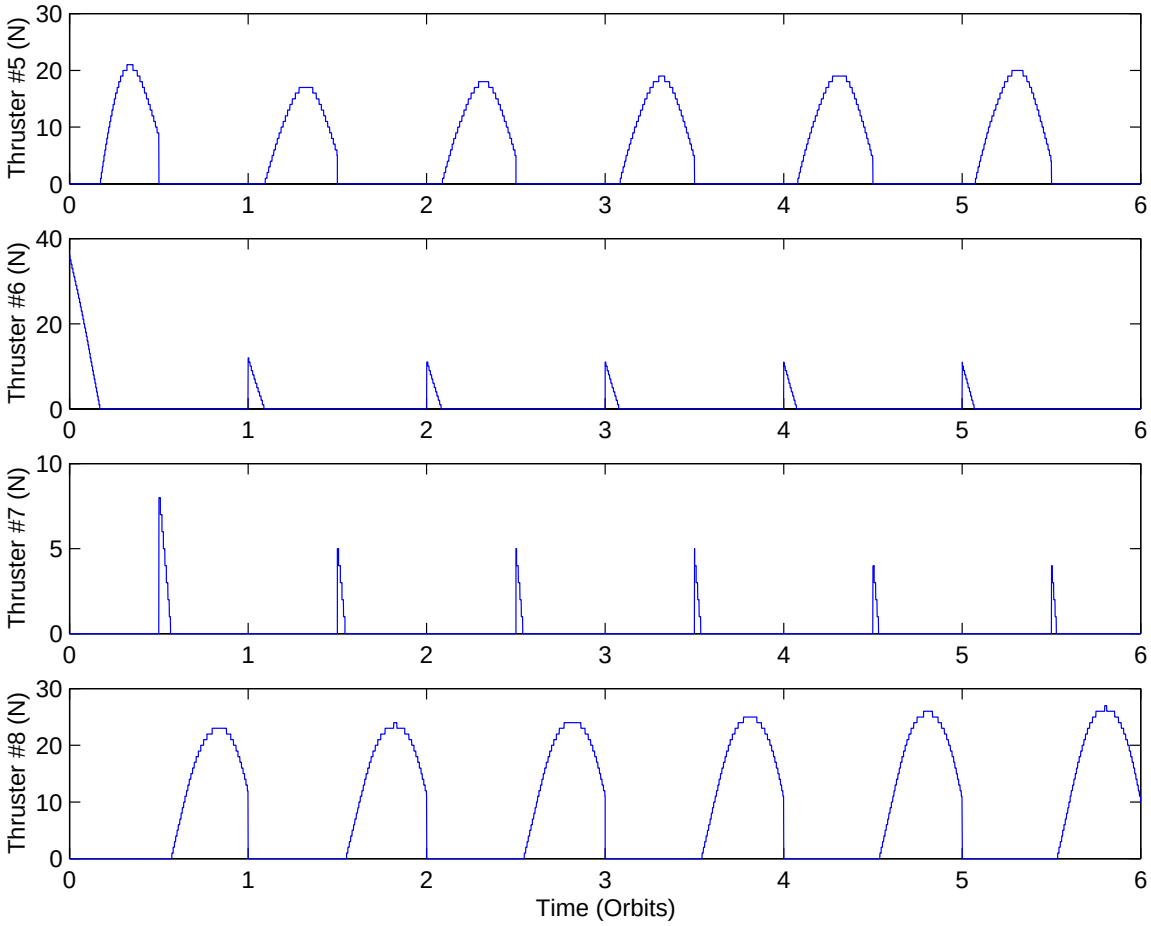

Figure 3.15: Simulation results without cyclic-disturbance rejection control (continued).

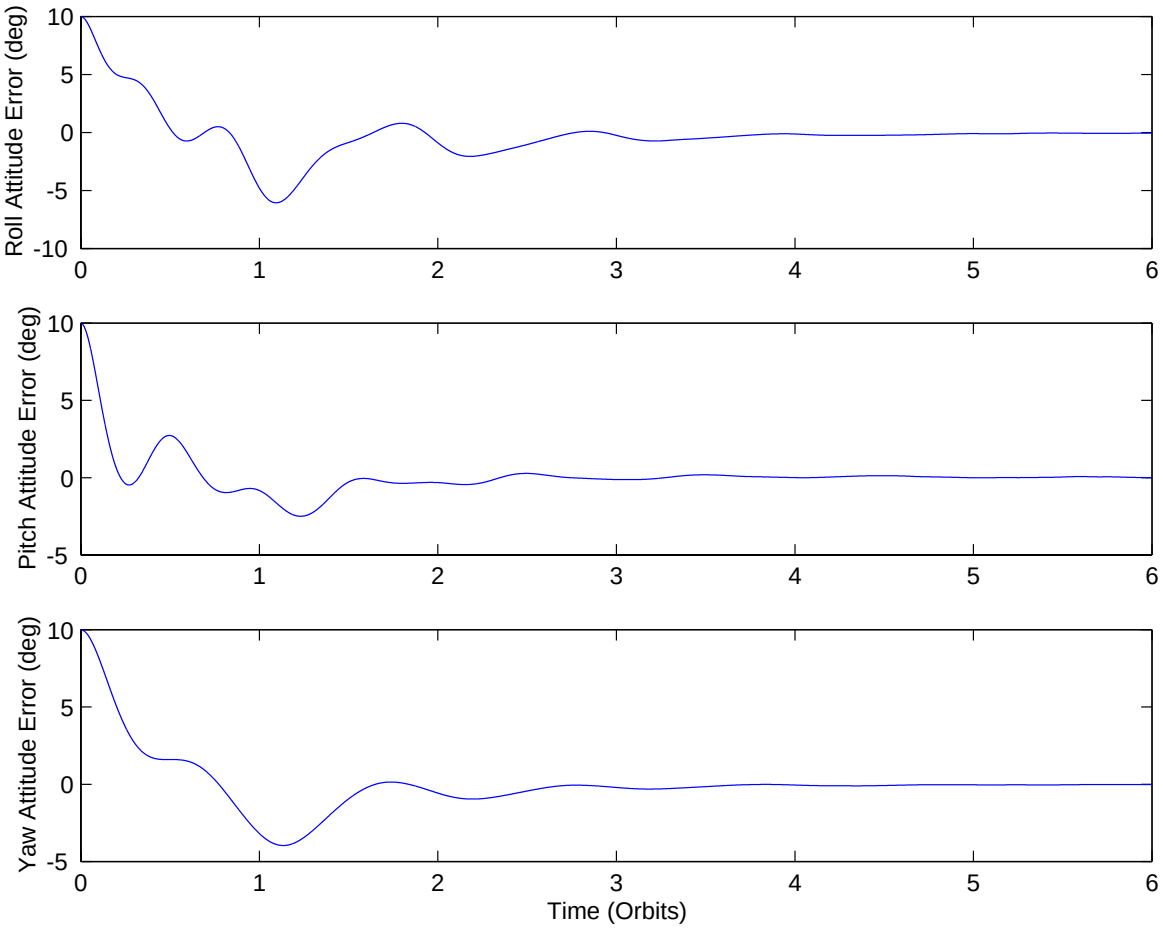

Figure 3.16: Simulation results with cyclic-disturbance rejection control.

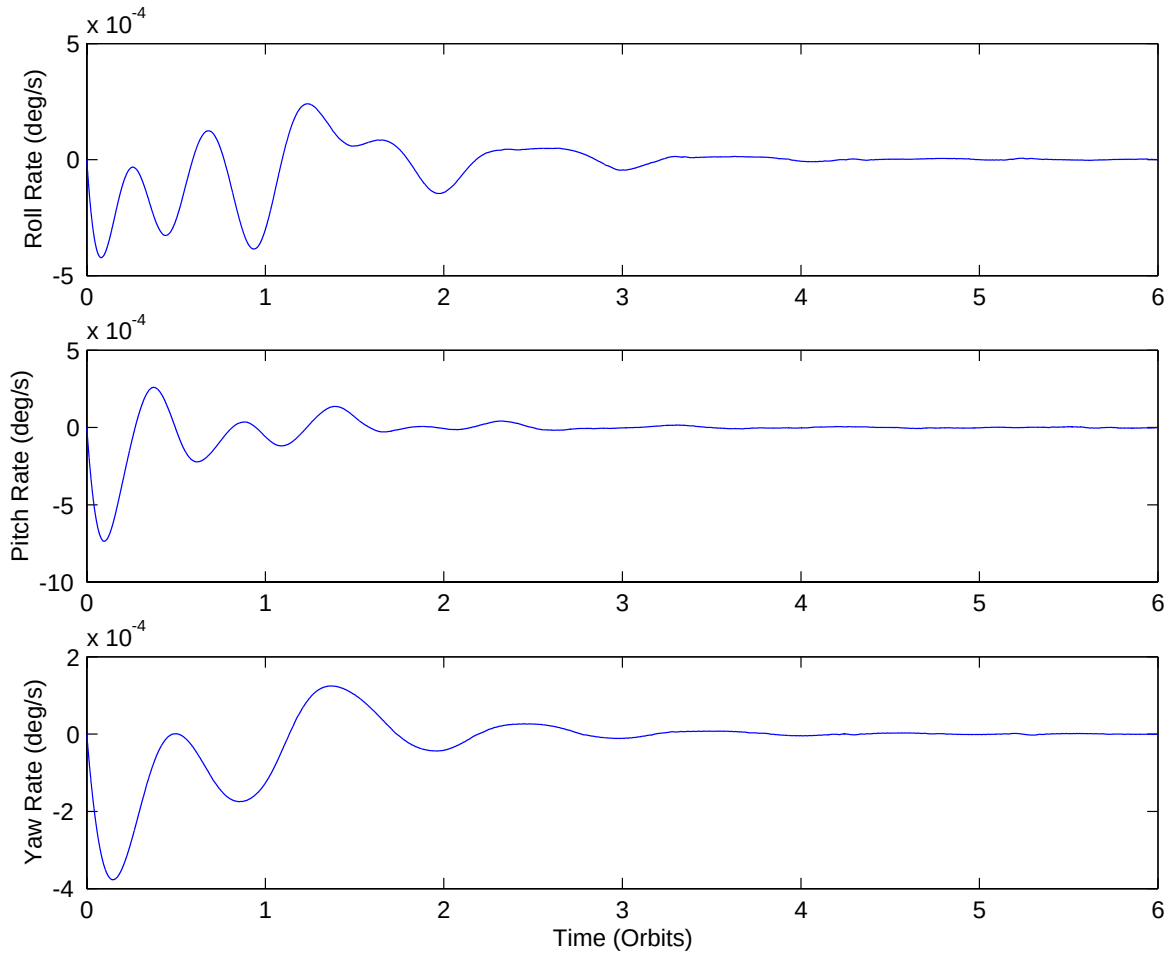

Figure 3.17: Simulation results with cyclic-disturbance rejection control (continued).

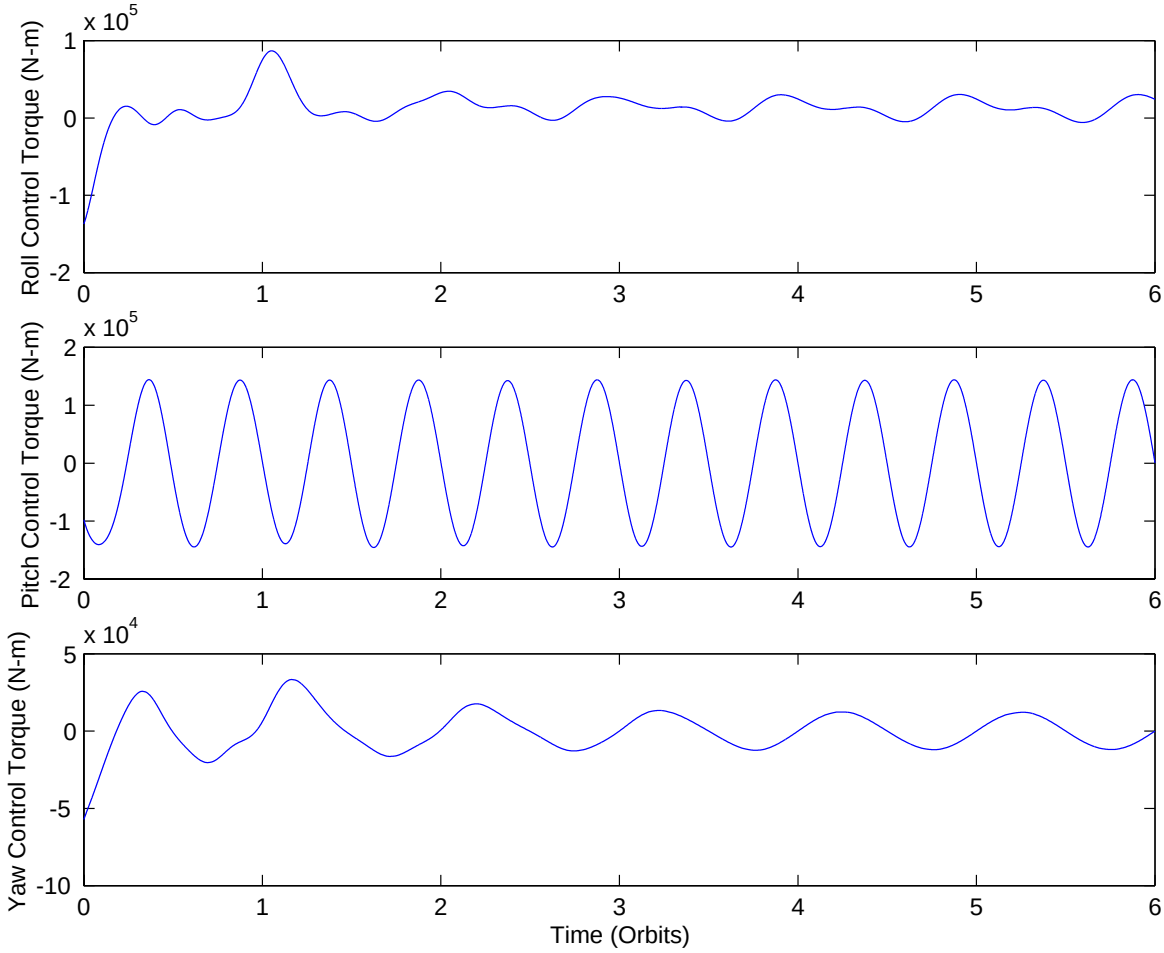

Figure 3.18: Simulation results with cyclic-disturbance rejection control (continued).

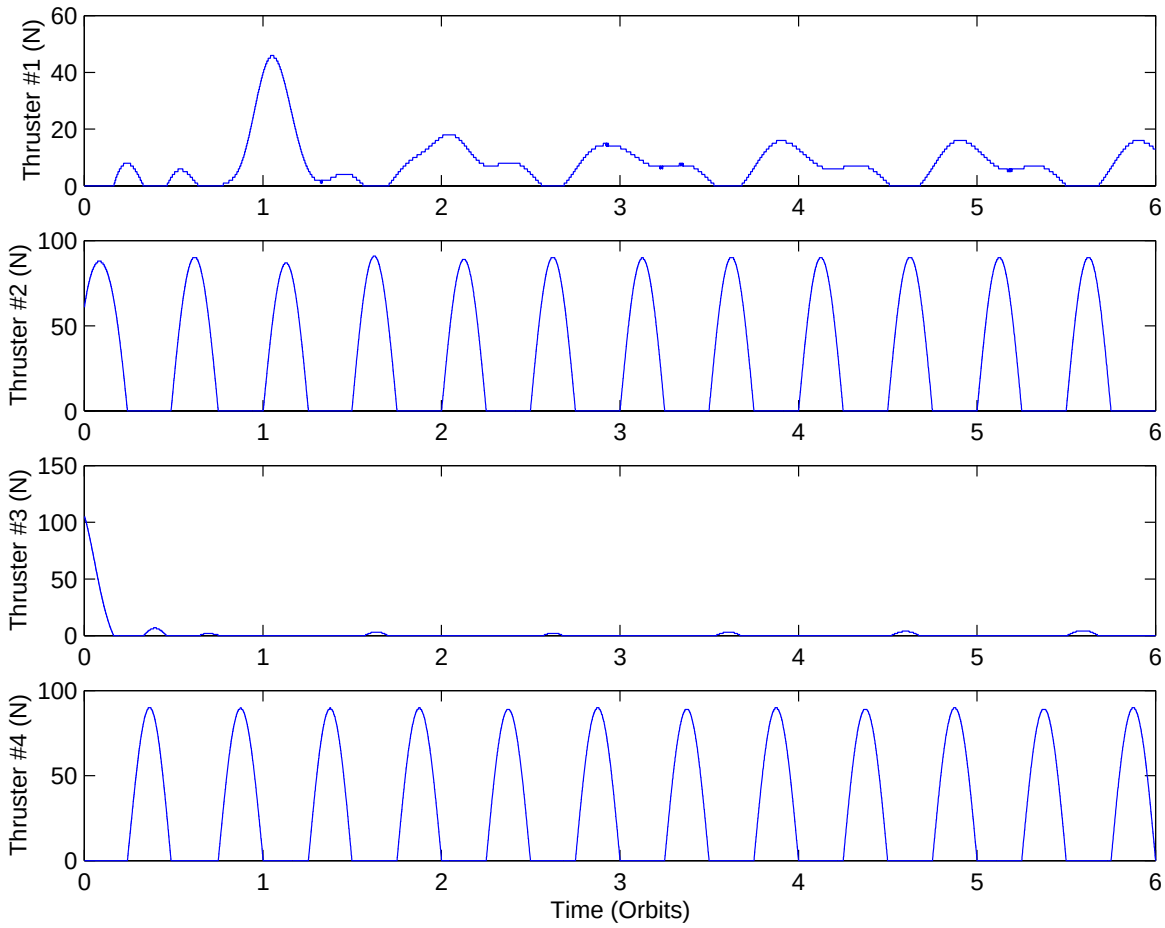

Figure 3.19: Simulation results with cyclic-disturbance rejection control (continued).

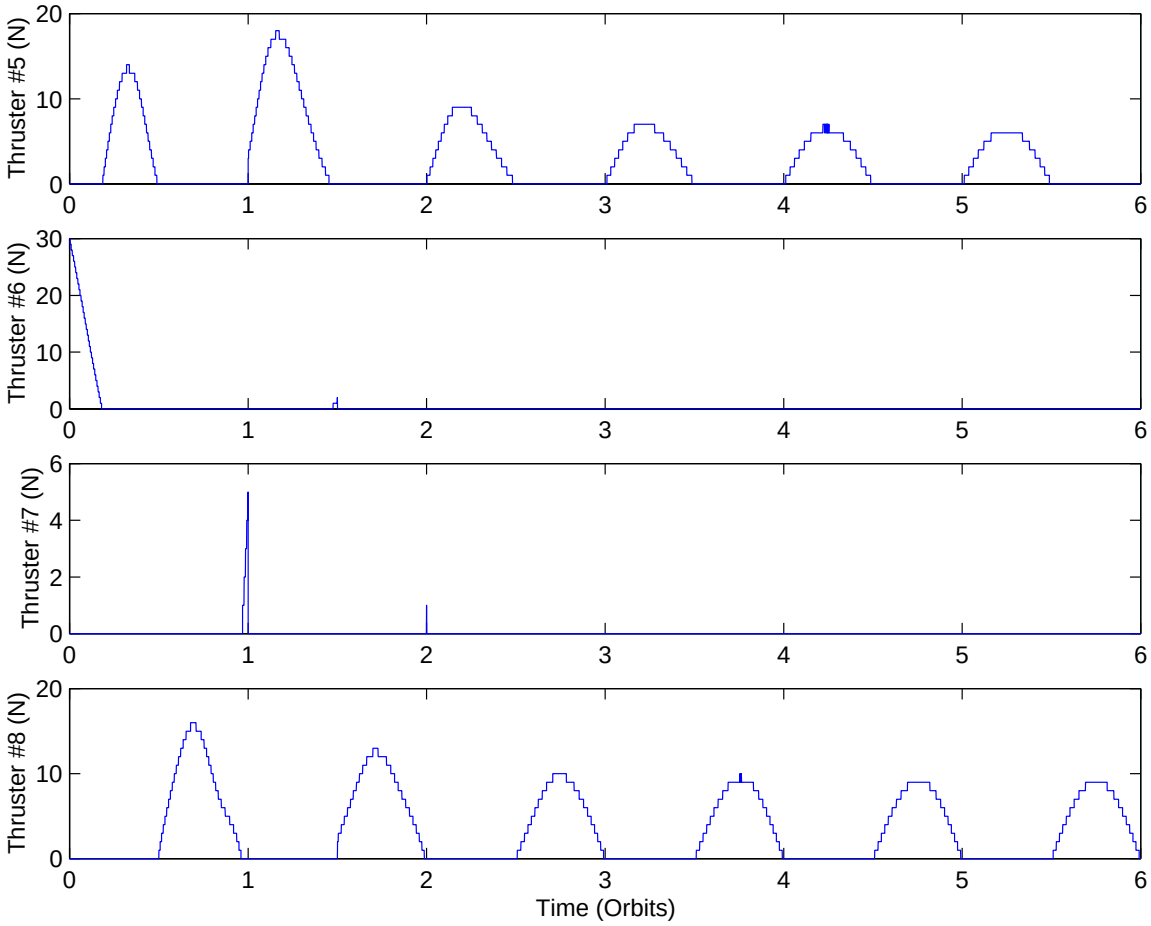

Figure 3.20: Simulation results with cyclic- disturbance rejection control (continued).

Chapter 4

Conclusions and Recommendations

4.1 Summary of Study Results

The major objective of this study was to develop advanced concepts for controlling orbit, attitude, and structural motions of very large Space Solar Power Satellites (SSPS) in geosynchronous orbit. This study focused on the 1.2-GW "Abacus" SSPS concept characterized by a square (3.2 × 3.2 km) solar array platform, a 500-m diameter microwave beam transmitting antenna, and an earth-tracking reflector (500 × 700 m). For this baseline Abacus SSPS configuration, we derived and analyzed a complete set of mathematical models, including external disturbances such as solar radiation pressure, microwave radiation, gravity-gradient torque, and other orbit perturbation effects. An integrated orbit, attitude, and structural control systems architecture developed for the Abacus satellite employs properly distributed, 500 1-N electric propulsion thrusters.

Despite the importance of the cyclic pitch gravity-gradient torque, this study shows that the solar pressure force is considerably more detrimental to control of the Abacus satellite (and other large SSPS) because of an area-to-mass ratio that is very large compared to contemporary, higher-density spacecraft.

A key parameter that characterizes the sensitivity of a satellite to solar radiation pressure is the area-to-mass ratio, A/m; the value of A/m for the Abacus satellite is 0.4 m^2/kg, which is relatively large when compared to 0.02 m^2/kg for typical geosynchronous communications satellites. Solar radiation pressure causes a cyclic drift in the longitude of the Abacus satellite of 2 deg, east and west. Consequently, in addition to standard north/south and east/west stationkeeping maneuvers for ±0.1 deg orbit position control, active control of the orbit eccentricity using electric thrusters becomes nearly mandatory. Furthermore, continuous sun tracking of the Abacus platform requires large control torques to counter various disturbance torques.

The proposed control system architecture utilizes properly distributed ion thrusters to counter, simultaneously, the cyclic pitch gravity-gradient torque, the secular roll torque caused by center of mass - center of pressure offset and solar pressure, the cyclic roll/yaw microwave radiation torque, and the solar pressure force whose average value

is 60 N. In contrast to a typical placement of thrusters at the four corners, e.g., employed for the 1979 SSPS reference system, the proposed placement shown in Figure 3.10 minimizes roll/pitch thruster couplings as well as the excitation of platform out-of-plane bending modes. A control-structure interaction problem of the Abacus platform with the lowest structural mode frequency of 0.002 Hz is avoided simply by designing an attitude control system with very low bandwidth (< orbit frequency). However, the proposed low-bandwidth attitude control system utilizes a concept of cyclic disturbance accommodation to provide ±5 arcmin pointing of the Abacus platform in the presence of large external disturbances and dynamic modeling uncertainties. Approximately 85,000 kg of propellant per year is required for simultaneous orbit, attitude, and structural control using 500 1-N electric propulsion thrusters with a specific impulse of 5000 sec. Only 21,000 kg of propellant per year is required if electric propulsion thrusters with a specific impulse of 20,000 sec can be developed. As I_{sp} is increased, the propellant mass decreases but the electric power requirement increases; consequently, the mass of solar arrays and power processing units increases.

The total dry mass (power processing units, thrusters, tanks, feed systems, etc.) of electric propulsion systems for the Abacus satellite is estimated as 75,000 kg based on a minimum of 500 1-N thrusters and a mass/power ratio of 5 kg/kW. The peak power requirement is estimated as 6 MW based on the total peak thrust requirement of 200 N and a power/thrust ratio of 30 kW/N.

4.2 Recommendations for Future Research

The baseline control system architecture developed for the Abacus satellite requires a minimum of 500 ion engines of 1-N thrust level. The capability of present electric thrusters are orders of magnitude below that required for the Abacus satellite. If the xenon fueled, 1-kW level, off-the-shelf ion engines available today, are to be employed, the number of thrusters would be increased to 15,000. The actual total number of ion engines will further increase significantly when we consider the ion engine's lifetime, reliability, duty cycle, redundancy, etc. Consequently, a 30-kW, 1-N level electric propulsion thruster with a specific impulse greater than 5,000 sec needs to be developed for the Abacus satellite if excessively large number of thrusters are to be avoided.

Several high-power electric propulsion systems are currently under development. For example, the NASA T-220 10-kW Hall thruster recently completed a 1,000-hr life test. This high-power (over 5 kW) Hall thruster provides 500 mN of thrust at a specific impulse of 2,450 sec and 59% total efficiency. Dual-mode Hall thrusters, which can operate in either high-thrust mode or high-I_{sp} mode for efficient propellant usage, are also being developed.

The exhaust gas from an electric propulsion system forms an essentially neutral plasma beam extending for large distances in space. Because little is known yet about the long-term effect of an extensive plasma on geosynchronous satellites with regard to communications, solar cell degradation, etc, the use of lightweight, space-assembled

Table 4.1: Technology advancement needs for the Abacus SSPS

	Current	Enabling
Electric Thrusters	3 kW, 100 mN $I_{sp} = 3,000$ sec (5,000–10,000 thrusters)	30 kW, 1 N $I_{sp} > 5,000$ sec (500–1,000 thrusters)
CMGs	20 N-m-s/kg 5,000 N-m-s/unit (500,000 CMGs)	2,000 N-m-s/kg 500,000 N-m-s/unit (5,000 CMGs)
Space-Assembled Momentum Wheels (300-m diameter)		66,000 N-m-s/kg 4×10^8 N-m-s/unit (5–10 MWs)

large-diameter momentum wheels may also be considered as an option for the Abacus satellite; therefore, these devices warrant further study. The electric thrusters, CMGs, and momentum wheels are compared in Table 4.1 in terms of their technology advancement needs. It is emphasized that both electrical propulsion and momentum wheel technologies require significant advancement to support the development of large SSPS.

Despite the huge size and low structural frequencies of the Abacus satellite, the control-structure interaction problem appears to be a tractable one because the tight pointing control requirement can be met even with a control bandwidth that is much lower than the lowest structural frequency. However, further detailed study needs to be performed for achieving the required 5-arcmin microwave beam pointing accuracy in the presence of transmitter/reflector-coupled structural dynamics, Abacus platform thermal distortion and vibrations, hardware constraints, and other short-term impulsive disturbances.

Although the rotating reflector concept of the Abacus satellite eliminates massive rotary joint and slip rings of the 1979 SSPS reference concept, the transmitter fixed to the Abacus platform results in unnecessarily tight pointing requirements imposed on the platform. Further system-level tradeoffs will be required for the microwave-transmitting antenna design, such as whether or not to gimbal it with respect to the platform, use mechanical or electronic beam steering, and so forth.

The following research topics of practical importance in the areas of dynamics and control of large flexible space platforms also need further detailed investigation to support the development of large SSPS.

- Thermal distortion and structural vibrations due to solar heating
- Structural distortion due to gravity-gradientloading
- Simultaneous eccentricity and longitude control
- Attitude control during the solar eclipses

- Orbit and attitude control during assembly
- Attitude and orbit determination problem
- Reflector tracking and pointing control problem
- Microwave beam pointing analysis and simulation
- Space-assembled, large-diameter momentum wheels
- Electric propulsion systems for both orbit transfer and on-orbit control
- Backup chemical propulsion systems for attitude and orbit control

References

[1] Glaser, P. E., "Power from the Sun: Its Future," *Science,* Vol. 162, No. 3856, November 22, 1968, pp. 857-861.

[2] Glaser, P. E., "The Potential of Satellite Solar Power," *Proceedings of the IEEE*, Vol. 65, No. 8, August 1977, pp. 1162-1176.

[3] Mankins, J. C., "A Fresh Look at Space Solar Power: New Architecture, Concepts, and Technologies," IAF-97-R.2.03, *the 48th International Astronautical Congress,* Turin, Italy, October 6-10, 1997.

[4] Moore, C., "Structural Concepts for Space Solar Power Satellites," *SSP Systems Workshop*, NASA Glenn Research Center, September 8, 1999.

[5] Moore, C., "Structures, Materials, Controls and Thermal Management," *SSP Technical Interchange Meeting #3*, Huntsville, AL, June 19-23, 2000.

[6] Carrington, C. and Feingold, H., "SSP Systems Integration, Analysis and Modeling," *SSP Technical Interchange Meeting #3*, Huntsville, AL, June 19-23, 2000.

[7] Oglevie, R. E., "Attitude Control of Large Solar Power Satellites," *Proceedings of AIAA Guidance and Control Conference*, Palo Alto, CA, 1978, pp. 571-578.

[8] Elrod, B. D., "A Quasi-Inertial Attitude Mode for Orbiting Spacecraft," *Journal of Spacecraft and Rockets*, Vol. 9, December, 1972, pp. 889-895.

[9] Juang, J.-N. and Wang, S.-J., "An Investigation of Quasi-Inertial Attitude Control for a Solar Power Satellite," *Space Solar Power Review*, Vol. 3, 1982, pp. 337-352.

[10] Shrivastava, S. K., "Orbital Perturbations and Stationkeeping of Communication Satellites," *Journal of Spacecraft and Rockets*, Vol. 15, No. 2, 1978, pp. 67-78.

[11] Gartrell, C. F., "Simultaneous Eccentricity and Drift Rate Control," *Journal of Guidance and Control*, Vol. 4, No. 3, 1981, pp. 310-315.

[12] Kamel, A. A. and Wagner, C. A., "On the Orbital Eccentricity Control of Synchronous Satellites," *Journal of the Astronautical Sciences*, Vol. XXX, No. 1, 1982, pp. 61-73.

[13] Kelly, T. J., White, L. K., and Gamble, D. W., "Stationkeeping of Geostationary Satellites with Simultaneous Eccentricity and Longitudinal Control," *Journal of Guidance, Control, and Dynamics*, Vol. 17, No. 4, 1994, pp. 769-777.

[14] McInnes, C. R., *Solar Sailing: Technology, Dynamics and Mission Applications*, Springer Praxis Publishing, Chichester, UK, 1999.

[15] Burns, R., et al., "Solar Radiation Pressure Effects on Formation Flying of Satellites with Different Area-to-Mass Ratios," AIAA Paper No. 2000-4132, AIAA/AAS Astrodynamics Specialist Conference, Denver, Co., August 14-17, 2000.

[16] Battin, R. H., *An Introduction to the Mathematics and Methods of Astrodynamics,* AIAA Education Series, AIAA, Washington, DC, 1987.

[17] Wie, B., *Space Vehicle Dynamics and Control*, AIAA Education Series, AIAA, Washington, DC, 1998.

[18] Kamel, A. A., Ekman, D., and Tibbitts, R., "East-West Stationkeeping Requirements of Nearly Synchronous Satellites Due to earth's Triaxiality and Luni-Solar

Effects," *Celestial Mechanics*, Vol. 8, 1973, pp. 129-148.

[19] Kamel, A. A., "Geosynchronous Satellite Perturbations Due to Earth's Triaxiality and Luni-Solar Effects," *Journal of Guidance, Control, and Dynamics*, Vol. 5, No. 2, 1982, pp. 189-193.

[20] Chao, C. C., "Simultaneous Stationkeeping of Geosynchronous Satellites," *Journal of Guidance, Control, and Dynamics*, Vol. 7, No. 1, 1984, pp. 57-61.

[21] Marsh, J. G., et al., "A New Gravitational Model for the Earth from Satellite Tracking Data: GEM-T1", *Journal of Geophysical Research*, Vol. 93, No. B6, June 10, 1988. pp. 6169-6215.

[22] Agrawal, B. N., *Design of Geosynchronous Spacecraft*, Englewood Cliffs, NJ, Prentice-Hall, 1986.

[23] Roithmayr, C. M., "Gravitational Moment Exerted on a Small Body by an Oblate Body," *Journal of Guidance, Control, and Dynamics*, Vol. 12, No. 3, 1989, pp. 441-444.

[24] Kumar, V. K. and Bainum, P. M., "Dynamics of a Flexible Body in Orbit," *Journal of Guidance and Control*, Vol. 3, No. 1, 1980, pp. 90-92.

[25] Reddy, A. S., Bainum, P. M., Krishna., R., and Hamer, H. A., "Control of a Large Flexible Platform in Orbit," *Journal of Guidance and Control*, Vol. 4, No. 6, 1981, pp. 642-649.

[26] Krishna, R. and Bainum, P. M., "Dynamics and Control of Orbiting Flexible Structures Exposed to Solar Radiation," *Journal of Guidance, Control, and Dynamics*, Vol. 8, No. 5, 1985, pp. 591-596.

[27] Bryson, A. E., Jr., *Control of Spacecraft and Aircraft*, Princeton University Press, Princeton, NJ, 1994.

[28] Wie, B., Liu, Q., and Bauer, F., "Classical and Robust H_∞ Control Redesign for the Hubble Space Telescope," *Journal of Guidance, Control, and Dynamics*, Vol. 16, No. 6, 1993, pp. 1069-1077.

[29] Wie, B., et al., "New Approach to Momentum/Attitude Control for the Space Station," *Journal of Guidance, Control, and Dynamics*, Vol. 12, No. 5, 1989, pp. 714-722.

[30] Wie, B., Liu, Q., and Sunkel, J., "Robust Stabilization of the Space Station in the Presence of Inertia Matrix Uncertainty," *Journal of Guidance, Control, and Dynamics*, Vol. 18, No. 3, 1995, pp. 611-617.

[31] Wie, B., "Active Vibration Control Synthesis for the COFS (Control of Flexible Structures) Mast Flight System," *Journal of Guidance, Control, and Dynamics*, Vol. 11, No. 3, 1988, pp. 271-276.

[32] Wie, B., Horta, L., and Sulla, J., "Active Vibration Control Synthesis and Experiment for the Mini-Mast," *Journal of Guidance, Control, and Dynamics*, Vol. 14, No. 4, 1991, pp. 778-784.

[33] Wie, B., "Experimental Demonstration of a Classical Approach to Flexible Structure Control," *Journal of Guidance, Control, and Dynamics*, Vol. 15., No. 6, 1992, pp. 1327-1333.

Appendix A

Simulation of Orbital Motion

A.1 Introduction

Numerical simulations of orbital motion, the results of which are presented in Chapters 1 and 2, employ the algorithms described briefly in what follows.

Encke's method, as described in Sec. 9.4 of Ref. [16], and in Sec. 9.3, of Ref. [2], lies at the heart of a MATLAB/SIMULINK computer program used to integrate dynamical and kinematical equations governing relative translational motion of two bodies.

This appendix begins with a brief description of the general relationship for two-body motion, then provides an overview of Encke's method and how it is carried out in the computer program, and ends with a presentation of the expressions used in computing the various contributions to the perturbing forces exerted on the two bodies.

A.2 Two-Body Motion

As discussed in Chapter 2, the relative orbital motion of two bodies is described by

$$\ddot{\vec{r}} + \frac{\mu}{r^3}\vec{r} = \vec{f} = \vec{f}_B - \vec{f}_P \tag{1}$$

where $\vec{r}$ is the position vector from the mass center $P^\star$ of a planet P to the mass center $B^\star$ of a body B, r is the magnitude of $\vec{r}$, $\ddot{\vec{r}}$ indicates the second derivative of $\vec{r}$ with respect to time t in an inertial or Newtonian reference frame N, and $\mu \triangleq G(m_P + m_B)$, where G is the universal gravitational constant, m_P is the mass of P, and m_B is the mass of B.

If P were a sphere with uniform mass distribution, or a particle, and if B were a particle, then the gravitational force exerted by P on B would be given by $\vec{g} = -G\,m_P\,m_B\,\vec{r}/r^3$. The force exerted by B on P would be simply $-\vec{g}$. The vector $\vec{f}_B$ represents the resultant force per unit mass acting on B, *other than* $\vec{g}/m_B$; $\vec{f}_P$ represents the resultant force per unit mass acting on P, *other than* $-\vec{g}/m_P$.

When $\vec{f}$ is as large or larger than $\mu\vec{r}/r^3$, integration of Eq. (1) is advisable and is referred to as *Cowell's method*. On the other hand, when $\vec{f}$ is small in comparison to $\mu\vec{r}/r^3$ Cowell's method can be disadvantageous in terms of numerical efficiency, and a different strategy known as *Encke's method* may be preferred.

A.3 Encke's Method

The method of Encke requires the solution of ordinary differential equations governing the behavior of $\vec{\delta}$,

$$\vec{\delta} \triangleq \vec{r} - \vec{\rho} \tag{2}$$

where $\vec{\rho}$ represents the solution of Eq. (1) with $\vec{f} = \mathbf{0}$; the path traced out by $\vec{\rho}$ is a conic section, known as the *osculating orbit*. The orbit described by $\vec{r}$ is the actual or true orbit of B about P, which differs from the osculating orbit whenever $\vec{f}$ does not vanish.

The behavior of $\vec{\delta}$ is governed by Eq. (9.27) of Ref. [16],

$$\ddot{\vec{\delta}} = \vec{f} - \frac{\mu}{\rho^3}[\vec{\delta} + f(q)\vec{r}] \tag{3}$$

where $\ddot{\vec{\delta}}$ indicates the second derivative of $\vec{\delta}$ with respect to time t in N, and ρ is the magnitude of $\vec{\rho}$. The function f of q is given by

$$f(q) = q\frac{3 + 3q + q^2}{1 + (1+q)^{\frac{3}{2}}} \tag{4}$$

where q is defined as

$$q \triangleq \frac{\vec{\delta} \cdot (\vec{\delta} - 2\vec{r})}{\vec{r} \cdot \vec{r}} \tag{5}$$

The values of $\vec{\delta}$ and $\dot{\vec{\delta}}$ are both zero at the beginning of each simulation, and also following orbit rectification, or the point at which the osculating position and velocity, $\vec{\rho}$ and $\dot{\vec{\rho}}$, are made equal to the true position and velocity, $\vec{r}$ and $\dot{\vec{r}}$, respectively. Rectification is performed when, as suggested in Ref. [2], $(\vec{\delta} \cdot \vec{\delta})^{1/2} \geq 0.01(\vec{\rho} \cdot \vec{\rho})^{1/2}$.

The osculating orbit is determined as a function of time using initial values for $\vec{\rho}$ and $\dot{\vec{\rho}}$ (which change with each rectification), together with Battin's universal formulae for conic orbits according to Eqs. (3.33) and (4.84), and the relationships given in Prob. 4–21 of Ref. [1]. Use of the universal formulae requires a generalized anomaly χ, obtained by Newtonian iteration as set forth in Eq. (4.4–15) of Ref. [2], or at the top of p. 219 in Ref. [1]; iteration is terminated when the time associated with χ through the generalized form of Kepler's equation [Eq. (4.81), Ref. [1]], is within 1×10^{-4} sec of the simulation time t.

Six scalar, first order, ordinary differential equations corresponding to the second order vector Eq. (3) are integrated using a variable step, Runge-Kutta 4-5 scheme, with relative and absolute error tolerances set to 1×10^{-8}. The true position and velocity, $\vec{r}$ and $\dot{\vec{r}}$, are used to calculate classical orbital elements a, e, i, Ω, ω, and M according to the material in Secs. 2.3 and 2.4 of Ref. [2], and Secs. 3.3 and 4.3 of Ref. [1].

A.4 Contributions to the Perturbing Force

In the case of geosynchronous satellites the perturbing force per unit mass $\vec{f}$ receives significant contributions from the gravitational attraction of the Sun and Moon, Earth's tesseral gravitational harmonics of degree 2 and orders 0 and 2, and solar radiation pressure, as discussed in Sec. 2.2. The remainder of this section contains the expressions employed in the computer program for these contributions, denoted respectively as $\vec{f}_s$, $\vec{f}_m$, $\vec{f}_{2,0}$, $\vec{f}_{2,2}$, and $\vec{f}_r$, such that

$$\vec{f} = \vec{f}_s + \vec{f}_m + \vec{f}_{2,0} + \vec{f}_{2,2} + \vec{f}_r \tag{6}$$

A.4.1 Solar and Lunar Gravitational Attraction

The gravitational force per unit mass exerted by the Sun on P is given by $\mu_s \vec{r}_s / r_s^3$, where μ_s is the product of G and the Sun's mass, $\vec{r}_s$ is the position vector from $P^\star$ to the Sun's mass center, and r_s is the magnitude of $\vec{r}_s$. Likewise, the gravitational force per unit mass exerted by the Sun on B is given by $\mu_s(\vec{r}_s - \vec{r})/|\vec{r}_s - \vec{r}|^3$. Therefore,

$$\vec{f}_s = \frac{\mu_s(\vec{r}_s - \vec{r})}{|\vec{r}_s - \vec{r}|^3} - \frac{\mu_s \vec{r}_s}{r_s^3} \tag{7}$$

When $\vec{r}$ is small in comparison to $\vec{r}_s$, numerical difficulties can be encountered in the evaluation of the right hand member of Eq. (7); therefore, an alternate form of $\vec{f}_s$ is used, as suggested in Eq. (8.61) of Ref. [1]:

$$\vec{f}_s = -\frac{\mu_s}{|\vec{r}_s - \vec{r}|^3}[\vec{r} + f(q_s)\vec{r}_s] \tag{8}$$

where

$$q_s \triangleq \frac{\vec{r} \cdot (\vec{r} - 2\vec{r}_s)}{\vec{r}_s \cdot \vec{r}_s} \tag{9}$$

The position vector $\vec{r}_s$ from Earth's mass center (actually, the Earth-Moon barycenter) to the Sun's mass center, projected onto geocentric-equatorial directions and referred to the ecliptic of date, is obtained as a function of t with the formulae and numerical values given on p. E4 of Ref. [3].

Similarly, the contribution of lunar gravitational attraction to $\vec{f}$ is given by

$$\vec{f}_m = \frac{\mu_m(\vec{r}_m - \vec{r})}{|\vec{r}_m - \vec{r}|^3} - \frac{\mu_m \vec{r}_m}{r_m^3} \tag{10}$$

where μ_m is the product of G and the Moon's mass, $\vec{r}_m$ is the position vector from $P^\star$ to the Moon's mass center, and r_m is the magnitude of $\vec{r}_m$. Numerical difficulties are avoided by using the expression

$$\vec{f}_m = -\frac{\mu_m}{|\vec{r}_m - \vec{r}|^3}[\vec{r} + f(q_m)\vec{r}_m] \tag{11}$$

where

$$q_m \triangleq \frac{\vec{r} \cdot (\vec{r} - 2\vec{r}_m)}{\vec{r}_m \cdot \vec{r}_m} \tag{12}$$

The position vector $\vec{r}_m$ from Earth's mass center to the Moon's mass center, projected onto geocentric-equatorial directions, and referred to the mean equator and equinox of date, is obtained as a function of t with the algorithm set forth on p. D46 of Ref. [3].

A.4.2 Tesseral Harmonics

The computer program makes use of Eq. (12) of Ref. [4] to account for the gravitational harmonics of P, for any degree n and order m; in the simulations performed for this study, n and m are limited to 2. Numerical values of the gravitational coefficients, gravitational parameter of Earth, and mean equatorial radius, are those of the Goddard Earth Model T1 as reported in Ref. [5].

Earth's oblateness is represented by a zonal harmonic of degree 2 and order 0, and is responsible for precessions in a satellite's orbit plane and argument of perigee. The contribution of this harmonic to the force per unit mass exerted by P on B is given in Eq. (45) of Ref. [4] (also Prob. 3.7b in Ref. [6]) as

$$\vec{f}_{2,0} = -\mu_\oplus J_2 \frac{{R_\oplus}^2}{r^4}\left[3\sin\phi\,\vec{e}_3 + \frac{3}{2}(1 - 5\sin^2\phi)\frac{\vec{r}}{r}\right] \tag{13}$$

where $\mu_\oplus$ is the gravitational parameter of the Earth, the product of G and the Earth's mass; $R_\oplus$ is the mean equatorial radius of the Earth (6378.137 km), r is the magnitude of $\vec{r}$, and ϕ is the geocentric latitude of B. Unit vector $\vec{e}_3$ is fixed in the Earth in the direction of the north polar axis.

The contribution of oblateness to the force per unit mass exerted by B on P is given by $-m_B\,\vec{f}_{2,0}/m_P$, and the contribution of oblateness to $\vec{f}$ is thus $[1 + (m_B/m_P)]\vec{f}_{2,0}$. In the case of the SSP orbiting Earth $m_B = 25 \times 10^6$ kg and $m_P = 5.98 \times 10^{24}$ kg, so $m_B/m_P = 4 \times 10^{-18}$, which can be neglected in comparison to 1; therefore, the entire contribution of oblateness to $\vec{f}$ is essentially equal to $\vec{f}_{2,0}$.

The contribution $\vec{f}_{2,1}$ of the tesseral harmonic of degree 2 and order 1 vanishes because the harmonic coefficients $S_{2,1}$ and $C_{2,1}$ are both zero. The harmonic of degree 2 and order 2 can cause the longitude of of a geosynchronous spacecraft to drift; from Eq. (12) of Ref. [4] the contribution to the force per unit mass exerted by P on B is given by

$$\vec{f}_{2,2} = \frac{\mu_\oplus {R_\oplus}^2}{r^5}\left\{\frac{C_{2,2}\mathcal{C}_2 + S_{2,2}\mathcal{S}_2}{r}\left[A_{2,3}\vec{e}_3 - (\sin\phi A_{2,3} + 5A_{2,2})\frac{\vec{r}}{r}\right]\right.$$

$$+ 2A_{2,2}\left[(C_{2,2}\mathcal{C}_1 + S_{2,2}\mathcal{S}_1)\vec{e}_1 + (S_{2,2}\mathcal{C}_1 - C_{2,2}\mathcal{S}_1)\vec{e}_2\right]\Big\} \tag{14}$$

where unit vectors $\vec{e}_1$ and $\vec{e}_2$ are fixed in the Earth: $\vec{e}_1$ lies in the equatorial plane parallel to a line intersecting Earth's geometric center and the Greenwich meridian, and $\vec{e}_2 = \vec{e}_3 \times \vec{e}_1$.

Equations (6) and (7) of Ref. [4] indicate that the required derived Legendre polynomials are $A_{2,2} = 3$ and $A_{2,3} = 0$. In addition, Eqs. (9) and (10) of Ref. [4] show that

$$\mathcal{S}_1 = \vec{r} \cdot \vec{e}_2 = r\cos\phi\sin\lambda, \quad \mathcal{C}_1 = \vec{r} \cdot \vec{e}_1 = r\cos\phi\cos\lambda \tag{15}$$

$$\mathcal{S}_2 = 2(r\cos\phi)^2\sin\lambda\cos\lambda, \quad \mathcal{C}_2 = (r\cos\phi)^2(\cos^2\lambda - \sin^2\lambda) \tag{16}$$

where λ is the geographic longitude of B measured eastward from the Greenwich meridian. Therefore,

$$\vec{f}_{2,2} = \frac{\mu_\oplus {R_\oplus}^2}{r^4}\Big\{-15\cos^2\phi[C_{2,2}(\cos^2\lambda - \sin^2\lambda) + 2S_{2,2}\sin\lambda\cos\lambda]\frac{\vec{r}}{r}$$
$$+ 6\cos\phi\left[(C_{2,2}\cos\lambda + S_{2,2}\sin\lambda)\vec{e}_1 + (S_{2,2}\cos\lambda - C_{2,2}\sin\lambda)\vec{e}_2\right]\Big\} \tag{17}$$

As in the case of $\vec{f}_{2,0}$, m_B/m_P is neglected in comparison to 1, and $\vec{f}_{2,2}$ thus constitutes the entire contribution of the present harmonic to $\vec{f}$.

A.4.3 Solar Radiation Pressure

The force per unit mass of solar radiation pressure exerted on B is given by $-C(\vec{r}_s - \vec{r})/(m_B|\vec{r}_s - \vec{r}|)$ where C is a constant, 60 N. We neglect the solar radiation pressure exerted on the Earth, and write

$$\vec{f}_r = \frac{C(\vec{r} - \vec{r}_s)}{m_B|\vec{r}_s - \vec{r}|} \tag{18}$$

References

[1] Battin, R. H., *An Introduction to The Mathematics and Methods of Astrodynamics*, AIAA, New York, 1987.

[2] Bate, R. R., Mueller, D. D., and White, J. E., *Fundamentals of Astrodynamics*, Dover Publications, Inc., New York, 1971.

[3] *The Astronomical Almanac for the Year 1999*, Nautical Almanac Office, United States Naval Observatory, U.S. Government Printing Office.

[4] Roithmayr, C. M., "Contributions of Spherical Harmonics to Magnetic and Gravitational Fields", EG2-96-02, NASA Johnson Space Center, Jan. 23, 1996.

[5] Marsh, J. G., et al., "A New Gravitational Model for the Earth from Satellite Tracking Data: GEM-T1", *Journal of Geophysical Research*, Vol. 93, No. B6, June 10, 1988. pp. 6169-6215.
[6] Wie, B., *Space Vehicle Dynamics and Control*, AIAA Education Series, AIAA, Washington, DC, 1998.